UNIVERSITY OF CALIFORNIA
RIVERSIDE

An Organic Geochemical Approach to Understanding Microbial Community Dynamics During Paleoenvironmental Transitions

A Dissertation submitted in partial satisfaction
of the requirements for the degree of

Doctor of Philosophy

in

Geological Sciences

by

Aaron Matthew Martinez

June 2020

Dissertation Committee:
Dr. Gordon Love, Chairperson
Dr. Mary Droser
Dr. Sandra Kirtland Turner

The Dissertation of Aaron Matthew Martinez is approved:

_____

_____

_____

Committee Chairperson

University of California, Riverside

ACKNOWLEDGEMENTS

This research was made possible through funding and support from National Science Foundation Earth Sciences Program grants NSF-EAR 134898 and NSF-EAR 1664247, the Agouron Institute, the University of California Jump Start Fellowship, Dissertation Year Fellowship, and Blanchard Fellowship programs, the American Museum of Natural History – Theodore Roosevelt Memorial Grant, the SEPM Student Research Grant, the GCS-SEPM Foundation Ed Picou Fellowship Grant, the Geological Society of America, and the National Science Foundation Graduate Research Fellowship Program.

I am most grateful to Gordon Love, my primary advisor, who has provided expert guidance and much-needed expertise during my time at UCR. Similar thanks go to Mary Droser, with whom I had the honor of being counted as a lab member and who was always around to chat. To both of you, thank you for providing a place to call home for the last several years. Additional thanks to the members of my qualification and dissertation committees – Sandra Kirtland Turner, Marilyn Fogel, and Samantha Ying – who provided excellent feedback and discussions both about science and beyond.

I have been lucky to receive a great amount support over the years. Foremost Diana Boyer, who has functioned as an informal advisor to me both in the field and away – you have my constant gratitude. I thank Carmi Thompson, Juanita Diaz, and Gordon Baird for their expertise in the field, as well as Juanita Diaz, Bridget Lee, Cecilia Lopez, Steve Bates, and Ying Lin for their expertise in the lab.

The research presented here would not have been possibly without the help of several collaborators including Eva Stüeken, Craig Barrie, and Paul Olsen. Samples analyzed in this work were provided in part by Eva Stüeken and by courtesy of the Ocean Drilling Program. Additional access to instrumentation was provided by Marylin Fogel and Tim Lyons at UCR, Roger Buick at UW, and GeoMark Research.

The writing here is, in part, reprints of the manuscripts: Martinez A.M., Boyer D.L., Droser M.L., Barrie C., and Love G.D. (2019) "A stable and productive marine microbial community was sustained through the end-Devonian Hangenberg Crisis within the Cleveland Shale of the Appalachian Basin, United States" *Geobiology* 17:27–42 (Chapter 2) and Stüeken, E. E., Martinez, A., Love, G., Olsen, P. E., Bates, S., and Lyons, T. W. (2019) "Effects of pH on redox proxies in a Jurassic rift lake: Implications for interpreting environmental records in deep time" *Geochimica et Cosmochimica Acta*, 252:240–267 (Chapter 3). Gordon Love was the main supervisor for Chapters 2 and 4; Eva Stüeken was the driving force behind Chapter 3.

The real heroes of this dissertation are the Love Biogeochemistry Lab: Emily Haddad, who took a paleontologist and taught them chemistry; Carina Lee, a verifiable font of geochemical knowledge, friendship, and excellent musical taste; Rosemarie Bisquera, an honorable companion and the life of New Years Eve; Alex Zumberge, grand master of the smoked brisket; JP Duda, companion on the 16 bus line; Nathan Marshall, keeper of the cool; and Adriana Rizzo, who is inspiration herself.

I had the great fortune to be counted as a member of the Droser Paleoecology Lab with: Robyn Dahl, a fantastic role model and bowling partner; Christine Solon Hall, soul

sister extraordinaire; Scott Evans, my Hoopla competition; Michelle Zill, the burrowmeister; Bridget Kelly, who humors my love of shells; Rachel Suprenant, tubetastic; and Phil Boan, because my life needed to be more meme-like.

Further appreciation to all the UCR faculty, staff, and students from whom I have learned much. In particular, Laurie Graham to whom I turn when lab things go wrong and the BEES staff for helping life run smoothly, especially Karen Cato for logistical help with the 2018 SoCal Geobiology Symposium. Thanks again to the graduate student staff for that event: Kelden Pehr, Maria Figueroa, Chris Tino, Adam Hoffman, and Jennifer Humphreys. Much appreciation to Andrey Bekker and Gareth Funning for letting me tag along on class field trips.

Sushi club with Jerlyn Swaitlowski was the highlight of many nights. Thanks to Charlie Diamond for the good taste in music, Shelley Wernette for fun Thanksgivings, Leanne Hancock for the leadership, Kim Lau for many coffee breaks, Caroline Hung for the dance parties, and Eugene Shi for keeping me fed. I highly appreciate the folks of the Geobiology Course 2017 with a shout out to Daan Speth – you made that summer one of my best. A special mention to Jennifer Humphreys, who has climbed all through life's ups and downs with me. Similarly to Alex Kovalick, who reminds me how effortless life can be. Thanks to the continued support from my family, who still find ways to surprise me with care packages. Lastly, to my partner on many journeys past and to come, Kelden Pehr, in the immortal words of Portgas D. Ace: Thank you.

ABSTRACT OF THE DISSERTATION

An Organic Geochemical Approach to Understanding Microbial Community Dynamics During Environmental Transitions

by

Aaron Matthew Martinez

Doctor of Philosophy, Graduate Program in Geological Sciences
University of California, Riverside, June 2020
Dr. Gordon Love, Chairperson

Organic geochemistry provides a way to explore the dynamics of past life on the Earth without requiring the preservation of discrete macrofossils. In particular, lipid biomarker analysis and stable isotope analyses, combined with sedimentological, paleontological, and other geochemical background, can be utilized to understand biogeochemical cycles as well as the sources and preservation of organic matter. These, in turn, may help unravel questions such as the distribution of primary producers during mass extinctions, hydrological dynamics of ancient rift systems, and the interactions of local environments on global carbon and climate systems.

Throughout this dissertation, I will walk through time to discrete events in the history of life on Earth. Through lipid biomarker, isotope, and complimentary techniques I characterize past paleoenvironments to understand transitions occurring in the biosphere, and vice versa. We will begin at one of the great mass extinctions, the End Devonian Hangenberg Crisis. Using a mix of geochemical techniques, I locate this mass

extinction within the Cleveland Shale Member of the Ohio Shale, then show that there is a stable microbial community of primary producers throughout the event, despite devastating losses occurring in the macrofaunal clades. Then, we fast forward to the Jurrasic, where we use a suite of environmentally relevant lipid biomarkers to constrain the hydrologic history of an ancient rift lake system and make inferences about environmental variables such as pH and salinity. Lastly, I explore some nuances of Cenozoic carbon cycle dynamics by unraveling the depositional history of organic matter at a high-latitude, nearshore marine basin and find that significant amounts of complex terrigenous materials were continuously sequestered into the early-middle Eocene Norwegian-Greenland Sea.

TABLE OF CONTENTS

Chapter Five: Summary of the Dissertation

LIST OF FIGURES

LIST OF TABLES

CHAPTER ONE

Introduction to the Dissertation

1. Introduction

Rocks record life. The evolutionary history of life on Earth is intimately tied to geologic processes through intricate and diverse biogeochemical cycles. Records of past geobiological processes are preserved within ancient rocks – sometimes faithfully, but often with artistic license. It is now understood that cellular life appeared early in the history of our planet, but rates of evolutionary change and leaps in organismal and ecological complexity vary enormously across geological time. Profound restructuring of marine ecology has often been associated with episodes of major climatic and/or environmental change that have punctuated and reshaped the course of life on Earth. It is key, then, to distinguish both the primary drivers of both biological and environmental change, and their downstream manifestations, during transitional periods in Earth's history to better understand these important events and the potential consequences of changing climates and environments on our planet today.

Studies of ecological and environmental change, including major mass extinction events, often derive from a paleontological perspective focused on marine macrofaunal invertebrates, for good reason. These organisms are abundant and readily preserved as fossils; drastic changes in fossil assemblages provide a robust method for interpreting past perturbations to ecological space. Recently, huge databases provide computing power to unravel intricacies of evolutionary rates and biodiversity changes through time.

However, these fossil records, while powerful, are as all proxies: imperfect. The ancient worlds where those fossil organisms thrived and faded would have been distinctly governed by diverse biogeochemical cycles that shaped environmental chemistry. When considering the past, it is thus imperative not only to observe the higher-level fauna, but in particular the microbial primary producers that form the base of marine food webs and drive global biogeochemical cycles.

For more recent periods in Earth history, primary producers and other lower trophic levels are well-represented in the marine fossil record in the form of microfossils. But the growth and preservation of these biomineralized tests requires specific nutrient and redox environments (such as bioavailable silica or a non-reducing bottom water). These fossils also do not speak to organic-walled or soft-bodied organisms that would have been ecologically dominant over the bulk of the geologic record. Aside from microfossils, sedimentary rocks contain the recycled and amalgamated remnants of past life in the form of organic matter. In the marine realm, organic matter primarily represents the most abundant things in the environment – the base of the food chain – that is, photoautotrophs living in the surface waters. Upon the death of these producers, most (>99%) of their primary organic carbon is remineralized and recycled by various heterotrophic organisms in the water column and sediment water interface. The remaining organic matter is usually composed of recalcitrant compounds or biomolecules (i.e. lipids, pigments, aromatic hydrocarbons), which can be deposited in the sediment and, under the right environmental conditions, remain stable for millions to billions of

years. These sedimentary biomolecules or organic matter can act as chemical fossils and preserve ecological biological specificity in the absence of traditional hard part remains.

The bulk of sedimentary organic matter is bound up and preserved in a phase known as kerogen, which is defined as an insoluble macromolecular structure with organics bound together through complex covalent cross-linkages. The remainder of sedimentary organic matter is defined as readily extractable free organic matter, or bitumen. With increasing time and burial, sedimentary organic matter is subjected to post-depositional processes including diagenesis and catagenesis. Diagenesis encompasses the initial low temperature (up to ~50°C) chemical and physical alterations to organic matter, including the initial formation of kerogen. Catagenesis refers to the thermal stresses (~50-150°C) that produce hydrocarbons from biomolecules over time, such as structural rearrangements to more thermally stable forms and cracking of kerogen bonded compounds to yield mobile bitumen. These processes are dependent on heat and pressure: as burial temperatures increase, catagenesis grades into metagenesis, or the total breakdown of original organic matter into dry gas and other such substances non-diagnostic for biological analysis. If preserved sedimentary organic matter has not experienced these advanced catagenetic or metagenetic effects, the distinct classes of organic biomolecules, their organisms source organisms, and their progression through the processes of diagenesis and catagenesis can be tracked through geologic time. Organic geochemistry is the field of study in which we look to remnant sedimentary organic matter and attempt to classify its parts in order to make meaningful inferences about past biogeochemical cycles, environments, and ecology. Methods in use throughout

this dissertation include describing bulk compositions of organic matter and selectively breaking out individual organic compounds for lipid biomarker analysis.

This dissertation will explore and attempt to untangle some of the base organic geochemical cycles that predominate in ancient environments. I will cover methods and techniques of organic geochemistry that can be utilized to understand biogeochemical cycles, sources of organic matter, and the distributions of primary producers during mass extinctions, hydrological dynamics of ancient rift systems, and the interactions of local environments on global carbon and climate systems.

In the second chapter, I discuss one of the Earth's greatest mass extinction events, the Hangenberg Crisis. This event is the final mass extinction within the overarching series of Late Devonian Mass extinction, representing the transition into the Carboniferous icehouse world. While the Hangenberg Crisis is considered a global event, its cause is uncertain and there has been to date no solid evidence of the exact stratigraphic location of this event within the classic Late Devonian sequence of black shales that make up the bulk of the Eastern United States Appalachian Basin. In order to explore the underlaying biogeochemical cycles that characterized this biotic crisis, and then compare it to the much more well-understood late Devonian Frasnian-Famennian mass extinction, I undertook an exploratory field study in which I measured and sampled a sequence of rocks from the Cleveland Black Shale member of the Ohio Shale in Ohio, USA. Using a multiproxy combination of organic and inorganic chemistry, as well as paleontological interpretations, I was able to delineate the strata temporally coincident with the Hangenberg Crisis in the Appalachian Basin for the first time. From there, I was

able to utilize more organic geochemical proxies such as stable isotopes and lipid biomarker analysis to probe the dynamics of the microbial communities that drove Devonian biogeochemical cycles before, during, and after the extinction event. My results indicate that much of the Devonian water column would have been euxinic, that is, anoxic with abundant free hydrogen sulfide, which represents an environment toxic to most metazoans. Surprisingly, regardless of the ubiquitous euxinic signal, there is an overprinted record of bioturbation, or the traces of past burrowing organisms, which suggests that the seafloor was not continuously devoid of life. Despite highly variable water column and sedimentary redox conditions, as well as the extinction known to be occurring in macrofaunal clades, lipid biomarker evidence shows that there is little to no change in the microbial communities that drive the base of the food chain at any point during this biotic crisis. Microbial communities are stable. Evidence further suggests that proposed transitions in planktic algal communities supposedly driven by the Hangenberg Crisis are, in fact, not visible in the record from the Appalachian Basin.

Having covered a global mass extinction in the Chapter Two, Chapter Three describes a more localized, mechanistic use of organic geochemistry. In particular, this chapter focuses on the hydrological dynamics of the ancient hypersaline lakes of the Newark Basin, part of the failed Jurassic rift system in central New Jersey. Here, I use transitions in lipid biomarker and isotope parameters to track changes in biological sources, which, in turn, indicate changes in the overarching paleoenvironment these source organisms inhabited. A suite of lipid biomarker parameters is able to characterize distinct phases in the hydrological history of the Newark Basin. These phases match

extremely well to published interpretations of sedimentary features, providing excellent constraints on dynamics of infill, stratification, and evaporitic phases. Further, these rift lakes have been proposed as potential sites of high pH in the ancient record. Biomarker and stable isotope parameters clearly indicate distinct phases of increased salinity driven stratification linked to high pH conditions. The highly detailed stratigraphic constraints generated here make this hypersaline lake an ideal natural laboratory to assess the role of variable pH on paleoenvironmental parameters.

In Chapter Four we fast-forward in time to the early-middle Eocene. The Eocene is characterized by changeability in both global carbon and climate cycles, including short-term orbitally-driven hyperthermal events and the Cenozoic switch from greenhouse to long-term icehouse conditions. Despite the utility of the Eocene as an analogue for modern climate change, many questions still exist about the causes of climactic variability, with proposed influences including the input of carbon sources ranging from volcanoes, to widespread wildfires, enhanced methane cycling, and the overturn of the oceanic store of dissolved organic carbon. To help unravel the links between Eocene carbon and climate cycles I obtained a core drilled by the Ocean Drilling Program off the coast of Greenland in the Norwegian-Greenland Sea. This core boasts the most resolved record of early-middle Eocene high latitude sites and represents a typical coastal marine environment that would have experienced the effects of orbitally-driven climate change. Analyses indicate that most preserved organic matter is likely terrigenous in nature, deriving from oxidized soils and inert kerogen. Individual lipid biomarker parameters are complex. Lipid biomarker analysis reveals immature terrestrial organic

matter characterized by abundant hopanoids, diterpenes, and triterpenes, emplaced on a background marine signal. Ratios of angiosperm to gymnosperm input indicate a shift from gymnosperm to angiosperm abundance up-core. Early-middle Eocene sediments from Site 913B appear to record a dynamic nearshore system with periods of strong terrigenous input highly influenced by local controls, thus making correlation to the global carbon cycle difficult. However, continuous deposition of largely inert, terrigenous organic matter suggests a mechanism for carbon sequestration in the warm and wet Eocene polar regions, while the original oxidation of this organic matter source may also provide a source of light carbon to the atmosphere on short time scales.

Lastly, Chapter Five presents a short synthesis and summary of the main findings of this dissertation. I provide a brief commentary of the major outstanding questions pertaining to the aforementioned topics and highlight potential avenues of future research.

CHAPTER TWO

A Stable and Productive Marine Microbial Community was Sustained Through the End-Devonian Hangenberg Crisis Within the Cleveland Shale of the Appalachian Basin, USA

Aaron M. Martinez, Diana L. Boyer, Mary L. Droser, Craig Barrie, Gordon D. Love

Abstract

The end-Devonian Hangenberg Crisis constituted one of the greatest ecological and environmental perturbations of the Paleozoic Era. To date, however, it has been difficult to precisely constrain the occurrence of the Hangenberg Crisis in the Appalachian Basin of the United States and thus to directly assess the effects of this crisis on marine microbial communities and paleoenvironmental conditions. Here we integrate organic and inorganic chemostratigraphic records compiled from two discrete outcrop locations to characterize the onset and paleoenvironmental transitions associated with the Hangenberg Crisis within the Cleveland Shale member of the Ohio Shale. The upper Cleveland Shale records both positive carbon ($\delta^{13}C_{org}$) and nitrogen ($\delta^{15}N_{total}$) isotopic excursions, as well as replenished trace metal inventories with links to eustatic rise. These dual but apparently temporally offset isotope excursions may be useful for stratigraphic correlation with other productive end-Devonian epeiric marine locations. Deposition of the black shale succession occurred locally beneath a redox-stratified water column with euxinic zones, with signs of strengthening denitrification during the

Hangenberg Crisis interval, but with an otherwise stable and algal-rich marine microbial community structure sustained in the surface mixed layer as ascertained by lipid biomarker assemblages. Discernible trace fossil signals in some horizons suggest, however, that bioturbation and seafloor oxygenation occurred episodically throughout this succession and highlight that geochemical proxies often fail to capture these rapid and sporadic redox fluctuations in ancient black shales. The paleoenvironmental conditions, source biota, and accumulations of black shale are consistent with expressions of the Hangenberg Crisis globally, suggesting this event is likely captured within the uppermost strata of the Cleveland Shale in North America.

1. Introduction

The end-Devonian Hangenberg Biotic Crisis (HC; ~359 Ma) is particularly intriguing for both its close temporal proximity and comparable magnitude to the faunal extinction associated with the earlier Frasnian-Fammenian boundary (Kellwasser) event, as well as the dramatic marine community ecological turnover resulting from these combined events (Droser et al., 2000; McGhee et al., 2013). The HC decimated ammonoid, trilobite, conodont, and vertebrate taxa, and marked the end of stromotoporoid sponges, though many affected groups recover in the Carboniferous (Caplan and Bustin, 1999; Sallan & Coates, 2010; McGhee et al., 2013). Numerous extinction mechanisms and triggers have been proposed including: ocean-wide marine anoxia, volcanism, eustatic change, climate fluctuations (Caplan & Bustin, 1999; Marynowski et al., 2012; Carmichael et al., 2015; Racki et al., 2018), and the evolution

and expansion of land plants (by increasing weathering rates and drawing down CO_2; Algeo et al., 1995; Tulipani et al., 2015b), though there were likely synergistic effects operating that contributed to the ecological crisis. The event was likely rapid (calculated duration of ~50-100 ka; Myrow et al., 2014), marked by glaciation, and globally expressed (Kaiser et al., 2015 and references therein). The HC is classically recognized within a predictable succession of lithologies recording eustatic variation. This begins with the deposition of a transgressive organic-rich shale, with the type section being the Hangenberg Black Shale in Germany (Marynowski and Filipiak, 2007; Kaiser et al., 2015). This is in turn overlain by regressive units of gray shales, sandstones, and limestones (Caplan and Bustin, 1999; Kaiser et al., 2015). Despite the global nature of the crisis, limitations on the use of traditional proxies for defining the HC (mainly the use of the *Siphonodella praesulcata* conodont zone and positive $\delta^{13}C_{carb}$ excursions) have arisen, prompting the improvement and integration of bio-, litho-, and chemo-stratigraphies to identify the crisis interval (Carmichael et al., 2015; Corradini et al., 2017; and references therein). In particular, suites of $\delta^{13}C_{org}$, sea level, and redox proxies have been shown to viably define the Hangenberg interval, combined with insight from biostratigraphy (Kaiser, 2005; Carmichael et al., 2015; Kaiser et al., 2015;). The HC remains ambiguously defined within end-Devonian shales in the Appalachian Basin of North America, due, in part, to the lack of lithological variability (no extensive $\delta^{13}C_{carb}$ record) and the scarcity of diagnostic conodonts (Over et al, 2007, Carmichael et al., 2015; Kaiser et al., 2015). Additionally, this area hosts an abundance of disconformable

sections in close temporal association with this event, which makes stratigraphic correlation and thus testing of specific causes and consequences difficult.

The organic-rich Cleveland Shale member of the Ohio Shale is well known for preserving some of the most spectacular arthrodire fish fossils, including their ultimate demise within thick, well exposed packages of black shale, as well as for being loosely associated with multiple Late Devonian biocrises, including the HC (Zagger, 1995; Sallan & Coates, 2010; Baird et al., 2013). Previous work has described miospores broadly characteristic of the end-Devonian (LN miospore zonation) from the uppermost Cleveland Shale (Eames, 1974), consistent with ammonoids described up to 3 m below the expression of the overlaying Bedford Formation, and the identification of the middle or upper *Siphonodella praesulcata* conodont zone (House et al., 1986; Zagger, 1995). Geochemically, wide-ranging localities of the Cleveland Shale have been well-characterized, with a general consensus of strengthening anoxia within the uppermost strata (Jaminski et al., 1998; Algeo et al., 2007; Rimmer et al., 2010). Combined, this evidence suggests that deposition of the uppermost strata of the Cleveland Shale may be approximately coeval with the occurrence of the Hangenberg Black Shale in Europe.

While the effects of the global HC on both marine and terrestrial macrofauna are well-studied, less is known about the impact this biocrisis had on the phytoplankton and other microorganisms that provided the primary biomass that sustained food webs and controlled Paleozoic biogeochemical cycles (for example, Marynowski and Filipiak, 2007; Cao et al., 2009; Marynowski et al., 2012; Rohrssen et al., 2013; Tulipani et al., 2015a; Whiteside and Grice, 2016). Lipid biomarkers, biomolecules that are recalcitrant

on geologic timescales, can be used to distinguish sources of organic matter input and characterize fundamental aspects of the microbial ecology of an environment during sedimentary deposition, if the host strata have undergone a mild thermal history (Peters et al., 2005). For instance, the ratio of the major (C_{27}-C_{35}) hopanes to (C_{27}-C_{30}) steranes (H/S) provides a broad but informative comparison of the relative contribution of bacteria and eukaryotes to sedimentary organic matter, where hopanes and steranes are the core hydrocarbon skeletons derived from bacterial hopanols and eukaryotic sterols, respectively (Peters et al., 2005; Rohrssen et al., 2013). Other biomarker compounds provide additional source organismal and paleoenvironmental selectivity. Green sulfur bacteria (Chlorobi), which are anoxygenic phototrophs, can utilize hydrogen sulfide as an electron donor and synthesize distinctive aromatic hydrocarbon pigment biomarkers (such as the C_{40} carotenoid isorenieratene, preserved in ancient sediments after diagenesis as isorenieratane), which are useful for recognition of episodes of photic zone euxinia (PZE, Summons & Powell, 1986) extending into surface waters.

To investigate evidence for significant changes within the microbial communities associated with the transitions into and out of the HC, we have integrated organic (lipid biomarker analyses as well as stable carbon and nitrogen isotopic measurements) and inorganic geochemical data with sedimentary ichnofabric evaluation to generate detailed chemostratigraphic records for thermally-immature (early oil window maturity) strata of the upper Cleveland Shale, from two outcrop locations. Here, for the first time, we identify the onset of the HC in the Cleveland Shale through $^{13}C_{org}$ trends and combined inorganic and organic redox proxies and utilize lipid biomarker assemblages to

investigate the stability of the microbial community structure, modes of primary productivity, and marine redox structure leading up to and through this biocrisis at these locations.

2. Geologic setting

During the latest Devonian (Upper Famennian), the region of northern and central Ohio was located within a low latitude (~25°S) epicontinental foreland basin situated between the Acadian uplands to the east and the Michigan and Illinois basins to the northwest and southwest, respectively, and was situated on the eastern flank of the Cincinnati Arch. Within the western part of this basin, the Ohio Shale was deposited as a distal expression of the Catskill Delta (Lewis and Schweitering, 1971; Ettensohn, 1985; Woodrow et al., 1988). The Cleveland Member of the Ohio Shale is a thick (up to 30 m) fissile to platy black shale that is interpreted to represent deposition below storm wave base during a transgression (Hellstrom & Babcock, 2000; Baird et al., 2013). Decimeter-scale cyclicity due to climactically controlled variations in organic and clastic content is present in the Cleveland Shale strata and, at some localities, the top few meters are interpreted to reflect glaciation as evidenced by large dropstones, presumably from ice-rafted materials (Jaminski et al., 1998, Brezinski et al., 2010; Baird et al., 2013). The Cleveland Shale is overlain by the Bedford Formation, here called the Bedford Shale, which consists of a gray to buff colored shale, with the Euclid Siltstone Member near its base, which are in total representative of the regressive units overlaying the Hangenberg black shale in Europe. We sampled strata from two outcrop sections: 1) Big Creek on

Tiedeman Road (TR) in Cleveland, Ohio and 2) Rocky Branch Creek (RB) in Gahanna, Ohio (**Fig. 2.1**), which are approximately 150 km apart. Both sites are sparsely fossiliferous and lack apparent bedforms within the Cleveland Shale. Additionally, both sites preserve a distinctive dark-gray, weakly bioturbated ~10 cm gradational conformable contact that serves as a transition between the uppermost Cleveland Shale to the overlying Bedford Formation. At TR, this transitional layer grades into half a meter of homogenized dark gray shale (Bedford Shale), then overlain by coarser, clastic material of the Euclid Sandstone. The Euclid Sandstone is not present at RB, which shows the same ~10 cm gradational contact from black into a homogenized gray shale, but instead expresses meters of the Bedford Shale with intermittent coarse-grained, sideritic layers. We use this unique gradational contact as a marker bed for the top of the Cleveland Shale.

3. Samples and methods

Samples for bulk organic chemistry, organic carbon and nitrogen isotopes, trace metal geochemistry, lipid biomarker analysis, and ichnofabric indicies were taken from freshly exposed surfaces in creek beds (July: 2014, 2015). Samples were collected as large blocks (> 200 g) to further minimize weathering edge effects. Approximately 15m and 2.8m of Cleveland Shale thickness are exposed and sampled below the Cleveland—Bedford contact at TR and RB, respectively. Sampling at RB was limited by available exposures.

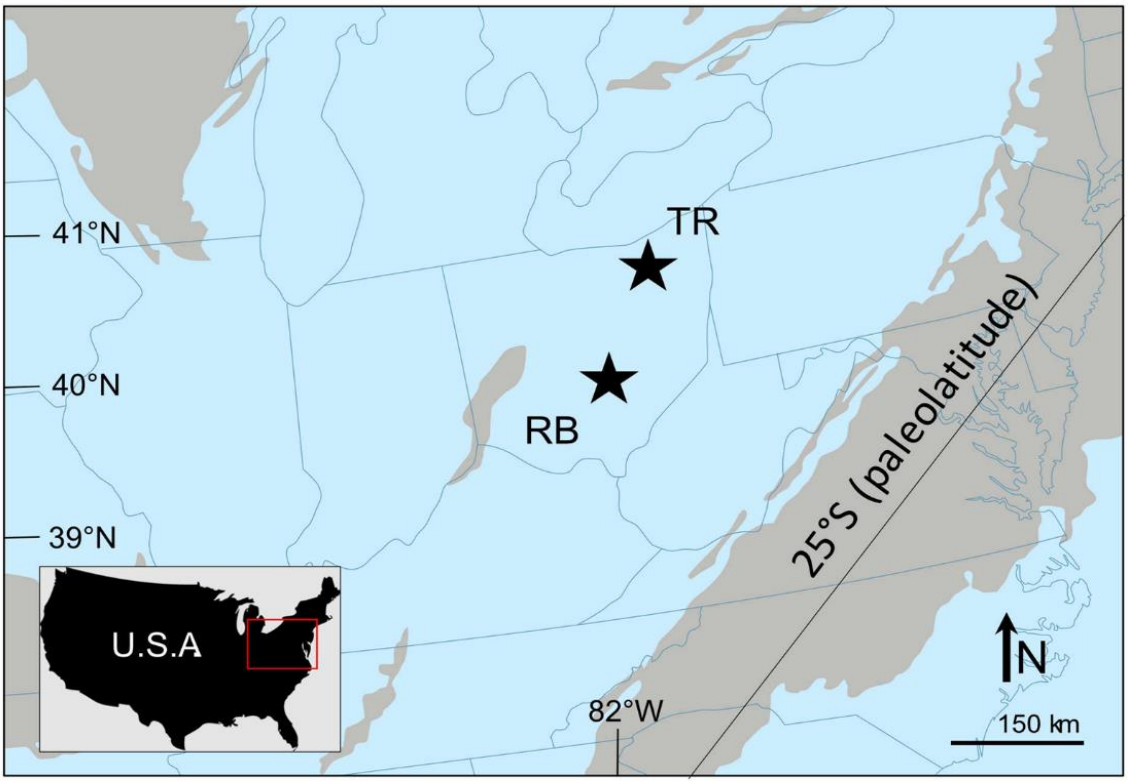

Figure 2.1: **Sample area.** Late Devonian paleogeography with modern Ohio outcrop locations for Tiedeman Road (TR) and Rocky Branch (RB). Paleogeography modified from Algeo et al. (2007). Darker shaded areas represent continental masses.

3.1. Rock-Eval Pyrolysis

Approximately 100 milligrams of washed, ground (60 mesh) whole rock sample were analyzed in a Rock-Eval II instrument. Measurements include S1: free bitumen content (mg HC/g rock); S2: remaining generation potential (mg HC/g rock); Tmax: temperature at maximum evolution of S2 hydrocarbons (°C); and S3: organic carbon dioxide yield (mg CO_2/g rock), and were generated by heating according to the following parameters S1: 300°C for 3 minutes; S2: 300°C to 550°C at 25°C/min, held at 550°C for 1 minute; S3: trapped between 300 to 390°. Instrument calibration was achieved using a rock standard with values determined from a calibration curve to pure hydrocarbons of

varying concentrations. This standard was analyzed every 10 samples as an unknown to check the instrument calibration. The standard deviation was considered acceptable under the following guidelines: T_{max}, ±2°C; S1, 10% variation from established value; S2, 10% variation from established value; S3, 20% variation from established value.

3.2. LECO TOC

Total organic carbon contents were determined at GeoMark Research using a LECO C230 instrument. Samples were decarbonized with concentrated HCl for at least two hours, rinsed through a filtration apparatus to remove the acid, dried at low temperature and weighed to obtain %carbonate based on weight loss, then combusted on the LECO C230. The LECO C230 instrument was calibrated with standards having known carbon contents. Standards were combusted by heating to 1200°C in the presence of oxygen; both carbon monoxide and carbon dioxide were generated, and the carbon monoxide was converted to carbon dioxide by a catalyst. The carbon dioxide product mass was measured by an IR cell. Combustion of unknowns was then completed and the response of unknowns per mass unit was compared to that of the calibration standard. Standards were analyzed every 10 samples to check variation and calibration of the analysis. Acceptable standard deviation for TOC is 3% variation from established value.

3.3. Carbon and nitrogen isotopes

For isotopic analysis, samples were washed with 1 M hydrochloric acid to remove any carbonate material prior to isotopic measurement of the organic material. The

remaining organic residue was measured for bulk carbon ($\delta^{13}C$) and nitrogen ($\delta^{15}N$) isotope signatures using an Elementar Isotope Select cube elemental analyzer (EA) coupled to a VisION isotope ratio mass spectrometer (IRMS). Samples and standards were weighed out on a Mettler Toledo microbalance (ranging from 5 mg to 40 mg depending upon organic content) and loaded into the EA autosampler. Stable isotope results for 12/13C are reported as $\delta^{13}C$ relative to VPDB in permil (‰) and calibrated using certified international standards (USGS24 & NBS22). The reported standard deviation for all carbon isotope measurements is ±0.1‰. Stable isotope results for 14/15N are reported as $\delta^{15}N$ relative to air in permil (‰) and calibrated using certified international standards (USGS25, IAEA-N-1 & IAEA-N-2). The reported standard deviation for all nitrogen isotope measurements is ±0.2‰.

3.4. Trace metals

Samples were powdered for whole rock trace metal analysis by solution using conventional methods on a quadrupole ICP-MS (Varian 820MS, now Analytik Jena; Inductively Coupled Plasma-Mass Spectrometer) at SUNY Oswego. Approximately 400 mg of powdered sample were ashed at 850°C for 12 hours, and then dissolved in a three acid (HNO_3, HCl, HF) total digestion. Mean duplicability of sample solution analyses (repeat measurement of the same solution) over the full range of concentration encountered was ±12%.

A subset of samples was analyzed for trace metal concentrations at UCR with slight changes in methodology to verify reproducibility. To make the most complete data

sets, TR metal data is reported from Oswego generated data and RB from UCR generated data. Procedure for UCR is as follows: total solid-phase iron (Fe_T) and aluminum (Al) concentrations were determined on ashed samples (600 °C) using a three-step digestion method (HNO_3/HCl/HF at 140°C). Final concentrations were determined on an Agilent 7900 ICP-MS with100-fold dilution in trace-metal grade 2% HNO_3. Reference standards SDO-1 (Devonian Ohio Shale) and SCO-1 (Cody Shale) were digested and analyzed in parallel with the sample extractions and yielded errors of less than <2%, <2%, and <3% for total Fe, Mo, and Al, respectively. TR datapoints produced at UCR were comparable to Oswego generated data.

3.5. Lipid biomarkers

Methods for extracting and characterizing lipid biomarkers for the Cleveland Shale follow those of Haddad et al. (2016). Trimmed, inner portions of rock samples were solvent cleaned in a sequence of ultrapure water, methanol (MeOH), dichloromethane (DCM), *n*-hexane, and DCM then powdered in a zirconia ceramic puck mill in a SPEX 8515 shatterbox. Crushed rock powders (typically 5 g for black shales, and between 10-55 g for gray shales and siltstones) were extracted in a CEM Microwave Accelerated Reaction System (MARS) at 100°C in a 9:1 DCM:MeOH (v/v) mixture for 15 min. Elemental sulfur was removed from the total lipid extract (TLE) using copper pellets activated with hydrochloric acid and rinsed with deionized water, methanol, dichloromethane, and *n*-hexane. Saturate hydrocarbon and aromatic fractions were obtained by silica gel column chromatography; the saturate hydrocarbon fractions were

eluted with 1.5 dv of *n*-hexane and the aromatic hydrocarbon fractions with 4 dv of a 1:1 (v/v) mixture of DCM and *n*-hexane. Asphaltenes and maltenes were not separated before chromatography. Full laboratory procedural blanks with pre-combusted sand were performed in parallel with each batch of rocks to ensure that any background hydrocarbon compounds were negligible in comparison with biomarker analyte abundances.

Saturated hydrocarbon fractions were analyzed by metastable reaction monitoring–gas chromatography–mass spectrometry (MRM–GC–MS) conducted at UC Riverside on a Waters AutoSpec Premier mass spectrometer equipped with a HP 6890 gas chromatograph and a DB-1MS coated capillary column (60 m x 0.25 mm, 0.25 μm film) using He as a carrier gas. The GC temperature was programmed with an initial hold at 60ºC for 2 min, then heating to 150ºC at 10ºC/min rate, followed by heating to 320ºC at 3ºC/min rate and a final hold for 22 min; analyses were performed via splitless injection in an electron impact mode, with an ionization energy of 70 eV and an accelerating voltage of 8 kV. MRM transitions for C_{27}–C_{35} hopanes, C_{31}–C_{36} methylhopanes, C_{21}–C_{22} and C_{26}–C_{30} steranes, C_{30} methylsteranes and C_{19}–C_{26} tricyclics were monitored. Procedural blanks with pre-combusted sand yielded less than 0.1 ng of individual hopane and sterane isomers per gram of combusted sand. Polycyclic biomarker alkanes (tricyclic terpanes, hopanes, steranes, etc.) were quantified by addition of a deuterated C_{29} sterane standard [d4-ααα-24-ethylcholestane (20R); 50 ng] to saturated hydrocarbon fractions and comparison of relative peak areas. Yields assume equal mass spectral response factors between analytes. Analytical errors for individual hopanes and

steranes concentrations are estimated at plus/minus 30%. Average uncertainties in hopane and sterane biomarker ratios are plus/minus 8% as calculated from multiple analyses of saturated hydrocarbon fractions from oil standards.

The saturated and aromatic hydrocarbon fractions were analyzed in both full scan and single ion monitoring methods at UC Riverside by gas chromatography–mass spectrometry (GC–MS) on an Agilent 7890A GC system coupled to an Agilent 5975C inert MSD mass spectrometer. The GC temperature program was 60ºC (held for 2 min), heated to 150ºC at 20ºC/min, then to 325ºC at 2ºC/min, and held at 325ºC for 20 min. The GC was equipped with a DB1-MS capillary column (60 m x 0.32 mm, 0.25 μm film thickness) and helium was used as a carrier gas. 200 ng of d14-p-terphenyl standard was added to each aromatic hydrocarbon fraction for quantification. Pristane/phytane (Pr/Ph) ratios were measured from relative peak areas using total ion chromatograms acquired from full scan analysis. Chlorobi-derived carotenoid biomarkers, including aryl isoprenoids, isorenieratane, and paleorenieratane were identified based on 133 and 134 Dalton (Da) mass chromatograms, with 3,4,5- and 2,3,6-trimethyl-substituted aryl isoprenoid abundances measured from peak areas in 133 Da ion chromatograms, with isorenieratane and paleorenieratane verified from mass spectra and retention times.

3.6. Ichnofabric Index

To analyze ichnofabric index, samples were slabbed perpendicular to bedding to reveal a cross-section. The slabbed section was polished with 800 level grit to remove saw marks and digitally scanned at a resolution > 400 dpi. Scans were then evaluated for

burrowing activity for each vertical cm of rock. Since ichnofabric index values can vary vertically through individual hand samples, ichnofabric index was generated for each cm in a sample (averaging 4 cm in width), then averaged to give a whole-slab estimate.

4. Results

4.1 Total organic carbon contents and Rock-Eval Pyrolysis parameters

Total organic carbon (TOC) contents for the upper Cleveland Shale are moderate to high, ranging from 0.69 wt% to 9.5 wt% (median of 4.2 wt%; **Fig. 2.2a and 2.3a**). TOC is appreciable throughout all samples, with notable spikes in the top 3 m of Cleveland Shale before falling sharply at the contact with overlying Bedford Formation. Rock-Eval pyrolysis parameters, particularly hydrogen indices (HI) in the range of 435-658 mg/g TOC for the black shales, indicate good petroleum source rock potential and are consistent with a thermally immature (early oil window) marine sedimentary organic matter (see **Table 2.1** for Rock-Eval data). These rocks are hence ideal targets for detailed biomarker investigation. HI values drop considerably into the gray Bedford shales, suggesting a shift to more terrestrially derived organic matter. The following data can be found in **Table 2.2, 2.3, and 2.4** at the end of the chapter.

4.2 Carbon isotopes

$\delta^{13}C_{org}$ values for the Cleveland Shale at the TR section remain close to a typical Paleozoic marine baseline of -29‰ with a +1.3‰ magnitude positive excursion (-29.3‰ to -28.0‰; **Fig. 2.2b**), centered at 3 m depth below the top of the section. This progresses into the coarser, clastic rocks of the Bedford Shale where $\delta^{13}C_{org}$ values become

considerably more ^{13}C-enriched (max -25.3‰) associated with a lithologic and organic-facies change and likely a significant increase in terrestrial (higher plant) biomass input (as suggested by Rock-Eval and lipid biomarker characteristics; see **Fig. 2.4**). The $\delta^{13}C_{org}$ values at the RB locality also remain close to a typical baseline of -29‰ and record no significant excursions within the black shale package (**Fig. 2.3b**). There is a pronounced shift to a more ^{13}C-enriched $\delta^{13}C_{org}$ within the top 10 cm of the Cleveland Shale at RB, again likely associated with the lithologic and organic facies shift leading into the gradational contact with the Bedford Shale.

4.3 Sedimentary molybdenum concentrations

Nearly half of all TR samples record Mo concentrations greater than 100 ppm (**Fig. 2.2c**). Values steadily increase from 40 to 121 ppm before the onset of the $\delta^{13}C_{org}$ excursion. Following the $\delta^{13}C_{org}$ excursion, sedimentary Mo behavior changes, beginning to fluctuate from moderately to highly enriched values (median of 106 ppm, range = 18-673 ppm). The RB section shows a single enriched Mo concentration 2.7 m below the Cleveland—Bedford contact (**Fig. 2.3c**, 144 ppm). Mo values at RB drop to low and stable levels (avg. of 16 ppm, but still higher than typical crustal baseline values of ca. 1-3 ppm) for the remainder of the black shale interval.

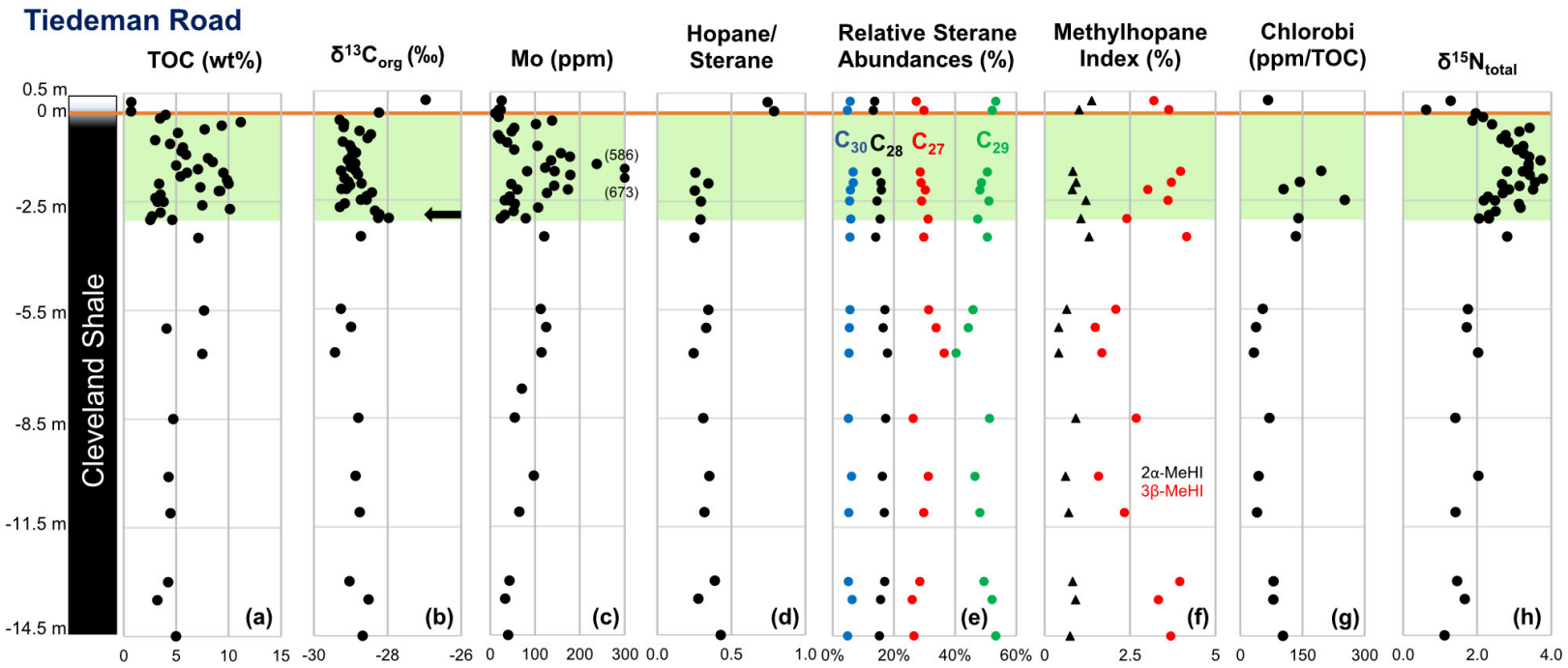

Figure 2.2: Chemostratigraphic records compiled for Tiedeman Road (TR section). The orange bar at 0 m indicates the lithological transition from the Cleveland Shale to the Bedford Formation. Green shaded region is the proposed Hangenberg Crisis interval following the peak $\delta^{13}C_{org}$ illustrated by the black arrow. Parameters include: (a) total organic carbon (TOC); (b) $\delta^{13}C_{org}$ ‰ (vs. VPDB); (c) Molybdenum (Mo) concentration (ppm of rock); (d) $C_{27\text{-}35}$ Hopane/ $C_{27\text{-}30}$ Sterane ratio; (e) relative abundance (percentage) of total $C_{27\text{-}30}$ steranes; (f) 2α- & 3β-Methylhopane index (2α-MeHI, triangles; 3β-MeHI, circles), where 3β- and 2α-MeHI was calculated from the percentage abundance of the C_{31} methylhopane relative to sum of (C_{31} methylhopane + C_{30} αβ-hopane); (g) overall summed abundance of Chlorobi biomarkers including isorenieratane, paleorenieratane, and their aryl isoprenoid fragments (C_{13}-C_{24}); and (h) $\delta^{15}N_{total}$ ‰ (vs. air).

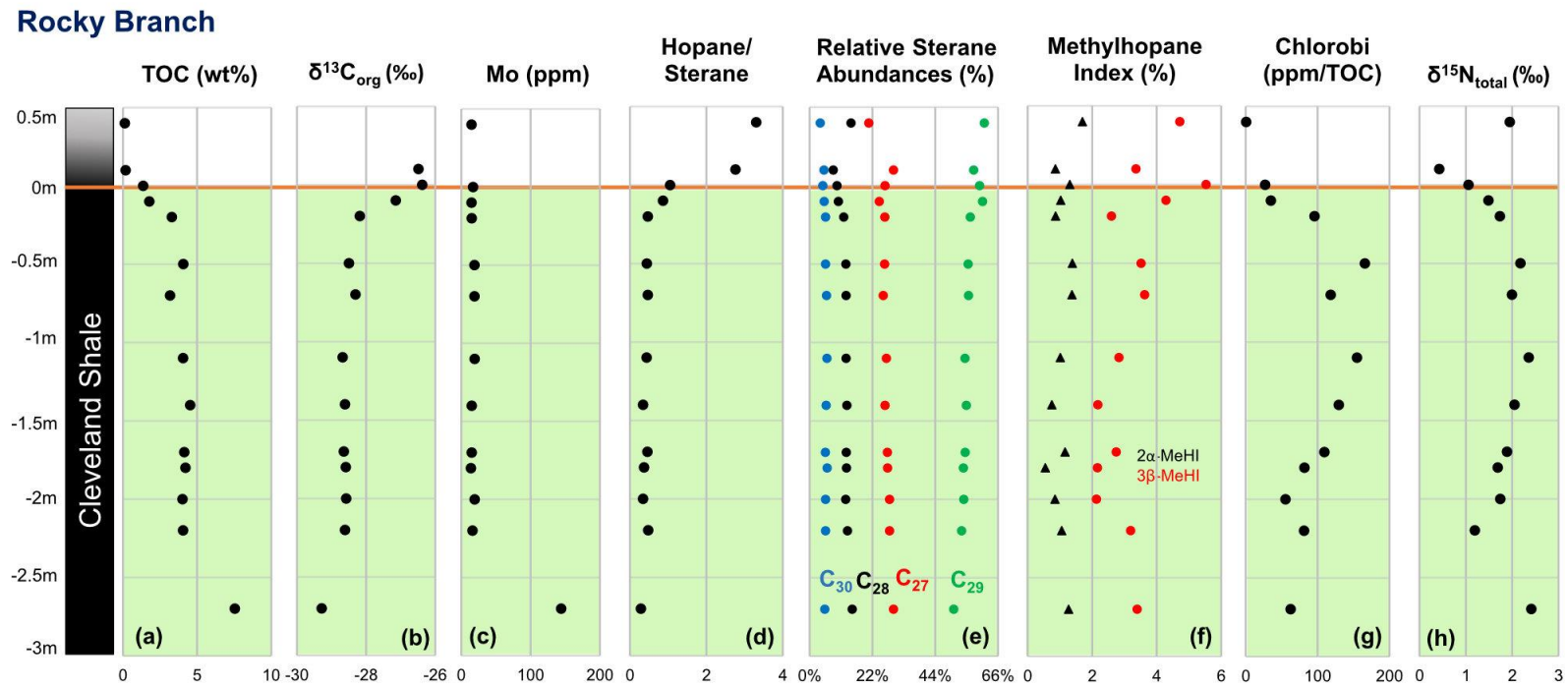

Figure 2.3: Chemostratigraphic records compiled for Rocky Branch (RB section). The orange bar at 0 m indicates the lithological transition from the Cleveland Shale to the Bedford Formation. Green shaded region is part of the proposed Hangenberg Crisis interval. Parameters include: (a) total organic carbon (TOC); (b) $\delta^{13}C_{org}$ ‰ (vs. VPDB); (c) Molybdenum (Mo) concentration (ppm of rock); (d) $C_{27\text{-}35}$ Hopane/ $C_{27\text{-}30}$ Sterane ratio; (e) relative abundance (percentage) of total $C_{27\text{-}30}$ steranes; (f) 2α- & 3β-Methylhopane index (2α-MeHI, triangles; 3β-MeHI, circles), where 3β- and 2α-MeHI was calculated from the percentage abundance of the C_{31} methylhopane relative to sum of C_{31} methylhopane and C_{30} αβ-hopane; (g) overall summed abundance of Chlorobi biomarkers including isorenieratane, paleorenieratane, and their aryl isoprenoid fragments (C_{13}-C_{24}); and (h) $\delta^{15}N_{total}$ ‰ (vs. air). The transition from the Cleveland Shale into the more oxic and terrestrially derived Bedford Shale is clearly marked by changing H/S ratios, heavier $\delta^{13}C_{org}$, and a drop in Chlorobi markers.

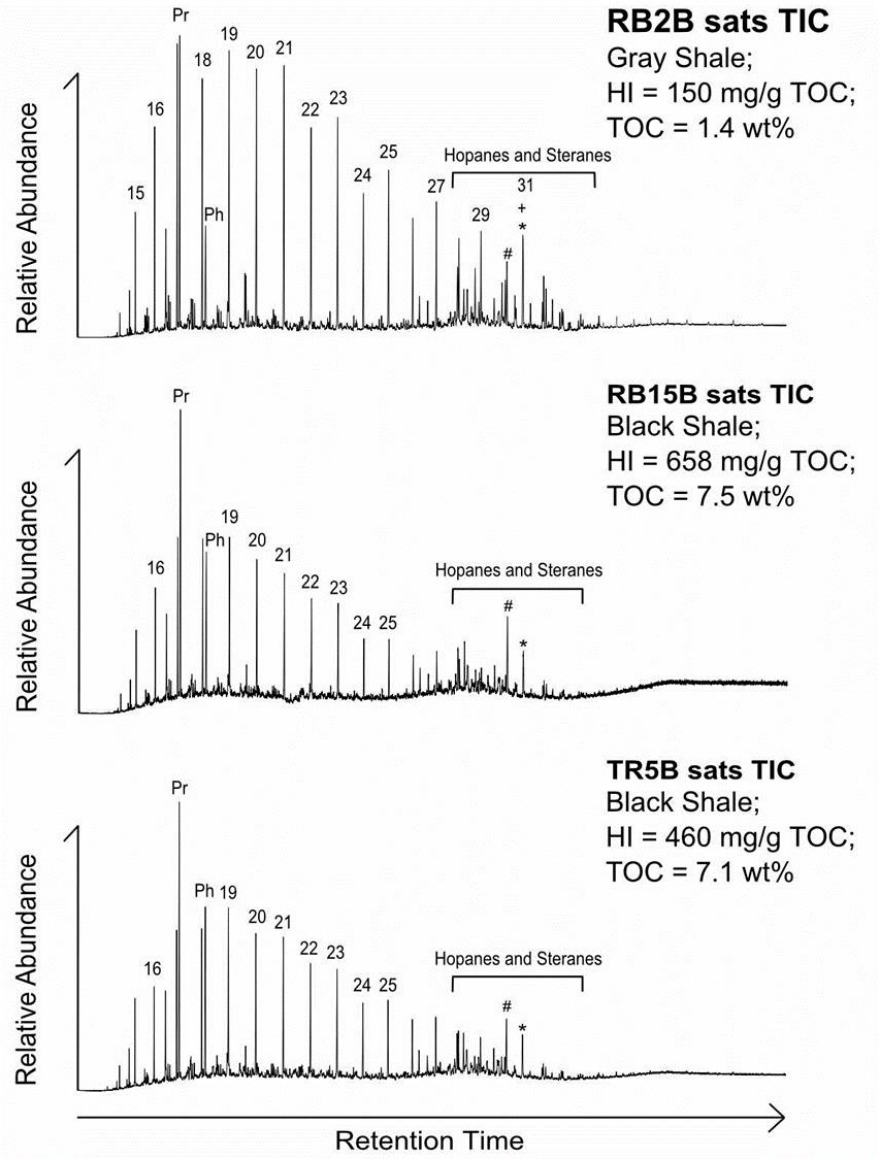

Figure 2.4: Representative total ion current chromatograms for saturated hydrocarbon fractions from rock bitumens (extracts) from the RB and TR sections. Pr = pristane; Ph = phytane; numbers indicate chain length of normal alkanes; # = C_{29}-ααα*R* sterane; * = C_{30}-αβ hopane; 31 + * = co-elution of the n-C_{31} alkane and C_{30}-αβ hopane. RB15B and TR5B represent a typical marine Cleveland Shale signal: high total organic carbon (TOC) and hydrogen index (HI), with a *n*-alkane profile that tails in abundance above *n*-C_{19} with a slight odd-over-even carbon number preference. The RB2B sample profile, transitioning into the overlaying Bedford Shale, shows a discernible terrestrial organic matter influence in the form of lower HI values, a greater contribution of long chain (C_{23-31}) *n*-alkanes with a more prominent odd carbon number preference from plant waxes, higher Pr/Ph ratio, and a higher hopane/sterane ratio.

4.4 Lipid biomarkers

Throughout both sections, the hopane/sterane (H/S) ratio is consistently low with a median of 0.35 for the combined localities (**Fig. 2.2d and 2.3d**), which is lower than the typical Phanerozoic marine average range of 0.5-2.0 for organic-rich oils and rocks (Peters et al., 2005; Cao et al., 2009). Such low H/S ratios indicate a high relative abundance of eukaryotic source organisms, in this case predominantly from marine algae. Steranes can be further classified by the total number of carbon atoms and the structural features within the hydrocarbon skeleton. C_{29} sterane carbon number predominance is found throughout both sections (C_{29} comprises generally > 50% of total C_{27}-C_{30} steranes; **Fig. 2.2e, 2.3e and 2.5**), which is characteristic of high inputs from green algae (Peters et al., 2005; Schwark and Empt, 2006; Kodner et al., 2008). Sterane number patterns are largely invariant throughout both sections, with C_{27}, C_{28}, and C_{30} steranes respectively accounting for a median 28%, 14%, and 5% of the total sterane pool (**Fig. 2.2e, 2.3e and 2.5**). Multiple hopane and sterane stereoisomer ratios for determining thermal maturity indicate that these samples have undergone a mild thermal burial history and are at an early oil window-stage of maturity [C_{27} hopane Ts/(Ts +Tm) and C_{29} sterane (20S/20S+R) ratios; **Fig. 2.4 and 2.5, Table 2.1**; Peters et al., 2005], consistent with the Rock-Eval pyrolysis parameters.

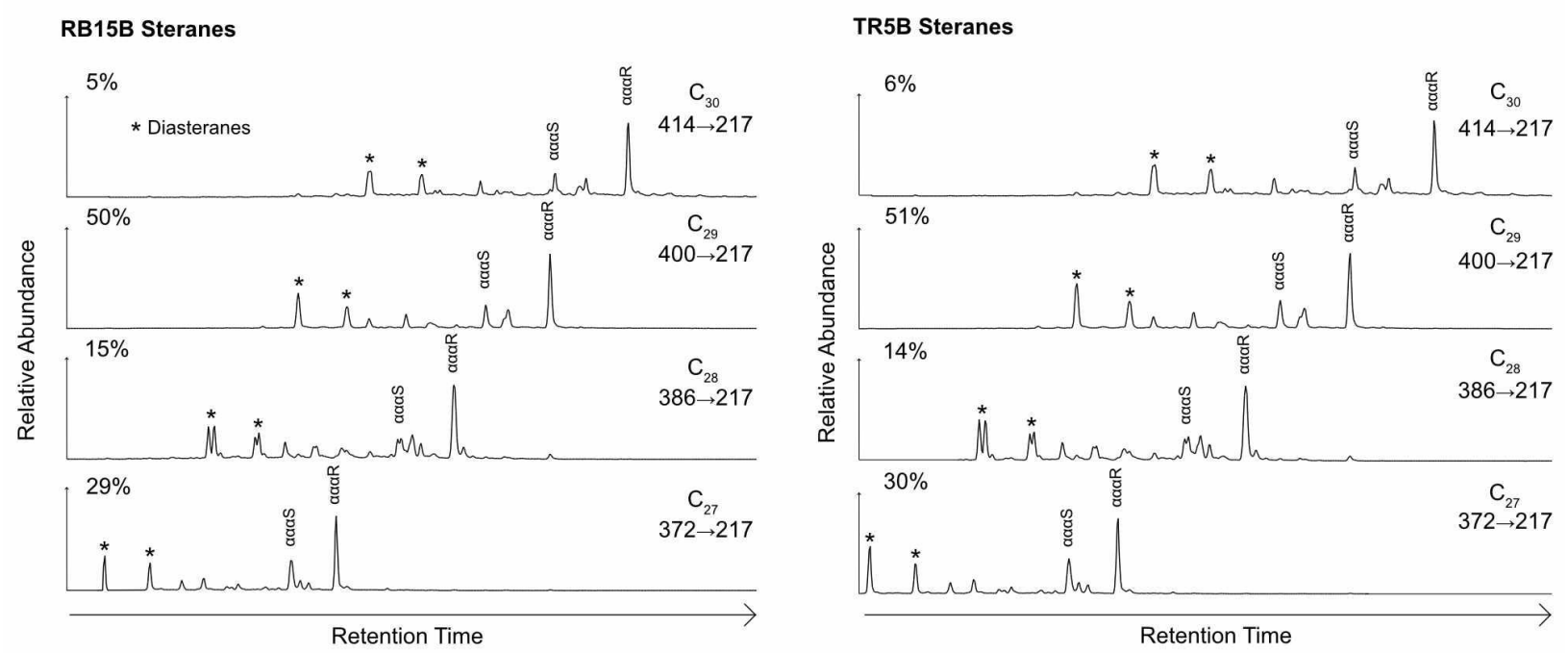

Figure 2.5: Representative MRM-GC-MS sterane traces for RB and TR sections. C_{29} steranes (shown through the 400-217 Da ion transition) are the most abundant amongst the C_{27}-C_{30} steranes, indicating a predominance of the green algal clade that is typical for Paleozoic marine environments (Schwark and Empt, 2006). The dominance of the immature ααα*R* stereoisomer for each sterane carbon number is consistent with the low thermal maturity of the host rocks (early oil window-maturity) as also gauged from Rock-Eval pyrolysis. The C_{30} sterane distributions are dominated by 24-*n*-propylcholestanes which are predominantly sourced by marine pelagophyte algae. Diasteranes (C_{27-30} -αβ and -βα) are also discernible in the profiles, typical for shale and siltstone lithologies containing clay minerals.

Methylhopane contents, expressed as the C_{31} 2α- and 3β-methylhopane indices (2α-MeHI; 3β-MeHI; where 2α- and 3β -MeHI are the percentage abundances of the particular C_{31} methylhopane relative to sum of C_{31} methylhopane and C_{30} αβ-hopane) are generally low absolute values similar in range to those reported previously for Frasnian-Famennian black shales (Haddad et al., 2016). Median values here reach 0.8% and 3.2% at TR and 1.0% and 3.0% at RB for 2α-MeHI and 3β-MeHI, respectively (**Fig. 2.2f and 2.3f**). The 3β-MeHI values records sporadic, slight enrichments occasionally just above 4% for both sections of black shale, but generally the 2- and 3-methylhopane content of our rocks is low, unexceptional, and around marine Phanerozoic average values (Peters et al., 2005; Cao et al., 2009).

Aromatic carotenoid biomarkers (isorenieratane, paleorenieratane, and their aryl isoprenoidal fragments) sourced from Chlorobi are found in high abundance in every sample of black shale (**Fig. 2.2g and 2.3g**) providing strong evidence for at least episodic photic zone euxinia (PZE) in the water column at both localities. Paleorenieratane is a structural isomer of isorenieratane that is typically found in Paleozoic-aged rocks (particularly common in Devonian-age source rocks) and provides strong support for carotenoid biomarker syngeneity (French et al., 2015). Paleorenieratane is of comparable or greater abundance to isorenieratane in the black shales from both sections. Summed concentrations range from 33-103 ppm/TOC throughout most of the Cleveland Shale, but consistently remain over 100 ppm/TOC within 3 m of the Cleveland-Bedford contact (TR max = 252 ppm/TOC, RB max 166 = ppm/TOC). A potential caveat to correctly interpreting the positive δ^{13}Corg excursion found at TR is the elevated presence of

Chlorobi biomarkers, which utilize the reverse tricarboxylic acid (rTCA) pathway to assimilate carbon, leading to more ^{13}C-enriched biomass than photosynthesizers utilizing the Calvin Cycle; however, Chlorobi concentrations are not significantly correlated with $\delta^{13}C_{org}$ patterns (Spearman's Rho: R28 = 0.051, p = 0.398). The aryl isoprenoid ratio (AIR), defined as the proportion of short-chain (C_{13}–C_{17}) to intermediate-chain (C_{18}–C_{22}) aryl isoprenoids, is consistently very low for both sections (TR median = 0.67, max = 1.19; RB median = 0.59, max = 0.89; **Fig. 2.6**). There is no obvious correlation, however, between the overall abundance of aryl isoprenoid compounds and the AIR values.

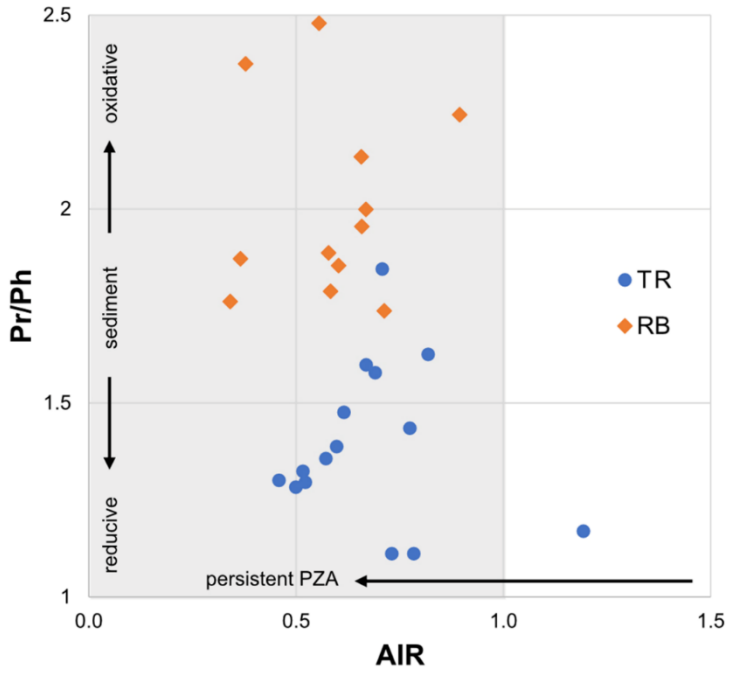

Figure 2.6: **Aryl isoprenoids.** Cross-plot of aryl isoprenoid ratio [AIR; calculated from (C_{13}–C_{17})/(C_{18}–C_{22}) for the 2,3,6-trimethylated aryl isoprenoid series in 133 Da ion chromatograms] values versus pristane/phytane (Pr/Ph) ratio. The grey shaded area contains AIR values that indicate inferred "persistent" photic zone anoxic/euxinic conditions while higher AIR values indicate "episodic" photic zone anoxia/euxinia (PZA; Schwark and Frimmel, 2004). Pr/Ph ratios between 1.0 and 3.0 are unexceptional and do not necessarily indicate strongly reducing conditions (Peters et al., 2005). There is, however, a discernible separation between TR (blue circle) and RB (orange diamond) samples in this plot.

4.5 Nitrogen isotopes

Total sedimentary organic nitrogen isotopic data reveal a general increase in $\delta^{15}N_{total}$ towards the upper part of the Cleveland Shale with a well-defined and systematic 1.9‰ positive excursion evident at TR, ranging from +1.9‰ to +3.8‰ (**Fig. 2.2h**). Baseline values range from 0-2‰ for the remainder of the succession. There is no obvious excursion at RB, which records a lower magnitude range of +1.2‰ to +2.4‰ $\delta^{15}N_{total}$ values within the Cleveland Shale (**Fig. 2.3h**).

4.6 Ichnofabric indices

The ichnofabric index is a semi-quantitative metric of the extent of bioturbation that is reflective of bottom water oxygenation, since bilaterian organisms capable of burrowing require molecular oxygen to support their metabolisms (Droser & Bottjer, 1986; Boyer & Droser, 2009). Within this system, values range incrementally from laminated sediments (ichnofabric index = 1) as unbioturbated, indicating a lack of oxygen needed for burrowing organisms, through fully homogenized sediments (ichnofabric index = 5), considered completely oxygenated and supportive of a diverse infaunal community (Droser & Bottjer, 1986). Cleveland Shale ichnofabric indices range from 1-3 with the majority falling between laminated (anoxic) and intervals of minor laminae disruption (transient bottom water oxygenation; average ichnofabric index = 1-2, **Fig. 2.7**). Bioturbation increases dramatically at the Cleveland-Bedford contact at both localities and upwards into the overlying coarser-grained siltstone rocks, up to ichnofabric index 5, indicative of a more oxic setting occurring above the black shales.

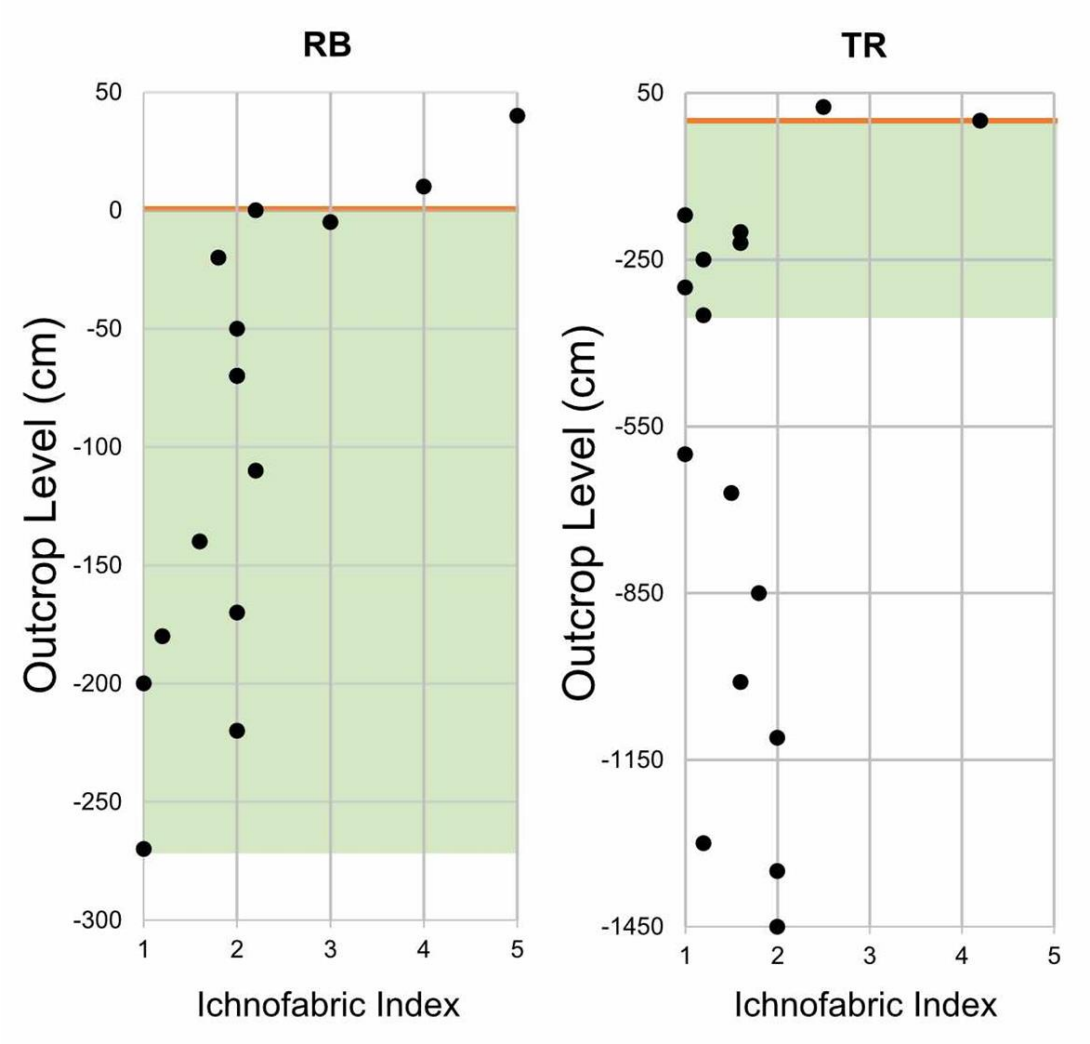

Figure 2.7: Ichnofabric index for Rocky Branch (RB) and Tiedeman Road (TR) localities. The orange bar at 0 cm indicates the lithological transition from the Cleveland Shale to the Bedford Shale. Green shaded region is the proposed Hangenberg Crisis interval. Bioturbation is low but constant throughout the deposition of both sections and increases in the Bedford.

5. Discussion

5.1. Characterizing the Hangenberg Crisis in the Cleveland Shale

The Hangenberg Crisis event interval had first to be identified from chemostratigraphic markers of the upper Cleveland Shale in order to assess the nature and stability of the local marine community structure and paleoenvironmental conditions leading up to and through this event. In addition to a characteristic positive organic carbon isotope excursion, the onset of Hangenberg black shale deposition elsewhere is usually associated with a sharp sea-level rise and a locally euxinic (anoxic with free hydrogen sulfide) water column (Marynowski and Filipiak, 2007; Kaiser et al., 2015). The ~2‰ positive excursions in both $\delta^{13}C_{org}$ and $\delta^{13}C_{carb}$ found by Kaiser (2005) near the base of the Hangenberg black shale in Europe mirror the +1.3‰ $\delta^{13}C_{org}$ excursion that peaks at 3 m below the Cleveland—Bedford contact within the black shale interval at the TR section (**Fig. 2.2b**).

Mo concentration in sedimentary rocks is a well-utilized geochemical proxy for recognizing ancient marine euxinia, as Mo is usually enriched in sediments deposited under sulfidic water columns (Tribovillard et al., 2006). The extent of Mo enrichment is dependent on the amount of dissolved Mo available in the water column, the total organic carbon content preserved, and the amount and persistence of free sulfide based on modern and ancient sedimentary studies (Tribovillard et al., 2006; Scott and Lyons, 2012). Sedimentary Mo concentrations greater than 20 ppm (of total rock mass) are generally considered intermittently euxinic, while concentrations over 60 ppm are predominantly or permanently euxinic (Scott & Lyons, 2012). Conversely, persistently

restricted euxinic basins often record low concentrations of Mo due to the near-quantitative drawdown of trace metals within their water mass (Algeo & Lyons, 2006). Following the $\delta^{13}C_{org}$ excursion at TR, sedimentary Mo behavior changes (**Fig. 2.2c**), beginning to fluctuate and reach the most highly enriched values (with a high median value of 106 ppm). Fluctuations in sedimentary Mo enrichment could imply either 1) variable volumetric extent and persistence of euxinia over depositional time; and/or 2) the competing local effects of euxinic drawdown of dissolved molybdenum versus marine circulation replenishment of dissolved metal inventories.

Variation in the strength or duration of euxinia is commonly used to explain fluctuations in Mo enrichments. However, this is inconsistent with biomarker evidence for abundant Chlorobi bacteria which flourished due to photic zone euxinia being sustained throughout the deposition of the upper Cleveland Shale (see sections 4.4 and 5.2). In light of this evidence, fluctuations in Mo enrichment at TR can best be interpreted as the replenishment of local dissolved metal inventories with metal-rich ocean waters rather than representing significant swings in redox conditions. This could have been achieved by a transgressive event, which would have increased the connectivity of the basin margin to the ocean. Mo/TOC values, which have been used as a proxy for ocean connectivity in partially restricted basins, have an average of 25 at the TR locality, implying a moderate connection to the open ocean (Algeo and Lyons, 2006). These values increase from the $\delta^{13}C_{org}$ excursion to a peak 2 m below the Cleveland—Bedford contact (**Fig. 2.8**); at this point, total sedimentary Mo concentration remains over 100 ppm for nearly a meter (**Fig. 2.2c**). Mo concentrations and Mo/TOC values then decline

towards the Bedford Shale, signifying a decrease in oceanic connectivity immediately approaching the contact. Consequently, the high enrichments of Mo in black shales throughout the TR section argue against a uniform global-scale drawdown of oceanic Mo inventories throughout the deposition of the Cleveland Shale (Algeo et al., 2007). We propose this combined carbon isotope, biomarker, and trace metal evidence constrains the onset and intensification of HC conditions at TR to within 3 m from the Cleveland—Bedford contact (**Fig. 2.2**).

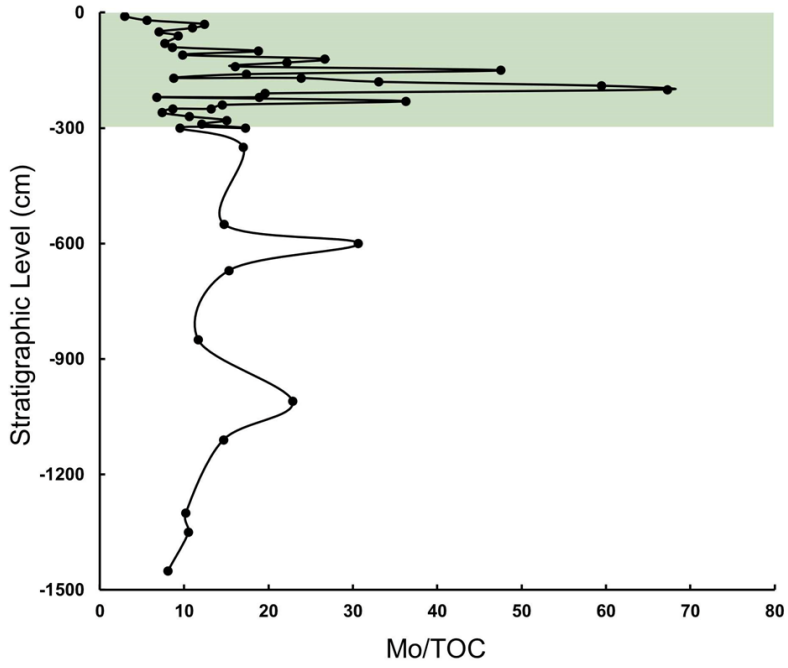

Figure 2.8: Crossplot of Mo/TOC for the Cleveland Shale at Tiedeman Road. Green shaded region is the proposed Hangenberg Crisis interval following the peak $\delta^{13}C_{org}$. 0 cm is the Cleveland—Bedford contact.

In contrast to the more complete TR section, there is no obvious organic carbon isotope excursion seen at the RB section with $\delta^{13}C_{org}$ values remaining close to a typical Paleozoic baseline of ca. -29‰ (**Fig. 2.3b**). It is likely that no excursion was captured here due to the thinner stratigraphic exposure of black shale at this locality. The $\delta^{13}C_{org}$ values for the Cleveland Shale at RB fall within the range of $\delta^{13}C_{org}$ values for the upper black shales deposited above the Cleveland Shale excursion level at TR, consistent with this interpretation. Furthermore, the RB results are comparable and complementary to those of Maynard (1981), who reported a 1‰ positive excursion relative to a -29‰ baseline near the top of the Cleveland Shale in a close-by locality in Richland, Ohio.

While a HC-linked transgressive event is captured in our dataset at TR, Mo inventories at the RB section appear to indicate increased basinal restriction resulting in less connection and exchange with open ocean waters. The RB section records a sudden drop from a single very high Mo value to much lower and consistent values for the uppermost black shale interval (**Fig. 2.3c**). This is despite appreciable TOC contents as well as the ubiquitous occurrence of abundant Chlorobi biomarkers (**Fig. 2.3g**). Given these constraints for persistent PZE baseline paleo environmental conditions at the RB section, the most parsimonious explanation for low Mo concentration in such a euxinic depositional setting is near quantitative drawdown of Mo in a restricted basin outcompeting dissolved metal replenishment. The depleted metal inventories at RB likely indicate suppressed oceanic recharge during the uppermost Cleveland Shale deposition at this locality. Nutrients supporting the RB ecosystem may have been more reliant on riverine inputs as Rimmer et al. (2004) have proposed for a Cleveland Shale locality in

modern day Kentucky; however, there is little biomarker evidence for local increases in terrestrial-based OM before a decline in HI immediately before the Cleveland—Bedford contact (**Fig. 2.4**). Since the RB section records only the final few meters of the Cleveland Shale, the biomarker and trace metal constraints together with a lack of a $\delta^{13}C_{org}$ excursion, indicate the RB section strata does not capture the onset of the HC paleoenvironmental conditions.

Combined chemostratigraphic profiles of $\delta^{13}C_{org}$, abundant Chlorobi biomarkers, and trace metal inventories in the black shales comprising the uppermost Cleveland shale are overall consistent with key characteristics of HC paleoenvironmental conditions reported elsewhere. Furthermore, Mo and Mo/TOC values at TR eventually show a similar drop (to Mo = 12-26 ppm; n = 5, **Fig. 2.2c**) as the RB section directly before the Cleveland—Bedford contact. We posit that the trace metal data for the uppermost Cleveland Shale at RB and TR, as well as the glacially-rafted dropstones in other time-equivalent North American localities (Brezinski et al., 2010), is consistent with a return to glacially-driven regression leading into the Bedford Shale. This is similar to the scenario proposed following the termination of Hangenberg black shale deposition in Europe (Kaiser et al., 2015).

5.2. Source biota and paleoenvironmental information from lipid biomarkers

Lipid biomarker analysis reveals important information about the Cleveland Shale depositional environment, modes of primary production and the stability of the microbial community structure leading up to and through the Hangenberg Crisis. TOC content is

consistently high throughout our dataset (**Fig. 2.2a and 2.3a**), though not as enriched as some previously reported Cleveland Shale samples (Rimmer et al., 2004). High TOC content can be associated with either elevated productivity and/or exceptional preservation of produced organic matter, but these factors are not mutually exclusive—productive settings can dynamically sustain low oxygen conditions that facilitate sedimentary organic matter preservation. Discernible terrestrial organic matter inputs only begin to increase towards the Cleveland—Bedford contact and stratigraphically higher and can readily be distinguished by molecular patterns in saturated hydrocarbon profiles (increased contribution from long chain *n*-alkanes combined with a prominent odd-over-even carbon number preference; see **Fig. 2.4**) and in Rock-Eval pyrolysis parameters (drop in HI to 150 mg/g TOC or less; see **Fig. 2.4 and Table 2.1**). We note that the apparent increase in terrestrial plant inputs to sedimentary organic matter coincides with a concomitant decrease in bulk TOC content, which suggests either a reliance of this microbial community on marine-derived nutrients and/or a change in organic matter preservation potential.

5.2.1. Hopanes and steranes

Throughout the black shale package found in both sections, the hopane/sterane (H/S) ratio is consistently low (median value of 0.35 for combined localities). This indicates an abundance of eukaryotic source organismal inputs and a strong contribution of marine algae to the overall primary production throughout deposition. These data are comparable to H/S ratios compiled from the Hangenberg black shale in the Holy Cross

Mountains, Poland (Marynowski et al., 2012), as well as sustained low H/S ratios reported for other Late Devonian extinctions, notably the previous Frasnian-Famennian transition (Haddad et al., 2016). This contrasts with the characteristics other of Paleozoic mass-extinction events and their aftermaths, such as at the end-Permian and end-Ordovician, for which there are reports of elevated bacterial contributions to sedimentary OM as a response to extinction and nutrient stress (Cao et al., 2009; Rohrssen et al., 2013; with the caveat that productive marine settings generally show a lower H/S than for contemporaneous oligotrophic settings, as expected). H/S ratios increase at and beyond the Cleveland—Bedford contact (range = 0.7-3.3), indicating increasing bacterial source inputs as glaciation and regression led to a shallower and more oxic paleoenvironment, also associated with increasing terrestrial plant/soil matter input.

Abundance patterns between different sterane carbon numbers and structures can be characteristic of particular algal clades even though these biomarkers are not source-specific compounds. For instance, C_{27} compounds are often produced as the major steroids by red algae, such as rhodophytes, while C_{28} being common in more-derived red algal clades which radiated from the Mesozoic Era and younger, such as coccolithophores and diatoms. In contrast, C_{29} steroids are produced by most green algal clades and terrestrial plants, although some prasinophyte algae exhibit a C_{28} steroid dominance (Kodner et al., 2008). A strong C_{29} sterane (stigmastane) carbon number predominance is consistently found in our samples throughout both sections, indicative of a predominance of green algal clades among the eukaryotic source organisms, similar to Frasnian-Famennian biomarker records from New York (Haddad et al., 2016) and most

early Paleozoic marine settings (Schwark and Empt, 2006; Rohrssen et al., 2013). The C_{30} steranes found are predominantly in the form of 24-*n*-propylcholestane isomers and are detectable throughout the entirety of the Cleveland Shale (**Fig. 2.5**). 24-*n*-propylcholestane is most likely derived from pelagophyte algae (Moldowan et al., 1990) in Devonian rocks, which are an exclusively marine class of microalgae and consistent with a predominantly autochthonous source input of marine organic matter for the black shales. The 24-*n*-propylcholestane proportions are highest immediately following the $\delta^{13}C_{org}$ excursion in organic-rich black shales deposited during the HC interval at TR (max = 7% total $C_{27\text{-}30}$ steranes).

The ratio of C_{28}/C_{29} steranes is low for all Cleveland Shale samples (TR median = 0.3; RB median = 0.22; overall range = 0.14-0.4, **Fig. 2.2e, 2.3e, and 2.5**)**;** values of 0.2-0.4 are found for many early Paleozoic sedimentary rocks and oils (Grantham and Wakefield, 1988; Schwark and Empt, 2006; Haddad et al., 2016). Schwark and Empt (2006) reported a similar range for their Ohio Shale strata (mostly in the 0.3 to 0.45 range) but with a subsequent transition to higher C_{28}/C_{29} ratios (> 0.55) for other Appalachian Basin shales during the Late Devonian—Early Carboniferous transition. These higher C_{28}/C_{29} sterane ratios come from the Bedford and Sunbury Shales, which stratigraphically overlie the Cleveland Shale studied here. Schwark and Empt (2006) suggested that the increased proportion of C_{28} steranes in these Appalachian Basin shales represents a fundamental transition in algal ecology, favoring prasinophytes, perhaps triggered by repeated Late Devonian biocrises or climactic perturbations. Our constantly low values of the C_{28}/C_{29} sterane ratio in shales from both the TR and RB sections

through the latest Devonian interval suggests that the algal ecological transition suggested by Schwark and Empt (2006) may have been significantly delayed or less prominent in paleotropical latitudes until the early Carboniferous or younger. Indeed, previously reported sterane carbon number patterns for Laurentian paleotropical epeiric seas in the Late Devonian show a similarly low C_{28}/C_{29} ratio to ours for Frasnian-Famennian aged black shales from the Appalachian Basin (mean = 0.3; Haddad et al., 2016).

5.2.2. Methylhopanes

The 3β-methylhopane index for both TR and RB sections mostly fall around the 1-3% Phanerozoic marine average (Peters et al., 2005; Cao et al., 2009), but occasionally just exceed 4.0%. Median values are higher than Appalachian Basin black shales from the Frasnian-Famennian interval (avg. 1%; Haddad et al., 2016). Elevated 3β-MeHI values can be characteristic of increased methane cycling in the local paleoenvironment (Rohrssen et al., 2013). The synthesis of 3β-methylbacteriohopanepolyols, from which 3β-methylhopanes are derived, has commonly been linked to aerobic methanotrophic proteobacteria when these are biomarkers are anomalously abundant in rocks and oils (Peters et al., 2005; Rohrssen et al., 2013) although these compounds can be synthesized by diverse bacterial groups (Welander and Summons, 2012). However, the highest values of 3β-MeHI in the Cleveland Shale at TR and RB (max 4.1 % and 4.3%) do not reach anywhere near the elevated 3β-methylhopane index values as previously found for numerous Late Ordovician-Silurian rocks from Laurentia (>10%, Rohrssen et al., 2013)

and sporadically up to 13% for end-Triassic to early Jurassic strata (Kasprak et al., 2015). While it should be noted that the relative changes in 3β-MeHI values in the Cleveland black shale can appear quite dramatic (such as a doubling effect from 2% to 4% found near the top of the TR section), these absolute values are all low in magnitude, close to the typical Phanerozoic marine average range (1-3%), and likely do not signify major changes in the microbial community.

Previously, 2α-methylhopanes have been used as a marker for oxygenic photosynthesis via cyanobacterial production; however, it is now apparent that a wide range of bacterial groups are capable of 2α-methylhopanoid biosynthesis (Rashby et al., 2007; Welander et al., 2010; Ricci et al., 2014). Regardless of the nature of the source bacteria, elevated 2α-methylhopane index values have been noted for other ocean anoxic events and have been linked to anoxia and/or nitrate limitation in the aftermath of anoxia (Kuypers et al., 2004; Cao et al., 2009; Ricci et al, 2014; Kasprak et al., 2015). Neither the TR nor the RB section, however, shows elevated abundance of, nor noteworthy variation within, 2α-methylhopanes across the interval of sampled strata. The 2α-MeHI is similar to the generally low values (<5%) reported previously for Late Devonian (Frasnian/Fammenian transition) black shales from both high and low paleolatitudes (Haddad et al., 2016). This contrasts with other periods of prolonged PZE, such as observed for the End-Triassic, where high relative abundances of 2α-methylhopanes co-occur with isorenieratane (Kasprak et al., 2015), as well as the exceptionally high 2α-MeHI values (10-33%) observed for the Early Triassic marine aftermath of the end-Permian mass extinction in South China (Cao et al., 2009).

5.2.3. Chlorobi carotenoid markers

Green sulfur bacteria, or Chlorobi, are anoxygenic phototrophs that can utilize sulfide as an electron donor (Summons and Powell, 1986). Chlorobi-derived carotenoids (isorenieratane, paleorenieratane, and aryl isoprenoid fragments) are ubiquitous in the Cleveland Shale and signify at least episodic PZE conditions in the water column. These organisms likely inhabited the lower portion of the photic zone and isorenieratane, in particular, is derived from the brown strain of green sulfur bacteria that can live in low light settings up to 100 m water depth (French et al., 2015 and references therein). Chlorobi could co-exist with eukaryotic algae as photosynthetic primary producers by zonation at different surface water depths, with algae preferentially inhabiting the shallower depths within the surface mixed layer, where dissolved oxygen is present. High absolute abundances of aromatic Chlorobi biomarker compounds were observed for both TR and RB sections within the HC interval (see **Fig. 2.2g and 2.3g**). These findings are consistent with similar biomarker features in Hangenberg black shales from the Holy Cross Mountains in Poland (Marynowski and Filipiak, 2007; Marynowski et al., 2012) although only low Chlorobi biomarker abundances tied to variable paleoredox conditions were reported for Frasnian-Famennian black shales from New York sections of the Appalachian Basin (Haddad et al., 2016).

To further assess whether PZE was persistent or intermittent, we employed the aryl isoprenoid ratio (AIR), which relates the proportion of short-chain (C_{13}–C_{17}) to intermediate-chain (C_{18}–C_{22}) aryl isoprenoids to determine the extent of aerobic degradation undergone by these compounds (i.e. Schwark and Frimmel, 2004; Spaak et

al., 2018). Low AIR values (<1) are proposed to highlight enhanced molecular preservation in a highly reducing environment such that photic zone anoxia is considered to be persistent, while higher values of AIR (> 1) indicate settings where longer chain aryl isoprenoids have been increasingly degraded and thus represent periods of only episodic photic zone anoxia. Nearly all AIR values for the Cleveland Shale are less than 1.0, which corresponds with aryl isoprenoid generation and preservation in a marine system sustaining photic zone euxinia or anoxia persistently (**Fig. 2.6**). An additional feature revealed by **Fig. 2.6** is the distinct separation between TR and RB when comparing pristane/phytane ratios (Pr/Ph) to AIR. The pristane/phytane (Pr/Ph) ratio is an established and commonly used molecular parameter for evaluating paleoredox conditions (Peters et al., 2005). Although Pr/Ph values for both TR and RB remain in an ambiguous zone due to their unexceptional moderate values (Pr/Ph = 1.0 to 3.0), samples from each locality cluster together (**Fig. 2.6**). RB samples generally show overall higher Pr/Ph ratios (median = 1.92) than TR (median = 1.36) despite the overlapping AIR values between these localities. An important counter-argument to persistent PZE conditions, as apparently indicated from AIR values, comes from the scattered occurrence of small burrows that provide physical evidence of sporadic ventilation of the bottom waters. This suggests that certain geochemical proxies such as AIR may be biased to record strongly reducing conditions, due to the suitability of those reducing conditions for preserving geochemical signatures (see section 5.4).

C_{40} carotenoid distributions in the Cleveland Shale contain a high abundance of the mysterious biomarker paleorenieratane, aptly named for its common temporal

occurrence in the Paleozoic. Paleorenieratane has no known equivalent modern biological precursor but is commonly prescribed a Chlorobi affinity based on its chemical structure, frequent co-occurrence with, and similar isotopically enriched $\delta^{13}C$ values as the Chlorobi-produced carotenoid, isorenieratane (French et al., 2015). Recent studies have compared relative abundances of paleo- and isorenieratane to understand paleoenvironments in regard to variables such as light intensity and salinity (French et al., 2015; Spaak et al., 2018). Spaak et al. (2018) observed a connection of C_{40} carotenoids with the degree of basinal restriction in the Devonian Canning Basin and conducted a short literature review. They noted that paleorenieratane/ isorenieratane (P/I) ratios > 1 commonly co-occur with AIR values > 1 and are perhaps indicative of episodic euxinia in less restricted settings. Our data do not fully support that of Spaak et al. (2018), but there are some similarities. The AIR at both Tiedeman Road (TR) and Rocky Branch (RB) is almost always < 1, however, the P/I ratio is variable between and within the two localities. At TR, the P/I switches from consistently < 1 (median = 0.89; isorenieratane dominated) for the majority of the section to P/I > 1 within the HC interval (median = 1.21; paleorenieratane dominated; **Fig. 2.9**). Potentially, this switch could indicate a decrease in local basin restriction at TR, which would be coincident with the increased oceanic connection proposed above from Mo concentrations. At RB, paleo- and isorenieratane are almost nearly equivalent (median P/I = 1.05) with a slight tendency towards paleorenieratane predominance (**Fig. 2.9**). However, low Mo concentrations at RB suggest a restricted basin, which would contrast with elevated isorenieratane

indicating restriction (Spaak et al., 2018). Furthermore, paleo- and isorenieratane co-occur in each sample in our dataset, though they do not in the Canning Basin.

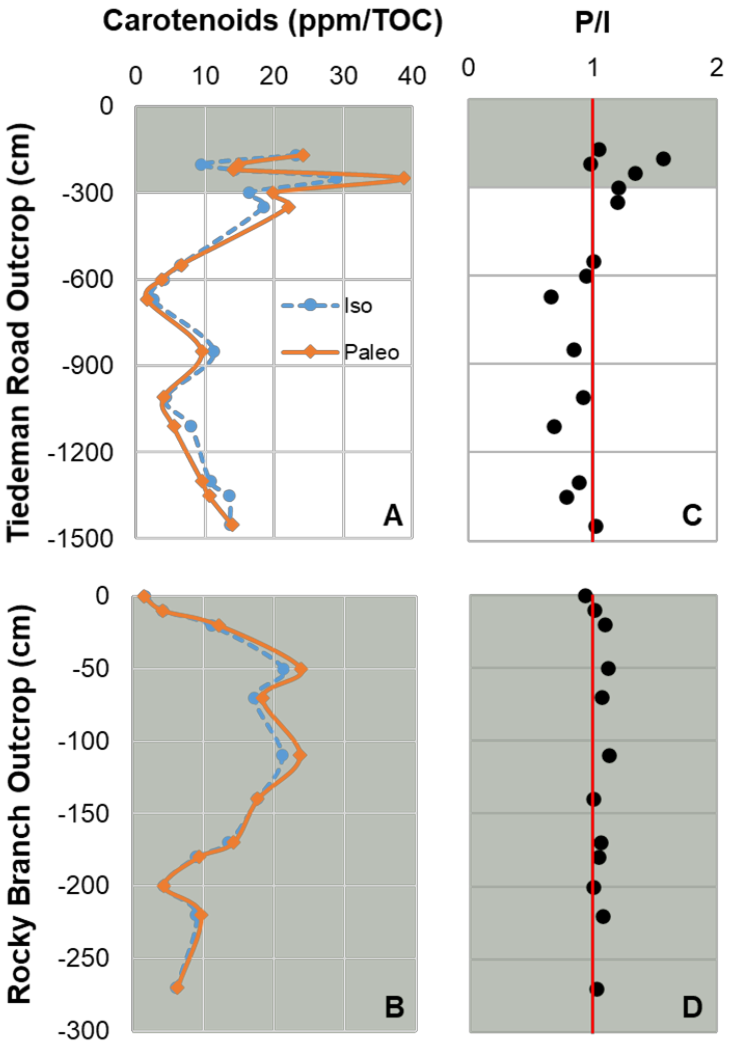

Figure 2.9: Carotenoid concentration profiles and ratios from TR and RB. Green shaded region indicates our proposed Hangenberg Crisis (HC) interval. A) and B) Concentrations (ppm/TOC) of isorenieratane (dashed line, blue circles) and paleorenieratane (solid line, orange diamonds) from TR and RB, respectively. C) Ratio of paleorenieratane to isorenieratane (P/I) for the TR section. There is a switch from isorenieratane dominated (P/I < 1) to paleorenieratane dominated (P/I > 1) at our proposed onset of the HC. D) Ratio of paleorenieratane to isorenieratane (P/I) for the RB section. Paleorenieratane and isorenieratane remain nearly equivalent (P/I ~ 1) for the entirety of the RB section, with a slight paleorenieratane predominance.

5.2.4. Major characteristics of biomarker assemblages

Overall, the biomarker assemblages found within the sampled strata of the Cleveland Shale reveal a stable and algal-rich late Devonian primary producer community thriving in a locally redox-stratified epicontinental shelf setting. The sedimentary organic matter in the black shales is derived predominantly from autochthonous sources from marine microorganisms. While there is some expected variation within some bacterial biomarker abundance parameters (i.e. Chlorobi and 3β-methylhopane producers) that occurs with the onset of HC conditions, the major biomarker assemblage features (low H/S ratios and invariant sterane patterns with a strong green algal source) are remarkably constant throughout the deposition of the black shales (**Fig. 2.2, 2.3, and 2.4**). These combined observations suggest a high tolerance of the microbial communities for low oxygen and chemically-stratified redox environmental conditions that prevailed in productive marginal settings during the Late Devonian (Tuite & Macko, 2013; Haddad et al., 2016). High productivity of the planktonic microbial community dynamically maintained OMZs at water depths within and below the photic zone through organic matter remineralization of settling biomass. Furthermore, any significant terrestrial inputs to organic matter only occur just immediately before the Cleveland—Bedford contact. This is stratigraphically situated above the main black shale package and coincides with an organic and lithofacies facies change as shown by a decrease in TOC content and oil-generating potential, coarser mudstone/siltstones, and a transition into a shallower and more oxic paleoenvironment.

5.3. Nitrogen isotopic excursion

Nitrogen cycling in Late Devonian epeiric seaways encompasses contributions from organisms utilizing different nitrogen species, including nitrate and recycled ammonium (Perkins et al., 2008; Rooney et al., 2015). Since biomarker assemblages remain relatively constant throughout the sampled intervals at both localities, the secular changes in $\delta^{15}N_{total}$ at the TR section likely represent changes in the stable isotopic composition of dissolved nitrate and other fixed nitrogen species rather than significant variations in source biota. We suggest the positive $\delta^{15}N_{total}$ excursion at TR was predominantly driven by increased denitrification rates during a transgressive event (Brezinski et al., 2010; Tuite & Macko, 2013). This transgressive event would replenish metal and nutrient levels and provide a ^{15}N-enriched bioavailable nitrogen source (^{15}N-enriched oceanic NO_3^-) for primary producers in the Appalachian epeiric seaways. This influx of nutrients could boost primary productivity and ultimately drive an expansion of the marine OMZ (as corroborated by an increase in TOC contents and enrichments in the abundance of Chlorobi biomarkers; **Fig. 2.2 and 2.3**). A greater volume of OMZ water column would have facilitated denitrification rates to exceed the rates of nitrogen fixation, driving the source nitrate progressively ^{15}N-enriched over time through partial consumption. Previous explanations for perturbed N cycles during anoxic or extinction events include enhanced recycling of ammonium; however, this should produce a negative excursion in $\delta^{15}N_{total}$ (Higgins et al., 2012; Kasprak et al., 2015), opposite to the trend that we observe. Increased weathering rates associated with the Late Devonian expansion of vascular plants (Algeo et al., 1995) could provide an additional flux of

nitrogen species and other nutrients, though we have no evidence for increased terrestrial source input to OM at our localities for this stratigraphic interval from detailed biomarker investigation (**Fig. 2.4**) until the very last centimeters of the black shale package that transitions into coarser grey shales and siltstones.

The positive $\delta^{15}N_{total}$ excursion at TR is consistent with a recent study by Rooney et al. (2015), who compared $\delta^{15}N$ between bulk sediment and *Tasminites* palynomorphs (a prasinophyte) in Cleveland Shale sections from Kentucky. These authors report a parallel increase in $\delta^{15}N$ values from both bulk sediment and *Tasminites* in the upper Cleveland Shale section, which they interpret could signify a shift in nutrient dynamics in the depositional basin. The onset of the $\delta^{15}N_{total}$ excursion at TR stratigraphically aligns with the termination of the $\delta^{13}C_{org}$ excursion, suggesting that the carbon cycle perturbation may have influenced nitrogen cycling as well. The cessation of the $\delta^{15}N_{total}$ excursion could signal glacial regression directly leading into the Cleveland—Bedford contact, which would increase basin restriction and cut off the connection to the open ocean. The positive nitrogen isotope excursion is potentially a useful correlation tool for identifying an intensification of sea level rise and reducing paleoenvironmental conditions in black shale successions with good stratigraphic coverage deposited around the Devonian-Carboniferous boundary in contemporaneous productive margins.

5.4. Constraints from bioturbation indicators

While biomarker and trace metal inventories make a strong and consistent argument for largely persistent photic zone euxinia conditions during deposition,

sedimentary fabrics preserved in the Cleveland Shale help describe a more nuanced paleoredox history and thus offer valuable insight (**Fig. 2.7**). Most bioturbation in the Cleveland Shale occurs as small burrows, on average a few millimeters diameter, and as disruptions in the depositional laminae. An exception to this rule are rare layers of well-preserved burrows at the TR section that measure over a centimeter in vertical depth. Overall, the discernible trace fossil signals in some horizons suggest that bioturbation and seafloor oxygenation occurred episodically throughout this succession. These episodes are perhaps linked to climactic cycling as proposed in Jaminski et al. (1998), although small-scale burrowing found here does not seem to follow a cyclical pattern. Burrowed horizons highlight that geochemical proxies often fail to capture these rapid and sporadic redox fluctuations in ancient black shales at times when marine chemical stratification weakened. Recognition of bioturbation allows a more balanced evaluation of the dynamics of redox change, nutrient replenishment, and the continuity of macrofaunal habitability in paleoenvironments. This is particularly important when chemostratigraphic proxies such as Mo enrichments and the AIR biomarker ratio suggest a pervasively redox-stratified basin sustaining shallow euxinic conditions.

6. Conclusions

We propose from a multi-proxy geochemical investigation that the uppermost Cleveland Shale in Ohio is an equivalent unit to the Hangenberg black shale found in Europe and the black shales were deposited in a productive and redox-stratified epicontinental shelf setting. A stable microbial community provided the primary biomass

necessary to support heterotrophy and dynamically maintained shallow euxinic depositional conditions locally, even prior to the intensification of Hangenberg Crisis (HC) conditions. The synchronous ~2‰ positive excursions in $\delta^{13}C_{org}$ and $\delta^{13}C_{carb}$ near the base of the Hangenberg black shale in Europe are mirrored by a similar magnitude positive $\delta^{13}C_{org}$ excursion found here below the Cleveland—Bedford contact at our most complete (TR) section. The dual and sequential expression of positive C and N isotope excursions at TR could provide a useful tool to identify the onset of HC in other geographical marine localities on productive continental margins near the Devonian-Carboniferous boundary. Enriched sedimentary Mo concentrations were maintained under pervasive euxinic baseline conditions due to redox-stratification but with the highest values occurring after the onset of the HC, consistent with a marine transgression and influx of nutrients. Similar paleoenvironmental conditions have been proposed for accumulation of black shales during the HC globally (Kaiser et al., 2015; Carmichael et al., 2015). Decreasing TOC contents, lower hydrogen indices, and muted Mo enrichments are all associated with the coarser clastic rocks deposited above the HC black shales, and, with glacial dropstones from other localities, indicate a shift back to glacial regression leading into the Bedford Shale, consistent with sea level trends proposed for equivalent units in Europe.

Throughout the black shale succession in the upper Cleveland Shale, there was apparently no major shift in the microbial community structure as inferred from the major characteristics of the lipid biomarker assemblages. We can recognize key biomarker characteristics of Late Devonian black shales that are appreciably different from those of

organic-rich rocks associated with deposition during other oceanic anoxic events of the Phanerozoic Eon. A low average value of hopane/sterane (ca. 0.35 for median value) and a strong organic matter source contribution from marine green algae is a constant feature of these and other Late Devonian black shales, despite global biocrises affecting eukaryotic macrofaunal clades (Sallan and Coates, 2010). Our evidence confirms that microbial communities survive, even thrive in some shelf settings, and sustain primary productivity during extinction events. Indeed, locally redox-stratified marine conditions with anoxic/euxinic zones extending into the lower photic zone could not be sustained without this microbial biomass since it is the remineralization and degradation of primary biomass that consumes dissolved oxygen and sulfate in the water column. The low C_{28}/C_{29} sterane ratios throughout our dataset indicate that any Paleozoic ecological transition to C_{28} producing algae is delayed in tropical paleolatitudes until after the HC. The inferred stability of the main microbial communities, combined with a positive $\delta^{15}N_{total}$ excursion at TR, likely signifies increasing rates of water column denitrification associated with a local expansion of the marine OMZ during the intensification of HC conditions.

Important insights were gained from ichnofabric evaluations that place important constraints on the temporal continuity of euxinic conditions. Shallow burrows found throughout the Cleveland Shale highlight the limitations of some geochemical redox approaches for recognizing short-lived and sporadic redox changes that deviate from anoxic/euxinic baseline conditions. Brief oxygenation pulses supported short lived bioturbation events occurring even within a strongly and predominantly redox-stratified

euxinic basin—albeit with low-oxygen stress more pronounced during the HC crisis interval—and underscore the necessity of integrating multiple independent redox proxies for a more complete paleoenvironmental reconstruction.

Sample	Outcrop Level (cm)	HI	Tmax
RB2B	0	150	438
RB8B	-50	435	432
RB13T	-170	549	435
RB15T	-270	658	432
TR20B2	0	136	432
TR6B	-170	618	431
TR5B	-350	460	433
TR14B1	-670	628	428
TR9B	-1450	609	431

Table 2.1: Rock-Eval Pyrolysis parameters measured for a subset of sedimentary rocks for Rocky Branch (RB) and Tiedeman Road (TR) localities. Tmax data are indicative of early oil window maturities and HI data indicate primarily marine sources of organic matter. The lower HI values for RB2B and TR20B2 are due to a more oxic and less organic-rich depositional facies with higher terrestrial organic input than the marine black shales.

Sample	Outcrop Level (cm)	TOC (wt%)	Ichnofabric Index	Hopane/ Sterane	2α-MeHI (%)	3β-MeHI (%)	Chlorobi Biomarkers (ppm/TOC)	Mo (ppm/rock)	U (ppm/rock)	$\delta^{15}N_{Total}$ ‰	$\delta^{13}C_{org}$ ‰
RB1B	40	0.13	5	3.30	1.70	4.72	1	15	2	1.95	n.d.
RB17B	10	0.18	4	2.76	0.85	3.36	n.d.	n.d.	n.d.	0.43	-26.5
RB2B	0	1.37	2.2	1.05	1.31	5.53	27	17	5	1.06	-26.4
RB5B	-10	1.78	n.d.	0.86	1.02	4.29	35	15	5	1.49	-27.1
RB21B	-20	3.29	1.8	0.47	0.87	2.60	96	15	5	1.74	-28.2
RB8B	-50	4.07	2	0.44	1.39	3.51	166	19	5	2.18	-28.5
RB9B	-70	3.18	2	0.47	1.37	3.62	118	19	5	2.00	-28.3
RB11B	-110	4.06	2.2	0.44	1.01	2.83	155	20	5	2.36	-28.7
RB23B	-140	4.53	1.6	0.34	0.74	2.18	130	15	5	2.05	-28.6
RB13T	-170	4.14	2	0.45	1.16	2.74	110	15	7	1.89	-28.6
RB24B	-180	4.22	1.2	0.37	0.54	2.16	82	14	7	1.69	-28.6
RB25B	-200	4.01	1	0.34	0.85	2.13	55	20	12	1.74	-28.6
RB14B	-220	4.05	2	0.48	1.05	3.19	81	17	8.6	1.20	-28.6
RB15T	-270	7.54	1	0.29	1.27	3.39	62	144	21	2.41	-29.3

Table 2.2: Data from Rocky Branch locality. Including: total organic carbon (TOC) as wt%; Ichnofabric index, C_{27-35} Hopane/ C_{27-30} Sterane ratio; 2α-MeHI (%) = 2α-Methylhopane Index and 3β-MeHI (%) = 3β-Methylhopane Index: 3β- and 2α-methylhopane indices were calculated from the percentage abundance of the C_{31} methylhopane relative to sum of C_{31} methylhopane and C_{30} αβ-hopane; overall abundance of Chlorobi biomarkers including isorenieratane, paleorenieratane, and their aryl isoprenoid fragments (C_{13}-C_{24}) in ppm/TOC; Molybdenum (Mo) concentration in ppm/rock; Uranium (U) concentration in ppm/rock; $\delta^{15}N_{total}$ ‰ (vs. air); and $\delta^{13}C_{org}$ ‰ (vs. VPDB). RB2B indicates transition to Bedford Shale.

Sample	Outcrop Level (cm)	TOC (wt%)	Ichnofabric Index	Hopane/ Sterane	2α-MeHI (%)	3β-MeHI (%)	Chlorobi Biomarkers (ppm/TOC)	Mo (ppm/rock)	U (ppm/rock)	$\delta^{15}N_{Total}$ ‰	$\delta^{13}C_{org}$ ‰
TR17B	25	0.72	2.5	0.74	1.38	3.20	67	26	11.3	1.3	-27.0
TR20B2	0	0.69	4.2	0.79	1.02	3.64	n.d.	24	10.1	n.d.	n.d.
TR6B	-170	9.5	1	0.26	0.83	3.98	195	83	11.8	2.8	-29.3
TR7B2	-200	3.37	1.6	0.34	0.93	3.71	144	n.d.	14.1	n.d.	n.d.
TR7B	-205	n.d.	n.d.	n.d.	n.d.	n.d.	n.d.	47	13.7	2.7	-28.7
TR1B	-220	9.2	1.6	0.25	0.81	3.02	104	174	12.7	3.5	-29.2
TR8B	-250	3.22	1.2	0.30	1.21	3.61	252	43	14.7	2.2	-28.6
TR16B	-300	4.63	1	0.29	1.06	2.40	141	80	15.4	2.3	-28.2
TR5B	-350	7.12	1.2	0.25	1.30	4.16	134	121	13.6	2.8	-28.7
TR4B	-550	7.67	n.d.	0.34	0.65	2.09	55	113	12.1	1.8	-29.3
TR15B	-600	4.09	1	0.33	0.41	1.48	38	125	28.5	1.7	-29.0
TR14B1	-670	7.5	1.5	0.25	0.42	1.68	33	115	9.2	2.0	-29.4
TR2B	-850	4.72	1.8	0.31	0.91	2.68	71	55	9.1	1.4	-28.8
TR13B	-1010	4.28	1.6	0.35	0.61	1.58	45	98	9.8	2.0	-28.9
TR12B	-1110	4.46	2	0.32	0.71	2.34	41	65	11.5	1.4	-28.8
TR11B	-1300	4.24	1.2	0.39	0.82	3.95	81	43	15.6	1.5	-29.0
TR10B	-1350	3.2	2	0.28	0.91	3.33	80	34	8.7	1.7	-28.5
TR9B	-1450	4.99	2	0.43	0.75	3.69	103	40	9.7	1.1	-28.7

Table 2.3: Data from Tiedeman Road locality. Including: total organic carbon (TOC) wt%; Ichnofabric index, C_{27-35} Hopane/C_{27-30} Sterane ratio; 2α-MeHI (%) = 2α-Methylhopane Index and 3β-MeHI (%) = 3β-Methylhopane Index: 3β- and 2α-methylhopane indices were calculated from the percentage abundance of the C_{31} methylhopane relative to sum of C_{31} methylhopane and C_{30} αβ-hopane; overall abundance of Chlorobi biomarkers including isorenieratane, paleorenieratane, and their aryl isoprenoid fragments (C_{13}-C_{24}) in ppm/TOC; Molybdenum (Mo) concentration in ppm/rock; Uranium (U) concentration in ppm/rock; $\delta^{15}N_{total}$ ‰ (vs. air); and $\delta^{13}C_{org}$ ‰ (vs. VPDB). TR20B2 indicates transition to Bedford Formation.

Sample	Outcrop Level (cm)	TOC (wt%)	Mo (ppm/rock)	U (ppm/rock)	$\delta^{15}N_{total}$	$\delta^{13}C_{org}$
TRChip1	0	n.d.	20	3	0.6	n.d.
TRChip2	-10	4.0	12	7	2.0	-28.2
TRChip3	-20	3.5	19	6	2.2	-25.3
TRChip4	-30	11.2	138	10	1.9	-29.3
TRChip5	-40	9.4	103	9	2.4	-29.2
TRChip6	-50	7.7	54	9	3.4	-29.2
TRChip7	-60	5.2	48	10	3.1	-28.8
TRChip8	-70	n.d.	18	11	2.8	-28.4
TRChip9	-80	3.0	23	11	2.7	-28.5
TRChip10	-90	4.4	38	10	2.8	-29.2
TRChip11	-100	5.6	106	12	3.2	-29.0
TRChip12	-110	5.5	54	14	3.1	-29.0
TRChip13	-120	5.9	158	14	3.3	-28.9
TRChip14	-130	8.0	178	13	3.4	-29.0
TRChip15	-140	8.5	136	15	3.7	-29.1
TRChip16	-150	5.0	238	15	3.4	-28.9
TRChip17	-160	7.1	123	13	3.4	-29.0
TRChip18	-170	6.0	144	14	3.2	-28.9
TRChip19	-180	5.4	179	12	3.4	-28.8
TRChip20	-190	9.9	586	29	3.8	-29.2
TRChip21	-200	10	673	31	3.6	-29.1
TRChip22	-210	7.3	143	14	3.1	-29.0
TRChip23	-220	9.1	61	9	2.9	-29.1
TRChip24	-230	3.5	127	12	2.7	-28.4
TRChip25	-240	3.0	44	9	2.3	-28.6
TRChip26	-250	3.8	33	10	2.5	-28.7
TRChip27	-260	7.5	55	12	3.1	-29.2
TRChip28	-270	10.1	107	16	3.2	-29.3
TRChip29	-280	3.5	53	11	2.5	-28.3
TRChip30	-290	2.7	33	9	2.3	-28.2
TRChip31	-300	2.5	24	10	2.1	-28.0

Table 2.4: Additional data from Tiedeman Road locality. Including: total organic carbon (TOC) wt%; Molybdenum (Mo) concentration in ppm/rock; Uranium (U) concentration in ppm/rock; $\delta^{15}N_{total}$ ‰ (vs. air); and $\delta^{13}C_{org}$ ‰ (vs. VPDB).

References

Algeo, T. J., Berner, R. A., Maynard, J. B., & Scheckler, S. E. (1995). Late Devonian oceanic anoxic events and biotic crises:"rooted" in the evolution of vascular land plants. GSA Today, 5(3), 45–66.

Algeo, T. J., & Lyons, T. W. (2006). Mo–total organic carbon covariation in modern anoxic marine environments: Implications for analysis of paleoredox and paleohydrographic conditions. Paleoceanography, 21(1).

Algeo, T. J., Lyons, T. W., Blakey, R. C., & Over, D. J. (2007). Hydrographic conditions of the Devono–Carboniferous North American Seaway inferred from sedimentary Mo–TOC relationships. Palaeogeography, Palaeoclimatology, Palaeoecology, 256(3), 204–230.

Baird, G. C., Over, D. J., and Hannibal, J. T. (2013). Updates concerning end-Devonian bio- sequence- and event-stratigraphy, northwest Pennsylvania and northeastern Ohio regions. Geological Society of America Abstracts with Programs, 45, 53.

Boyer, D. L., & Droser, M. L. (2009). Palaeoecological patterns within the dysaerobic biofacies: Examples from Devonian black shales of New York state. Palaeogeography, Palaeoclimatology, Palaeoecology, 276(1), 206–216.

Brezinski, D. K., Cecil, C. B., & Skema, V. W. (2010). Late Devonian glacigenic and associated facies from the central Appalachian Basin, eastern United States. Geological Society of America Bulletin, 122(1–2), 265–281.

Cao, C., Love, G. D., Hays, L. E., Wang, W., Shen, S., & Summons, R. E. (2009). Biogeochemical evidence for euxinic oceans and ecological disturbance presaging the end-Permian mass extinction event. Earth and Planetary Science Letters, 281(3), 188–201.

Caplan, M. L., & Bustin, R. M. (1999). Devonian–Carboniferous Hangenberg mass extinction event, widespread organic-rich mudrock and anoxia: causes and consequences. Palaeogeography, Palaeoclimatology, Palaeoecology, 148(4), 187–207.

Carmichael, S. K., Waters, J. A., Batchelor, C. J., Coleman, D. M., Suttner, T. J., Kido, E., … Chadimová, L. (2015). Climate instability and tipping points in the Late Devonian: Detection of the Hangenberg Event in an open oceanic island arc in the Central Asian Orogenic Belt. Gondwana Research, 32, 213–231.

Corradini, C., Spalletta, C., Mossoni, A., Matyja, H., & Over, D. J. (2017). Conodonts across the Devonian/Carboniferous boundary: a review and implication for the

redefinition of the boundary and a proposal for an updated conodont zonation. Geological Magazine, 154(4), 888–902.

Droser, M. L., & Bottjer, D. J. (1986). A semiquantitative field classification of ichnofabric. Journal of Sedimentary Research, 56(4).

Droser, M. L., Bottjer, D. J., Sheehan, P. M., & McGhee, G. R. (2000). Decoupling of taxonomic and ecologic severity of Phanerozoic marine mass extinctions. Geology, 28(8), 675–678.

Eames, L.E. (1974). Palynology of the Berea Sandstone and Cuyahoga Group of northeastern Ohio (PhD Thesis). Michigan State University.

Ettensohn, F. R. (1985). Controls on development of Catskill Delta complex basin-facies. Geological Society of America Special Papers, 201, 65–78.

French, K. L., Rocher, D., Zumberge, J. E., & Summons, R. E. (2015). Assessing the distribution of sedimentary C40 carotenoids through time. Geobiology, 13(2), 139–151.

Grantham, P. J., & Wakefield, L. L. (1988). Variations in the sterane carbon number distributions of marine source rock derived crude oils through geological time. Organic Geochemistry, 12(1), 61–73.

Haddad, E. E., Tuite, M. L., Martinez, A. M., Williford, K., Boyer, D. L., Droser, M. L., & Love, G. D. (2016). Lipid biomarker stratigraphic records through the Late Devonian Frasnian/Famennian boundary: Comparison of high-and low-latitude epicontinental marine settings. Organic Geochemistry, 98, 38–53.

Hellstrom, L. W., & Babcock, L. E. (2000). High-resolution stratigraphy of the Ohio Shale (upper Devonian), central Ohio. Northeastern Geology and Environmental Sciences, 22(3), 202–226.

Higgins, M. B., Robinson, R. S., Husson, J. M., Carter, S. J., & Pearson, A. (2012). Dominant eukaryotic export production during ocean anoxic events reflects the importance of recycled NH_4+. Proceedings of the National Academy of Sciences, 109(7), 2269–2274.

House, M. R., Gordon, M., & Hlavin, W. J. (1986). Late Devonian ammonoids from Ohio and adjacent states. Journal of Paleontology, 60(1), 126–144.

Jaminski, J., Algeo, T. J., Maynard, J. B., & Hower, J. C. (1998). Climatic origin of dm-scale compositional cyclicity in the Cleveland Member of the Ohio Shale (Upper Devonian), Central Appalachian Basin, USA. Shales and Mudstones, 1, 217–242.

Kaiser, S. I. (2005). Mass extinctions, climatic and oceanographic changes at the Devonian/Carboniferous boundary (PhD Thesis). University of Bochum.

Kaiser, S. I., Aretz, M., & Becker, R. T. (2015). The global Hangenberg Crisis (Devonian–Carboniferous transition): review of a first-order mass extinction. Geological Society, London, Special Publications, 423(1), 387–437.

Kasprak, A. H., Sepúlveda, J., Price-Waldman, R., Williford, K. H., Schoepfer, S. D., Haggart, J. W., Ward, P.D., Summons, R.E., & Whiteside, J.H. (2015). Episodic photic zone euxinia in the northeastern Panthalassic Ocean during the end-Triassic extinction. Geology, 43(4), 307–310.

Kodner, R. B., Pearson, A., Summons, R. E., & Knoll, A. H. (2008). Sterols in red and green algae: quantification, phylogeny, and relevance for the interpretation of geologic steranes. Geobiology, 6(4), 411–420.

Kuypers, M. M., van Breugel, Y., Schouten, S., Erba, E., & Damsté, J. S. S. (2004). N2-fixing cyanobacteria supplied nutrient N for Cretaceous oceanic anoxic events. Geology, 32(10), 853–856.

Lewis, T. L., & Schwietering, J. F. (1971). Distribution of the Cleveland black shale in Ohio. Geological Society of America Bulletin, 82(12), 3477–3482.

Marynowski, L., & Filipiak, P. (2007). Water column euxinia and wildfire evidence during deposition of the Upper Famennian Hangenberg event horizon from the Holy Cross Mountains (central Poland). Geological Magazine, 144(3), 569–595.

Marynowski, L., Zatoń, M., Rakociński, M., Filipiak, P., Kurkiewicz, S., & Pearce, T. J. (2012). Deciphering the upper Famennian Hangenberg Black Shale depositional environments based on multi-proxy record. Palaeogeography, Palaeoclimatology, Palaeoecology, 346, 66–86.

Maynard, J. B. (1981). Carbon isotopes as indicators of dispersal patterns in Devonian-Mississippian shales of the Appalachian Basin. Geology, 9(6), 262–265.

McGhee, G. R., Clapham, M. E., Sheehan, P. M., Bottjer, D. J., & Droser, M. L. (2013). A new ecological-severity ranking of major Phanerozoic biodiversity crises. Palaeogeography, Palaeoclimatology, Palaeoecology, 370, 260–270.

Moldowan, J. M., Fago, F. J., Lee, C. Y., Jacobson, S. R., Watt, D. S., Slougui, N.-E., … Young, D. C. (1990). Sedimentary 24-*n*-propylcholestanes, molecular fossils diagnostic of marine algae. Science, 247(4940), 309–312.

Myrow, P. M., Ramezani, J., Hanson, A. E., Bowring, S. A., Racki, G., & Rakociński, M. (2014). High-precision U–Pb age and duration of the latest Devonian (Famennian) Hangenberg event, and its implications. Terra Nova, 26(3), 222–229.

Over, D. J. (2007). Conodont biostratigraphy of the Chattanooga Shale, Middle and Upper Devonian, southern Appalachian Basin, eastern United States. Journal of Paleontology, 81(6), 1194–1217.

Perkins, R. B., Piper, D. Z., & Mason, C. E. (2008). Trace-element budgets in the Ohio/Sunbury shales of Kentucky: constraints on ocean circulation and primary productivity in the Devonian–Mississippian Appalachian Basin. Palaeogeography, Palaeoclimatology, Palaeoecology, 265(1), 14–29.

Peters, K. E., Walters, C. C., & Moldowan, J. M. (2005). Petroleum systems through time: Devonian source rocks: The biomarker guide (Vol. 2). Cambridge University Press, 794–807.

Racki, G., Rakociński, M., Marynowski, L., & Wignall, P. B. (2018). Mercury enrichments and the Frasnian-Famennian biotic crisis: A volcanic trigger proved? Geology, 46(6), 543–546.

Rashby, S. E., Sessions, A. L., Summons, R. E., & Newman, D. K. (2007). Biosynthesis of 2-methylbacteriohopanepolyols by an anoxygenic phototroph. Proceedings of the National Academy of Sciences, 104(38), 15099–15104.

Ricci, J.N., Coleman, M.L., Welander, P.V., Sessions, A.L., Summons, R.E., Spear, J.R., and Newman, D.K. (2014). Diverse capacity for 2-methylhopanoid production correlates with a specific ecological niche: The ISME journal, 8, 675-684.

Rimmer, S. M., Thompson, J. A., Goodnight, S. A., & Robl, T. L. (2004). Multiple controls on the preservation of organic matter in Devonian–Mississippian marine black shales: geochemical and petrographic evidence. Palaeogeography, Palaeoclimatology, Palaeoecology, 215(1), 125–154.

Rimmer, S. M., Rowe, H. D., Hawkins, S. J., & Francis, H. (2010). Geochemistry of the Cleveland member of the Ohio Shale, Appalachian Basin: Indicators of depositional environment during sediment accumulation. Kirtlandia, 57, 3–12.

Rohrssen, M., Love, G. D., Fischer, W., Finnegan, S., & Fike, D. A. (2013). Lipid biomarkers record fundamental changes in the microbial community structure of tropical seas during the Late Ordovician Hirnantian glaciation. Geology, 41(2), 127–130.

Rooney, A., Goodhue, R., & Clayton, G. (2015). Stable nitrogen isotope analysis of the Upper Devonian palynomorph, Tasmanites. Palaeogeography, Palaeoclimatology, Palaeoecology, 429, 13–21.

Sallan, L. C., & Coates, M. I. (2010). End-Devonian extinction and a bottleneck in the early evolution of modern jawed vertebrates. Proceedings of the National Academy of Sciences, 107(22), 10131–10135.

Schwark, L., & Empt, P. (2006). Sterane biomarkers as indicators of Palaeozoic algal evolution and extinction events. Palaeogeography, Palaeoclimatology, Palaeoecology, 240(1), 225–236.

Schwark, L., & Frimmel, A. (2004). Chemostratigraphy of the Posidonia Black Shale, SW-Germany: II. Assessment of extent and persistence of photic-zone anoxia using aryl isoprenoid distributions. Chemical Geology, 206(3–4), 231–248.

Scott, C., & Lyons, T. W. (2012). Contrasting molybdenum cycling and isotopic properties in euxinic versus non-euxinic sediments and sedimentary rocks: Refining the paleoproxies. Chemical Geology, 324, 19–27.

Spaak, G., Edwards, D. S., Allen, H. J., Grotheer, H., Summons, R. E., Coolen, M. J., & Grice, K. (2018). Extent and persistence of photic zone euxinia in Middle–Late Devonian seas–Insights from the Canning Basin and implications for petroleum source rock formation. Marine and Petroleum Geology, 93, 33–56.

Summons, R. E., & Powell, T. G. (1986). Chlorobiaceae in Palaeozoic seas revealed by biological markers, isotopes and geology. Nature, 319(6056), 763–765.

Tribovillard, N., Algeo, T. J., Lyons, T., & Riboulleau, A. (2006). Trace metals as paleoredox and paleoproductivity proxies: an update. Chemical Geology, 232(1), 12–32.

Tuite, M. L., & Macko, S. A. (2013). Basinward nitrogen limitation demonstrates role of terrestrial nitrogen and redox control of δ15N in a Late Devonian black shale. Geology, 41(10), 1079–1082.

Tulipani, S., Grice, K., Greenwood, P. F., Haines, P. W., Sauer, P. E., Schimmelmann, A., … Playton, T. (2015). Changes of palaeoenvironmental conditions recorded in Late Devonian reef systems from the Canning Basin, Western Australia: A biomarker and stable isotope approach. Gondwana Research, 28(4), 1500–1515.

Tulipani, S., Grice, K., Greenwood, P. F., Schwark, L., Boettcher, M. E., Summons, R. E., & Foster, C. B. (2015). Molecular proxies as indicators of freshwater incursion-driven salinity stratification. Chemical Geology, 409, 61–68.

Welander, P. V., Coleman, M. L., Sessions, A. L., Summons, R. E., & Newman, D. K. (2010). Identification of a methylase required for 2-methylhopanoid production and implications for the interpretation of sedimentary hopanes. Proceedings of the National Academy of Sciences, 107(19), 8537–8542.

Welander, P. V., & Summons, R. E. (2012). Discovery, taxonomic distribution, and phenotypic characterization of a gene required for 3-methylhopanoid production. Proceedings of the National Academy of Sciences, 109(32), 12905–12910.

Whiteside, J. H., & Grice, K. (2016). Biomarker records associated with mass extinction events. Annual Review of Earth and Planetary Sciences, 44, 581–612.

Woodrow, D. L., Dennison, J. M., Ettensohn, F. R., Sevon, W. T., & Kirchgasser, W. T. (1988). Middle and Upper Devonian stratigraphy and paleogeography of the central and southern Appalachians and eastern Midcontinent, USA.

Zagger, G. W. (1995). Conodont biostratigraphy and sedimentology of the latest Devonian of northeast Ohio (PhD Thesis). Case Western Reserve University.

CHAPTER THREE

Tracking Environmental Change in a Jurassic rift lake: implications for interpreting paleoenvironmental records in deep time

Eva E. Stüeken, Aaron Martinez, Gordon Love, Paul E. Olsen, Steve Bates, Timothy W. Lyons

Abstract

It is widely agreed that the Earth's atmosphere and oceans have undergone major redox changes over the last 2.5 billion years. However, the magnitude of these shifts remains a point of contention because it is difficult to reconstruct concentrations of dissolved O_2 from indirect proxies in sedimentary archives. In this study, we show that an additional complicating factor that is rarely considered may be the pH of the water column. We analyzed rock samples from the early Jurassic Towaco Formation in the Newark basin (eastern USA), comprising deposits of a rift lake that became temporarily redox stratified. New biomarker evidence including terpane and carotenoid biomarker proxies points to increasingly saline aquatic conditions during the second half of the lake's history, with a salinity and redox induced stratification that may also explain the disappearance of macrofauna at this time. Distinctive lipid biomarker assemblages and stable nitrogen isotopic ratios support mineralogical indications that the lake was alkaline ($pH \geq 9$) during its saline history. In summary, our results highlight the potential importance of aquatic pH in influencing global biogeochemical cycles for multiple

elements and for yielding a characteristic combination of ancient nitrogen isotope and lipid biomarker signatures under highly alkaline conditions.

1. Introduction

Secular changes in the redox state of Earth's atmosphere and oceans have fundamentally impacted the evolution of biogeochemical cycles. For partial example, sequential oxygenations of the Earth's atmosphere, surface ocean, and finally deep ocean (Anbar et al., 2007; Hardisty et al., 2017; Scott et al., 2008; Stüeken et al., 2015a) have influenced the terrestrial weathering of sulfate, build-up of oceanic nitrate, and concentrations of trace metals in the ocean, respectively (Partin et al., 2015; Sperling et al., 2015; Zerkle et al., 2017). Thus, along with implications for the evolutionary history of early biology, there is significant interest in understanding the redox evolution of the early Earth. Typically, with the lack of direct evidence, paleo-redox conditions are mostly inferred through use of redox proxies, many of which relate to the deposition and preservation of redox sensitive major and minor elements in the geologic record (such as iron or the transition metals; see Lyons et al., 2014).

Although atmospheric and dissolved oxygen levels imparted the first-order control on many biogeochemical transitions, it is conceivable that biogeochemical cycles have also been affected by other environmental parameters, including aquatic pH. Recent model estimates suggest a gradual increase in seawater pH from ~6.5 in the Archean to modern values of > 8 (Halevy and Bachan, 2017; Isson and Planavsky, 2018), which may have influenced the mobility of major and minor elements. Importantly, within the

natural circumneutral range of pH 6-9, the systematics of important redox-proxy parameters are affected. For example, the solubility of ferrous iron in anoxic waters drops by more than an order of magnitude per one unit increase in pH (Morgan and Lahav, 2007), while molybdenum becomes more soluble, even in the presence of H_2S (Helz et al., 2011). Transition metal cations of Co, Ni, Cu and Zn behave like iron and show a decline in solubility with higher pH (Tack et al., 1996). We hypothesize that long-term changes in seawater pH as outlined by Halevy & Bachan (2017) could have contributed to the magnitude of enrichment in authigenic iron and other transition metals in marine sediments, and thus color the interpretation of paleo-redox records.

To test this hypothesis, we analyzed samples from the Early Jurassic Towaco Formation of the Newark Supergroup in the eastern U.S. As reviewed below, the Towaco Formation was deposited in a lacustrine setting with intermittent anoxic, high-pH (alkaline) intervals (Kruge et al., 1990; Olsen et al., 1996s; Pratt, 1989), comparable to other units in the Newark rift lakes around this time (El Tabakh and Schreiber, 1994; Van Houten, 1962). This paper delves into the effects of high pH on biogeochemical proxies using the Towaco set of lacustrine rocks as a natural laboratory. To support this effort, we provide here a comprehensive set of lipid biomarker analyses as an independent control on the salinity, stratification dynamics, and long-term hydrologic evolution of this lacustrine system. We determine that the distinctive and well-studied stratigraphy of this lacustrine system is clearly delineated and supported using discrete suites of biomarker parameters. Further, as biomarker parameters are by nature products of active biogeochemical cycles, we use these factors to assist in interpreting the underlaying pH

of the system and the resulting effects on biogeochemical proxies. This chapter will focus solely on organic geochemical parameters and their interpretation; for the full integrated paper see Stüeken et al. (2019), *Geochimica et Cosmochimica Acta*.

2. Geologic setting

The Newark Supergroup in the eastern United States comprises a series of fluvial and lacustrine sedimentary rocks interbedded with basalt flows, in its younger parts, and intruded by diabase (diorite) sills and dikes (**Fig. 3.1**). The sediments were deposited in a series of half-grabens (**Fig. 3.2A**) that formed at tropical to subtropical latitudes during the early Mesozoic break-up of Pangaea prior to the opening of the central North Atlantic Ocean (e.g. Hay et al., 1982; Kent and Tauxe, 2005; Schlische, 1990; Witte et al., 1991). During the Triassic and extending into the Jurassic, regional climate was cycled quasi-periodically from relatively humid to arid conditions, with the end-members depending on paleolatitude (Kent and Tauxe, 2005; Olsen, 1986; Olsen and Kent, 1996). The Towaco Formation of the Newark Basin was deposited at approximately 21° N paleolatitude and experienced both arid and humid conditions. It is equivalent in age and comparable in lithostratigraphy to the East Berlin Formation in the Hartford Basin in Connecticut (Olsen, 2012). In the East Berlin Formation, previous studies inferred evaporitic conditions from the presence of occasional salt deposits and abundant exposure surfaces and carbon and oxygen isotopes in carbonates that point to evaporitic conditions (El Tabakh and Schreiber, 1994; Suchecki et al., 1988, this study). The humid phases are marked by the presence of very large and perennial lake sequences (Olsen,

1990). Overall, the setting may have been comparable to the modern East African rift lakes (Hay et al., 1982). Given the proximity between the Newark and Hartford basins

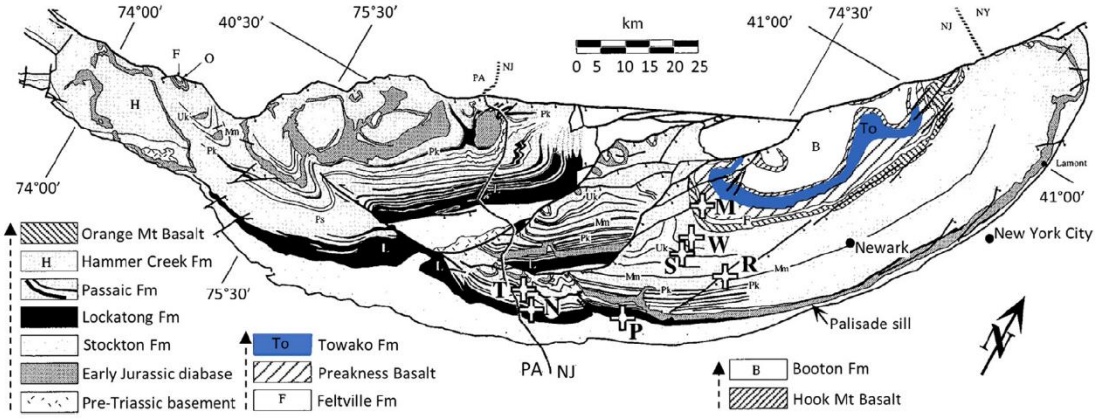

Figure 3.1: Geologic map of the Newark Basin. The early Jurassic Towaco Formation investigated in this study is highlighted in blue. The Triassic-Jurassic boundary lies within the Passaic Formation. Adapted from Olsen et al. (1996a).

and the similarities in age and depositional environment between the Towaco and East Berlin formations, it is conceivable that the two settings experienced similar conditions at this time, as will be confirmed in this study.

The sedimentary units in both basins include non-marine red beds, gray siltstones and black shales with variable amounts of carbonate. These lithologies show a striking cyclicity with recurrence intervals paced by Milankovitch cycles, indicating a strong climatic control on regional sedimentation rates, precipitation and even water chemistry (Olsen, 1986; Olsen and Kent, 1996). The shortest and most notable cycle at outcrop scale is termed the Van Houten cycle (Olsen, 1986), with an inferred duration of ~20,000 years corresponding to the precession cycle (Blackburn et al., 2013; Olsen, 1986; Olsen and Kent, 1996; Whiteside et al., 2007). At our sampling locality the stratigraphic

thickness of Van Houten cycles is roughly 25 m (Olsen et al., 1996b). A typical Van Houten cycle with a perennial lake interval as initially described by Van Houten (1965) and El Tabakh & Schreiber (1994) for other units in the Newark Basin includes three divisions with varying thicknesses (**Fig. 3.2B**; Olsen, 1986; Olsen and Kent, 1996). Starting from the base: (i) a red to gray mudstone with progressively upward increasing thin- bedding and decreasing abundances of desiccation cracks, roots and/or burrows is overlain by (ii) planer-laminated shale, sometimes organic rich, with a basal horizon that is rich in fossils of fishes, crustaceans, and sometimes reptiles followed by (iii) another gray to red mudstone with a progressive decrease in bedding and an increase of desiccation cracks and roots or burrows. Divisions 1 and 3 can include evaporite pseudomorphs after Na-Ca sulfates (glauberite). All three divisions contain variable amounts of carbonate, including dolomite and calcite (El Tabakh and Schreiber, 1994; Kruge et al., 1990; Van Houten, 1965). In some Van Houten cycles in the Newark and Hartford basins, including the East Berlin Formation that is time-equivalent to the Towaco Formation (Olsen, 2012), magnesite and analcime have been reported from the black shale facies (El Tabakh and Schreiber, 1994; Gierlowski-Kordesch and Rust, 1994; Van Houten, 1962), and authigenic albite has been reported from gray mudstones (Kruge et al., 1990). It is uncertain how many of these apparent evaporitic minerals are of primary versus diagenetic origin (Smoot and Olsen, 1994).

Collectively, this sequence of lithologies and diagenetic minerals is interpreted as a climatically induced consequence of deepening and shallowing of an alkaline, sometimes saline lake, where the black shale facies (division 2) represents the high-stand

interval (Olsen and Kent, 1996). The high abundance of organic matter (up to 8 wt% TOC in some cycles) and the absence of burrows in the deepest water facies likely indicate anoxic bottom waters (El Tabakh and Schreiber, 1994; Kruge et al., 1990; Olsen and Kent, 1996). During their deepest intervals, Newark lakes were probably chemically stratified, consistent with our acquired geochemical data set below.

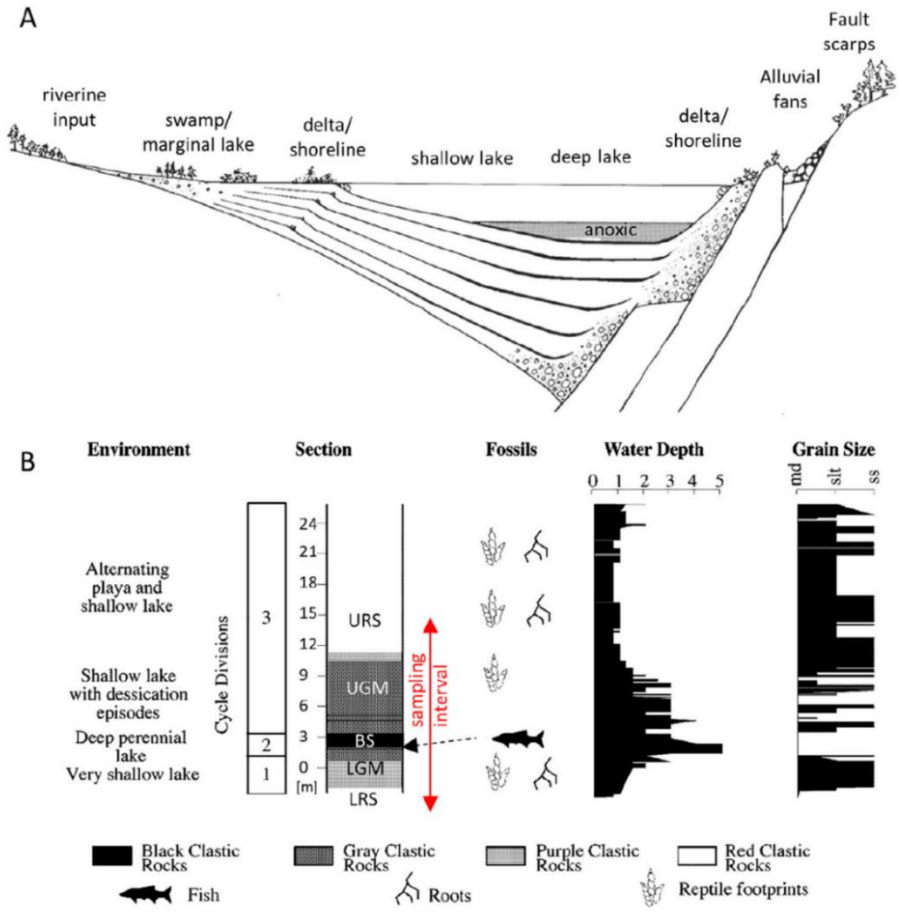

Figure 3.2: Sedimentary facies evolution and distribution. A: The lake basin formed in a half-graben where activity along the normal fault created accommodation space for sedimentation (adapted from Olsen, 1988b). Our sample set captures the marginal/shoreline facies (red siltstone), the shallow lake facies (gray mudstone) and deep lake facies (black shale). B: Schematic of a Van Houten cycle of lake deepening and shallowing in the Towaco Formation as inferred from the sedimentary record (adapted from Olsen, 1997). LRS = lower red siltstone, LGM = lower gray mudstone, BS = black shale, UGM = upper gray mudstone, URS = upper red siltstone.

We collected samples from two drill-cores (C-128 and PT-14, **Fig. 3.1**) which traversed through one Van Houten cycle (that containing the Colfax Bed, Olsen, 2011) of the early Jurassic Towaco Formation in the Newark basin (Olsen, 2011; Olsen et al., 1996a; Weems and Olsen, 1997). The Towaco Formation is approximately 350 m thick and bracketed by the Preakness Basalt and the Hook Mountain Basalt (**Fig. 3.1**; Olsen et al., 1996a,; Schlische, 1990). This interval was chosen because it was easily accessible through relatively fresh drill-core and because of its relatively low thermal maturity (%R_0 = 0.50, H/C ratios ~0.95, T_{max} = 426°C, Hatcher and Romankiw, 1985; Malinconico, 2002; Pratt et al., 1985). Furthermore, this cycle contains a thin but distinctive ash bed – the Pompton Tuff (Olsen, 2012) – which allows us to correlate this unit with a Van Houten cycle in the East Berlin Formation in the Hartford basin, another rift lake of the Newark Supergroup. Previous studies of the Hartford basin have reported magnesite ($MgCO_3$) and organic biomarkers indicative of moderately saline and alkaline conditions (Gierlowski-Kordesch and Rust, 1994; Kruge et al., 1990). These biomarker alkane features included elevated carotanes and extended tricyclic terpanes, which are commonly enhanced in saline environments, including alkaline lakes (De Grande et al., 1993), although they are not necessarily indicative of saline conditions on their own. Both β- and γ-carotane have been reported from analyses of the Towaco Formation (Kruge et al., 1990; Pratt, 1989). Lastly, the carbon isotope composition and aromaticity of the black shales in the Towaco Formation suggest a high percentage (60-90%) of algal biomass, with only relatively small contributions of detrital plant material (Spiker et al.,

1988, this study), which allows us to investigate biogeochemical processes occurring primarily in the local water column.

3. Analytical methods

3.1. Sample preparation

Sample preparation and analyses followed standard protocols. The outer surfaces of the core samples were removed with a water-cooled rock saw. The samples were then hammered into sub-cm sized chips, which were transferred into an acid-washed glass beaker and sonicated for a few seconds in 2M HCl. The acid was removed during multiple rinses with DI-H_2O (18 MΩ) in the sonic bath. The clean rock ships were air-dried in loosely covered plastic weigh boats and then pulverized to a fine powder in a ball mill. The powders were stored in acid-washed plastic vials.

3.2. Total nitrogen and organic carbon

Sample preparation and analyses of carbon and nitrogen isotopes were carried out at the University of Washington. A ~0.5g aliquot of each powder was weighed into a glass centrifuge tube and decarbonated with 6M HCl at 60°C overnight (Stüeken et al., 2015b; Stüeken et al., 2015c). The acid was refreshed twice and stirred with a glass rod. The powders were then washed three times with DI-H_2O (18 MΩ) and dried for three days in a closed oven at 60°C. For analyses of total organic carbon (TOC), total nitrogen (TN), organic carbon isotopes and total nitrogen isotopes, the dry powders were weighed into 9 x 5 mm tin capsules and analyzed by flash combustion with an Costech EA

coupled via a Conflo III to Thermo Finnigan MAT253 IRMS. The average reproducibility of samples was 0.25‰ for $\delta^{15}N_{bulk}$ (1 standard deviation, SD), 0.15‰ for $\delta^{13}C_{org}$ (1 SD), 0.5% for TOC (relative error, RE), 5% for TN (RE), and 5% for C/N ratios (RE). We obtained values of $\delta^{15}N_{bulk}$ = 5.37 ± 0.46‰, $\delta^{13}C_{org}$ = -37.84 ± 0.61‰, TOC = 7.4 ± 0.2% and TN = 1019 ± 96 ppm for our UW-McRae in-house standard, which agree well with previous studies (Stüeken et al., 2015b; Stüeken et al., 2015c). The isotopic data were expressed in delta notation relative to VPDB for $\delta^{13}C_{org}$ and relative to air for $\delta^{15}N$: δ [‰] = ($^{x/y}R_{sample}$ / $^{x/y}R_{standard}$ - 1), where $^{x/y}R = {}^{15}N/{}^{14}N$ for nitrogen and $^{13}C/^{12}C$ for carbon.

3.3. Lipid biomarker analysis

Crushed rock powders were extracted in a CEM Microwave Accelerated Reaction System (MARS) at 100°C in a 9:1 DCM:MeOH (v/v) mixture for 15 min to yield rock bitumens. Full laboratory procedural blanks with pre-combusted sand were performed in parallel to ensure that any background hydrocarbon compounds were negligible in comparison with biomarker analyte abundances. Saturate hydrocarbon and aromatic fractions were obtained by silica gel column chromatography; the saturate hydrocarbon fractions were eluted with n-hexane and the aromatic hydrocarbon fractions with a 1:1 (v/v) mixture of DCM and n-hexane.

Saturated hydrocarbon fractions were analyzed by metastable reaction monitoring–gas chromatography–mass spectrometry (MRM-GC-MS) conducted at UC Riverside on a Waters AutoSpec Premier mass spectrometer equipped with a HP 6890

gas chromatograph and DB-1MS coated capillary column (60 m × 0.25 mm, 0.25 μm film thickness) using He as carrier gas. The GC temperature program consisted of an initial hold at 60°C for 2 min, heating to 150°C at 10 °C/min, followed by heating to 320°C at 3°C/min and a final hold for 22 min. Analyses were performed via splitless injection in electron impact mode, with an ionization energy of 70 eV and an accelerating voltage of 8 kV. MRM transitions for C_{27}–C_{35} hopanes, C_{31}–C_{36} methylhopanes, C_{21}–C_{22} and C_{26}–C_{30} steranes, C_{30} methylsteranes and C_{19}–C_{26} tricyclics were monitored. Polycyclic biomarker alkanes (tricyclic terpanes, hopanes, steranes, etc.) were quantified by addition of a deuterated C_{29} sterane standard [d4-ααα-24-ethylcholestane (20R)] to saturated hydrocarbon fractions and comparison of relative peak areas.

Both saturated and aromatic hydrocarbon fractions were analyzed in both full scan and single ion monitoring methods at UC Riverside by gas chromatography–mass spectrometry (GC–MS) on an Agilent 7890A GC system coupled to an Agilent 5975C inert MSD mass spectrometer. The GC was equipped with a DB1-MS capillary column (60 m × 0.32 mm, 0.25 μm film thickness), and helium was used as the carrier gas. The temperature program for GC-MS full scan and selected ion monitoring was 60ºC (2 min hold), ramped to 150ºC at 20ºC/min, then to 325ºC at 2ºC/min and hold at 325ºC for 20 min. C_{40} carotanes, including β-carotane, γ-carotane and their structural isomers, were identified in saturated hydrocarbon fractions based on 125 Dalton (Da) mass chromatograms and verified from mass spectra and retention time. Aromatic carotenoid biomarkers were monitored for on m/z 133 and 134 ion chromatograms with retention times verified by in-house standards.

4. Results

4.1. Sample description

The two drill cores, which transect the same stratigraphic unit, show matching lithofacies with similar thicknesses (**Fig. 3.3 and 3.4**) and thus will be presented in a single description. The sampled section can be broadly divided into five parts: (i) a lower red siltstone to silty shale; (ii) a lower greenish-gray mudstone, 2 m thick; (iii) a black shale, 1.5 m thick; (iv) an upper greenish-gray mudstone, 5 m thick and (v) an upper red siltstone to silty shale. Units (i) and (v) are mostly composed of interlaminated red shale and red siltstone with lenses of fine sandstone. Individual laminae are several mm thick and sometimes graded or wavy. Some coarser-grained laminae display cross-bedding, while the finer intervals – especially towards the base and top of the two drill core sections – show pedogenic features, including desiccation cracks and rare nodular carbonate. Units (ii) and (iv) are mostly composed of interbedded massive and bioturbated mudstones with weakly graded cm-scale silty shale interbeds. Bioturbation is most prevalent proximal to the red siltstone units. In unit (ii), the grain size generally decreases upward from silt- to clay-dominated, whereas unit (iv) shows a coarsening-upward trend. The basal 10 cm of this bed is microlaminated and contains whole fish fossils and a distinct pyritic ash bed that is about 0.5cm thick (the Pompton Tuff). This microlaminite horizon is traceable over many kilometers in the Towaco Formation (Olsen, 1988a).

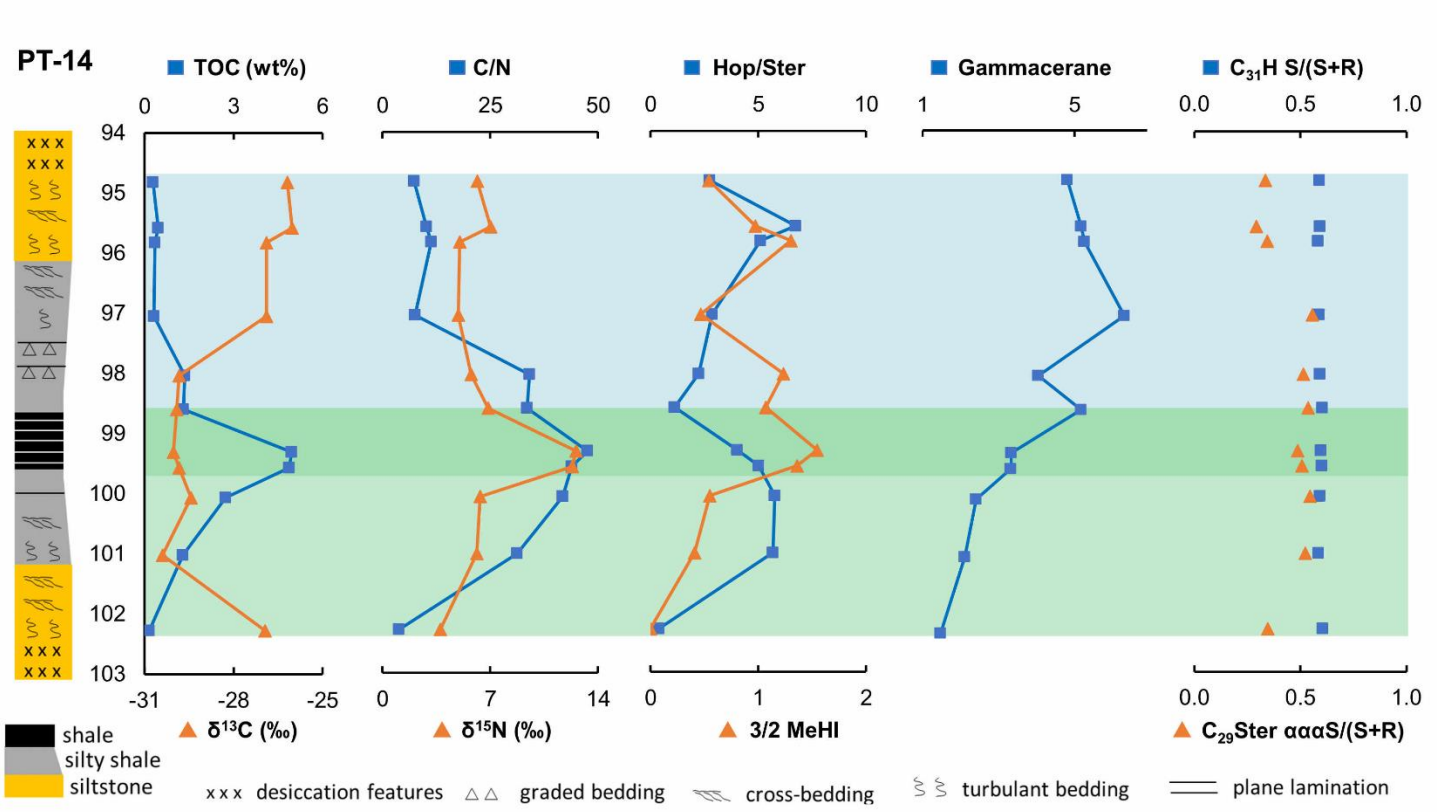

Figure 3.3: Chemostratigraphy of core PT-14 through the Towaco Formation. TOC = total organic carbon (wt%); C/N = carbon/nitrogen ratio (wt%/wt%); Hop/Ster = C_{27}-C_{35} hopanes/C_{27}-C_{29} regular steranes; Gammacerane = 10*(gammacerane/C_{30} αβ hopane); C_{31}H S/(S+R) = C_{31} αβ hopane S/(S+R) ratio for thermal maturity; $\delta^{13}C_{org}$ ‰ (vs VPDB); $\delta^{15}N_{total}$ ‰ (vs AIR); 3/2 MeHI = 3β-methylhopane index/2α-methylhopane index; C_{29}Ster ααα S/(S+R) = C_{29} sterane ααα S/(S+R) ratio for thermal maturity. Light shaded green bar = water level increase as inferred from lithofacies (grain size fining). Dark shaded green bar = water level highstand and thermohaline stratification as inferred from lithofacies. Shaded blue bar = water level shrinkage by evaporation as inferred from biomarkers.

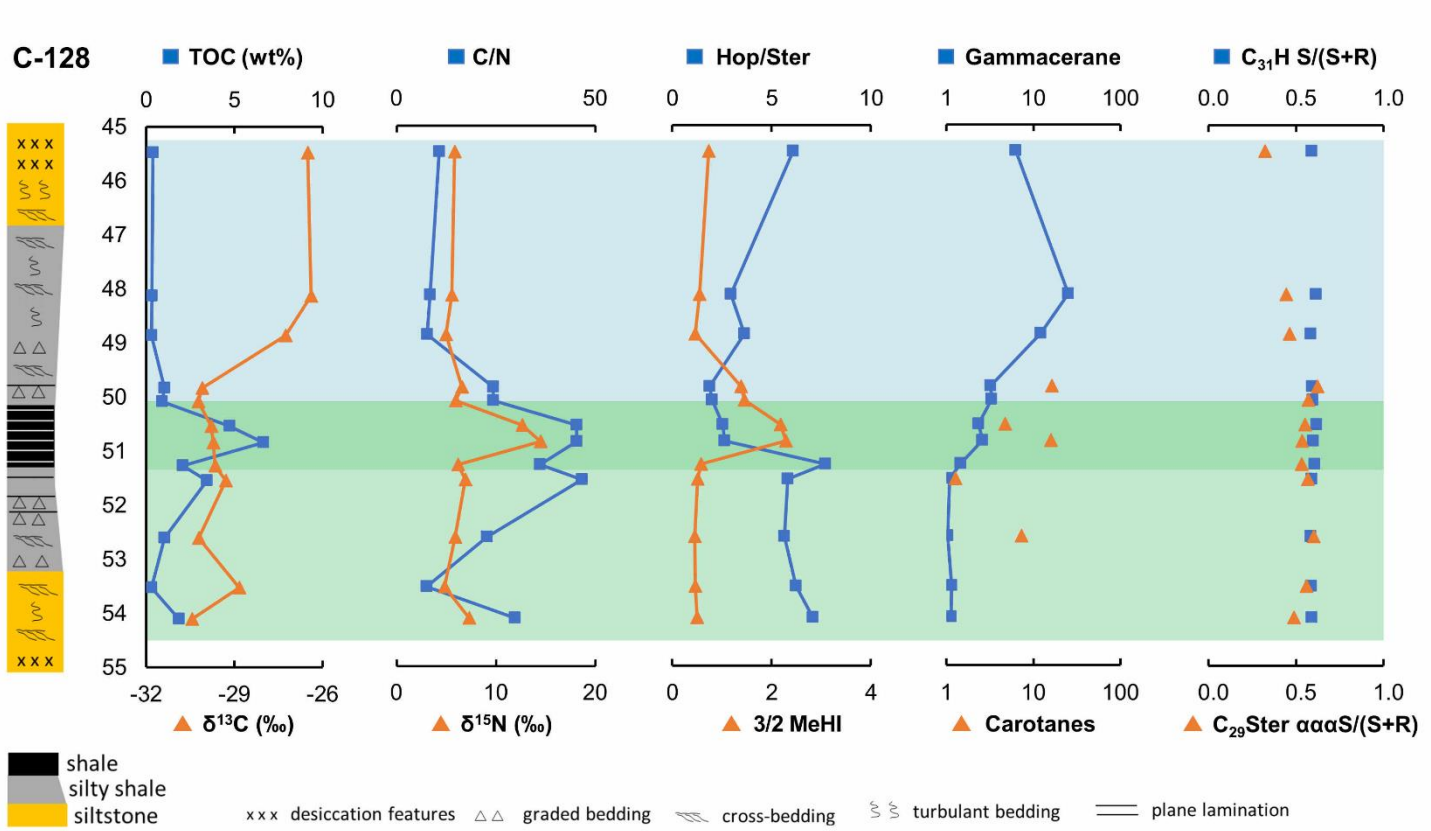

Figure 3.4: Chemostratigraphy of core C-128 through the Towaco Formation. TOC = total organic carbon (wt%); C/N = carbon/nitrogen ratio (wt%/wt%); Hop/Ster = C_{27}-C_{35} hopanes/C_{27}-C_{29} regular steranes; Gammacerane = 10*(gammacerane/C_{30} αβ hopane); C_{31}H S/(S+R) = C_{31} αβ hopane S/(S+R) ratio for thermal maturity; $\delta^{13}C_{org}$ ‰ (vs VPDB); $\delta^{15}N_{total}$ ‰ (vs AIR); 3/2 MeHI = 3β-methylhopane index/2α-methylhopane index; Carotanes = sum of carotane biomarkers/n-C_{21+22} alkane; C_{29}Ster ααα S/(S+R) = C_{29} sterane ααα S/(S+R) ratio for thermal maturity. Light shaded green bar = water level increase as inferred from lithofacies (grain size fining). Dark shaded green bar = water level highstand and thermohaline stratification as inferred from lithofacies. Shaded blue bar = water level shrinkage by evaporation as inferred from biomarkers.

4.2 Organic carbon and nitrogen systematics

Total organic carbon (TOC) abundances show a distinct peak up to 6.6% in the 1-m-thick black shale horizon in both cores (**Fig. 3.3 and 3.4**, **Table 3.1**). This peak is established somewhat gradually over the lower 2 m of the gray mudstone, with intermediate values around 1%, but it ends comparatively abruptly with TOC values dropping down to < 0.5% in the upper gray mudstone. Total nitrogen is well correlated with organic carbon in both cores ($r^2 = 0.91$), indicating that it is most likely organic-bound or derived from organic matter degradation. Ratios of organic carbon to total nitrogen (C/N) covary with TOC (**Fig. 3.5B**), meaning that samples with higher sedimentary organic matter tend to be relatively nitrogen-depleted. This trend levels off slightly above ~2% TOC (**Fig. 3.5B**) where the slope between C/N ratios and TOC becomes shallower.

Organic carbon isotopes ($\delta^{13}C_{org}$) range from -24‰ to -30‰, where the lighter values occur mostly within the lower gray mudstone and the black shale. Above the black shale, $\delta^{13}C_{org}$ is systematically heavier (**Fig. 3.3 and 3.4**). Samples with $\delta^{13}C_{org}$ > -29‰ all have < 0.5% TOC and vice versa (**Fig. 3.5D**). Total nitrogen isotope data ($\delta^{15}N_{bulk}$) range from 3‰ to 15‰, in good agreement with two previous measurements (Spiker, 1985). Values above 6‰ are restricted to the black shale horizon (**Fig. 3.3 and 3.4**), which is also the interval with the lowest $\delta^{13}C_{org}$ and the highest TOC and C/N values. Given that this interval occurs in the middle of the section, and there is no evidence of high maturity in any of the strata investigated, it is unlikely that the correlation between $\delta^{15}N_{bulk}$ and C/N is a metamorphic feature (cf. Haendel et al., 1986).

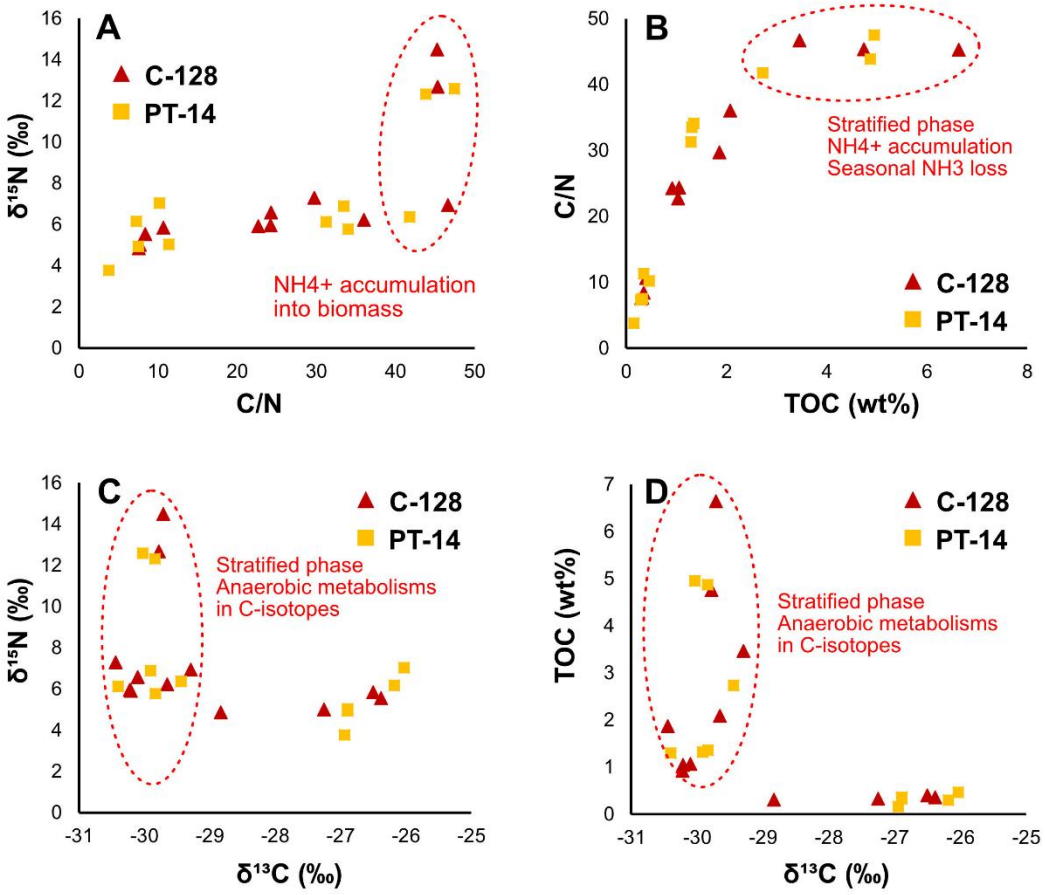

Figure 3.5: Carbon-nitrogen scatter plots. A: bulk $\delta^{15}N$ versus organic carbon to total nitrogen (C/N) ratios. The kink in the slope likely indicates the onset of stratification and build-up of an isotopically enriched NH_4^+ reservoir in the water column that became bioavailable to algae and prokaryotes. B: C/N ratios versus total organic carbon (TOC). The correlation between the two parameters likely suggests higher rates of NH_4^+/NH_3 production and NH_3 loss from biomass (increasing C/N) under progressively more anoxic conditions that favor increasing TOC buildup. The kink in the slope may reflect a transition towards stratification and seasonal NH_3 release as in modern Mono Lake (Jellison et al., 1993). C: Bulk $\delta^{15}N$ versus organic $\delta^{13}C$ isotopes. The interval of heaviest $\delta^{15}N$ – interpreted as redox stratified – is characterized by depleted $\delta^{13}C$, which may indicate anaerobic metabolisms or utilization of isotopically light DIC in a stratified water column. D: TOC versus organic $\delta^{13}C$, showing that that anaerobic metabolisms (light $\delta^{13}C_{org}$) correspond to intervals of high biomass accumulation, consistent with redox stratified conditions.

4.3. Lipid biomarker record

We used the selectivity and sensitivity of multiple reaction monitoring (MRM)-GC-MS to detect and scrutinize terpenoid alkane biomarker distributions (hopanes, steranes, methylhopanes, methysteranes and other polycyclic biomarker alkanes) alongside traditional full scan GC-MS analysis of saturated and aromatic hydrocarbon fractions prepared from the rock bitumens (solvent-extractable organic matter). The hopane and sterane maturity profiles from our samples (**Table 3.2**) as well as the other major polycyclic alkane features are self-consistent with the thermal maturity and saline lacustrine paleoenvironmental setting, suggesting they are syngenetic with the host strata. Consistency checks include: 1) similar stereoisomer maturity patterns for hopanes and steranes regardless of carbon number; 2) distinctive polycyclic alkane compound distributions (such as high gammacerane) that are not commonly associated with contaminant background signal along with no discernible presence of suspicious younger biomarker features, e.g., oleanane from angiosperms. Thermal maturity parameters, including C_{31} hopane isomerization at 22S/[22S+22R], C_{30} hopane βα/(βα+αβ), and C_{29} ααα S/(ααα S+ααα R) ratios, are all consistent with a mid- oil window stage of thermal maturity prior to peak oil generation (**Fig. 3.3 and 4; Table 3.2**), consistent with previous Rock-Eval pyrolysis and NMR data from the Towako Fm. (Hatcher and Romankiw, 1985; Pratt et al., 1985). Thus, these samples were ideal targets for detailed biomarker investigation.

Key characteristics of the biomarker assemblages were calculated from molecular ratios for twelve C-128 and eleven PT-14 samples (**Table 3.2**). Hopane/sterane ratios are

typically elevated (range = 0.4 – 7.7; median = 4.0; **Fig. 3.3 and 3.4**) relative to the Phanerozoic marine average for organic-rich marine strata (which are generally in the 0.5-2.0 range, Peters et al., 2005; Rohrssen et al., 2013). In both cores, the lowest hopane/sterane ratios are recorded in the upper parts of unit (iii) black shales with both siltstones and silty shales having more elevated values. There is no detectable signal recorded from MRM-GC-MS for 24-*n*-propylcholestanes (24-npc) in any sample (<0.1% of total C_{27}-C_{30} steranes).

The major hopane peak in all samples is the C_{30}-17α,21β(H) (hereafter, C_{30}H); typical ratios of C_{30}H to C_{31}H(22R) homohopanes (C_{31}HR/ C_{30}H) are between 0.2 and 0.3 (**Table 3.2**). The homohopane index (HHI; C_{35} homohopane/ΣC_{31}-C_{35} homohopanes) is moderate to high throughout both studied sections ranging from 0.9 – 5.1 (**Table 3.2**). Values are typically elevated in the lower gray and black shales and lowest in the upper siltstone. A ratio of C_{26}/C_{25} tricyclic terpanes is elevated over 1.2 for all shale units and lower than 1.2 for all siltstone samples. Gammacerane is a prominent biomarker compoundwithin samples from both cores (**Table 3.2**). The gammacerane index values [gammacerane/(gammacerane + C_{30}αβ hopane) * 10] increases up-section in both cores (**Fig. 3.3 and 3.4**) from lower values in the lower grey shale (0.7 – 1.1), moderate to high values in the black shales (1.1 – 5.5), to extreme values within the upper gray shales and siltstones (4.5 – 25.3).

2-methyl- and 3-methylhopane indices (2α-and 3β -MeHI, where these represent the percentage abundances of the particular C_{33} methylhopane relative to sum of C_{33} methylhopane and C_{32} homohopane) are moderate to high throughout the entire sample

set (**Table 3.2**). 2α- MeHI spans values from 2.1 to 15.2% while 3β -MeHI records a less dramatic but still wide range of 2.8 – 8.4%. Relative abundances of 3β -MeHI to 2α-MeHI (hereafter termed the 3β/2α ratio) are highest in the TOC-rich unit (iii) black shales (**Fig. 3.3 and 3.4**), but both ratios are typically most elevated within the low TOC siltstones. Due to poor chromatographic resolution of the more traditionally measured C_{31} methylhopane homologues, due to co-elution with large peaks of methylgammacerane, we use C_{33} methylhopanes compounds as our homolog measurement.

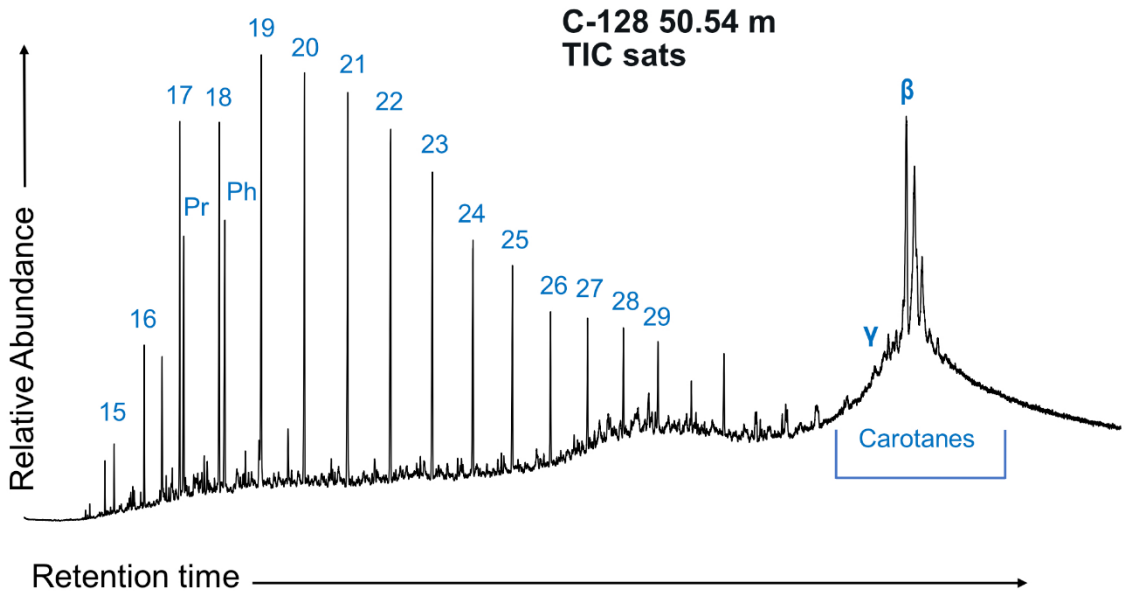

Figure 3.6: Total ion current chromatograph of C-128 50.54 saturated fraction. This is a high TOC sample showing prominent carotane biomarkers including β-carotane (β) and γ-carotane (γ). Numbers refer to the carbon number of corresponding *n*-alkane peaks. Pr = pristane; Ph = phytane.

Due to a combination of low sample size and commonly low to moderate TOC contents (~1wt%), the detailed hydrocarbon distributions for several samples are not measurable via traditional full-scan GC-MS techniques. Among the more robust lipid samples, such as the organic-rich black shales, anomalously high amounts of preserved C_{40} carotanes relative to n-alkanes are observable (**Fig. 3.3, 3.4, and 3.6**). Full-scan total ion currents (TICs) of these samples are typically dominated by a large signal of β-carotane, with lesser amounts of γ-carotane along with various structural isomers of these. When measurable, all samples show low pristane/phytane ratios (<1.0), though this is again biased to favor higher TOC rocks with more extractable lipid content (**Table 3.1 and 3.2**). We found no detectable signals from aromatic carotenoid biomarkers – that is, markers for anoxygenic photosynthetic bacteria such as Chlorobi – in any sample, which implies that photic zone euxinia was not sustained in the water column during deposition of these strata. This conclusion is consistent with the corresponding iron mineral speciation data, as only a small subset of the overall rock set showed deposition under possibly euxinic (anoxic and sulfidic) conditions (as shown in Stüeken et al., 2019).

5. Discussion

5.1. Testing geochemical proxies for a lacustrine depositional setting

The fossil record of the Newark basin preserves no clear evidence of marine influence (Olsen, 1988b; Olsen, 1997). Although many diverse biogeochemical processes and sedimentary constituents found here can inform our understanding of ancient marine settings, these rocks are ideally suited for putting geochemical proxy indicators of

lacustrine settings to the test. The search for robust geochemical indicators of marine or lacustrine deposition backed by sedimentological and structural evidence is long-lasting (Berner and Raiswell, 1984; Tissot and Welte, 1984). Commonly used proxies can struggle to distinguish between the various types of lacustrine settings – be they fresh, saline, and/or alkaline – due to overprinting by redox-sensitive reactions (i.e. pyrite-bound sulfur concentrations; Berner and Raiswell, 1984; and see Stüeken et al., 2019). A broad array of biomarker ratios and abundance patterns can be integrated to monitor ancient biotic input and constrain paleoenvironmental facies for rocks that have experienced a sufficiently mild thermal history, as for the sedimentary rocks here (Tissot and Welte, 1984). The well-documented stratigraphy of the Van Houten cycles allows us to test lipid signatures suggesting lacustrine settings against geological evidence.

Hopane/sterane ratios in the Newark Basin are elevated compared to typical Phanerozoic marine source rocks, which is a common feature in organic matter derived from a terrestrial or lacustrine environment due to higher bacterial contributions (Rohrssen et al., 2013; Tissot and Welte, 1984). One intriguing feature in chromatograms of all samples is the absence 24-npc steranes from pelagophyte algae (Moldowan et al., 1990). These steranes are exclusively found in marine environments and are the dominant C_{30} sterane in marine rocks and oils of Devonian age and younger (Gold et al., 2016). Due to the excellent preservation biomarker lipids, especially in the organic-rich black shales, the absence of these C_{30} regular steranes in the Towako Fm. (<0.1% of total C_{27}-C_{29} steranes) provides a strong indication of lacustrine paleoenvironments for all strata analyzed.

More evidence of lacustrine deposition comes from an array of terpenoid biomarker parameters including the $C_{31}HR/ C_{30}H$ ratio and C_{26}/C_{25} tricyclic terpanes (Peters et al 2005; Zumberge, 1987). The $C_{31}HR$ homohopanes are common in marine settings, where they typically arise from the degradation and diagenesis of various diverse bacteriohopanepolyols (Peters et al., 2005; Talbot and Farrimond, 2007). Thus, relatively low $C_{31}R/ C_{30}H$ ratios are often characteristic of lacustrine depositional environments. Similarly, deep marine facies have been observed to record elevated amounts of the C_{25} tricyclic terpane – lack of this marker leading to an elevated C_{26}/C_{25} ratio appears specific for lacustrine environments, at least freshwater ones (Zumberge, 1987). The comparison of these two parameters (**Fig. 3.7**) separates our data into two discrete clusters. All $C_{31}HR/ C_{30}H$ ratios are low in agreement with lacustrine origins (~0.2-0.3), but the C_{26}/C_{25} ratio decreases in the uppermost gray shale and siltstones, falling outside the typical (low salinity) lacustrine zone. This highlights a complication with the C_{26}/C_{25} parameter within organic-lean (low TOC), evaporitic siltstone facies, but also distinctly shows a fundamental difference in biomarker assemblages (and thus potentially a shift in biological sources) between the lower shales and upper siltstones. This result also emphasizes that caution should be applied when utilizing singular parameters – similar to most biomarker ratios the C_{26}/C_{25} ratio is most informative when interpreted as part of a suite of lipid biomarker proxies.

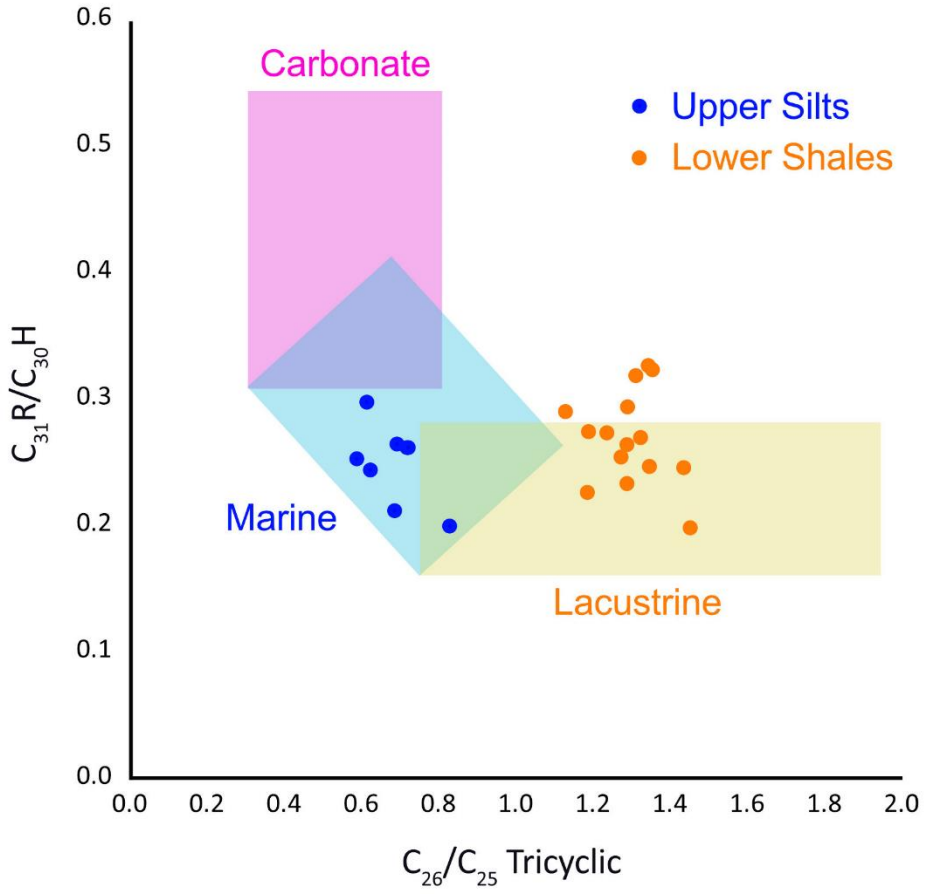

Figure 3.7: Scatterplot of the C_{26}/C_{25} tricyclic terpane ratio versus the $C_{31}HR/C_{30}H$ ratio. The orange samples to the right of the graph represent samples from the lower gray shale and black shales from both cores. The blue circles grouped to the left of the graph represent the overlaying evaporitic silts and shales. The yellow, blue, and pink shaded boxes reflect average ratio ranges from lacustrine, marine, and carbonate source environments, respectively (Peters et al., 2005). Of note, while lithology and other biomarker ratios would interpret the overlaying silts to be an evaporitic lacustrine environment, the C_{26}/C_{25} ratio falls in a typical marine zone. This seems to suggest a shift in source inputs between the lower units and the upper evaporitic zone. A cut-off empirical threshold value of 1.2 is commonly used by the petroleum industry to distinguish most lacustrine from marine settings. Hypersaline lacustrine environments are less predictable for this C_{26}/C_{25} tricyclic terpane ratio behavior, as seen for the evaporitic upper siltstones, though it is useful in this case for readily distinguishing two end-members of biomarker assemblages.

This argument for lacustrine deposition is further supported by the saline biomarker assemblage of the black shale above the fish-bearing, microlaminated layer, as well as in the upper gray shale (discussed below). This assemblage – consisting of abundant methylhopanes, gammacerane, and carotanes – is typical of those from saline alkaline lakes and therefore inconsistent with a marine depositional setting (Collister et al., 1990; Grice et al., 1998; Horsfield et al., 1994; Jiamo et al., 1990; Ruble et al., 1994; Summons et al., 2008). In total, biomarker data match with previous stratigraphic interpretations as well as the assemblages of non-marine fossils, solidifying their utility as environmental indicators.

5.2. Hydrological evolution

Our data and petrographic observations are consistent with previous interpretations of Van Houten cycles as products of rising and falling lake levels likely driven by climatic change in the Newark and Hartford basins (El Tabakh and Schreiber, 1994; Gierlowski-Kordesch and Rust, 1994; Hay et al., 1982; Kruge et al., 1990; Olsen, 1986; Olsen and Kent, 1996; Olsen et al., 1996a; Suchecki et al., 1988; Van Houten, 1962). The pedogenic features in the red siltstone indicate very shallow conditions with frequent exposure. The lower gray mudstone with decreasing grain size up section represents a deepening of the lake. Cross-bedding in this part of the section may reflect inputs of fluvial waters and thus a hydrologically open system at that time. The upper gray mudstone, where grain size coarsens upwards and that culminates in the upper red

siltstone, likely captures a return to shallow water conditions. The black shale horizon between the lower and upper gray mudstone thus represents the episode of maximum water depth (Olsen and Kent, 1996). This conclusion is supported by carbonate C-O isotope ratios, which present the black shale as a fresher (though still chemically stratified) interval bracketed by evaporitic conditions in the shallow strata below and especially evaporitic signatures in the overlaying gray shale and siltstones (found in Stüeken et al., 2019).

A more detailed picture can be obtained with the inclusion of the organic biomarkers, which indicate progressively greater contributions of halophilic organisms from the lower gray shale across the black shale and into the upper gray shale (**Fig. 3.8**). In both cores, systematic increases in the gammacerane index (from 1.08 to 3.23 in C-128 and from 1.1 to 5.5 in PT-14) were observed moving up-section through the black shale interval (though excluding the microlaminite where samples were not analysed for biomarkers). Elevated gammacerane indices are indicative of stratified water columns, though it is now known that the likely precursor molecule, tetrahymanol, is synthesized by a range of organisms (Banta et al., 2015; Damsté et al., 1995). Carotanes, β-carotane in particular, are also found in abundance between 50.84m and 49.83m of the C-128 core black shale interval as reported from other ancient saline environments (**Fig. 3.6**; **Table 3.2**; Ding et al., 2019). Carotanes are diagenetic hydrocarbon derivatives of accessory pigments from photosynthetic organisms. Increased relative production of β-carotene (the precursor of β-carotane) has been reported from both modern organisms under increasing salinity (Ben-Amotz and Avron, 1983; Borowitzka et al., 1990; Fazeli et al., 2006).

Elevated methylhopanes are commonly reported from hypersaline and alkaline lacustrine systems (Farrimond et al., 2004; French et al., 2020; Peters et al., 2005; Summons et al., 2008). The relative enrichment of the 3β/2α ratio may often, but not always, indicate the most hypersaline lacustrine environments due to a pronounced methane cycle operating within saline lakes. In the Towako formation, the 3β/2α ratio is typically only enriched within the upper parts of the black shale unit. The upper gray shale displays the most saline biomarker assemblage, including the highest gammacerane- and overall methylhopane indices. The 3β/2α ratio in these upper gray shales is depressed due to the highly elevated 2α-MeHI, rather than to low 3β-MeHI. Speculatively, 2α-MeHI values might be influenced by lake level – as the lake shallows there is more peripheral area exposed to form evaporitic crusts, as shown by the predominance of desiccation cracks. These evaporitic environments may favor cyanobacteria or other terrestrial-based microbes that can produce abundant 2-methylhopanes (Canfora et al., 2016; Oren, 2015; Ricci et al., 2014; Taher, 2014), which is also consistent with enriched $\delta^{13}C_{org}$ values (around -25‰ for the overlaying gray silts/shales versus a more depleted -30‰ baseline for the black shale units; Spiker et al., 1988; Whiteside et al., 2011). Alternatively, stratification during black shale deposition may have maintained a fresher surface water layer, influencing the relative methylhopane ratios by favoring different source organisms. Overall, these biomarker patterns suggest a progressive increase in salinity across the black shale – starting above the presumably fresher fish-bearing horizon in the microlaminite – and extending into the upper gray shale.

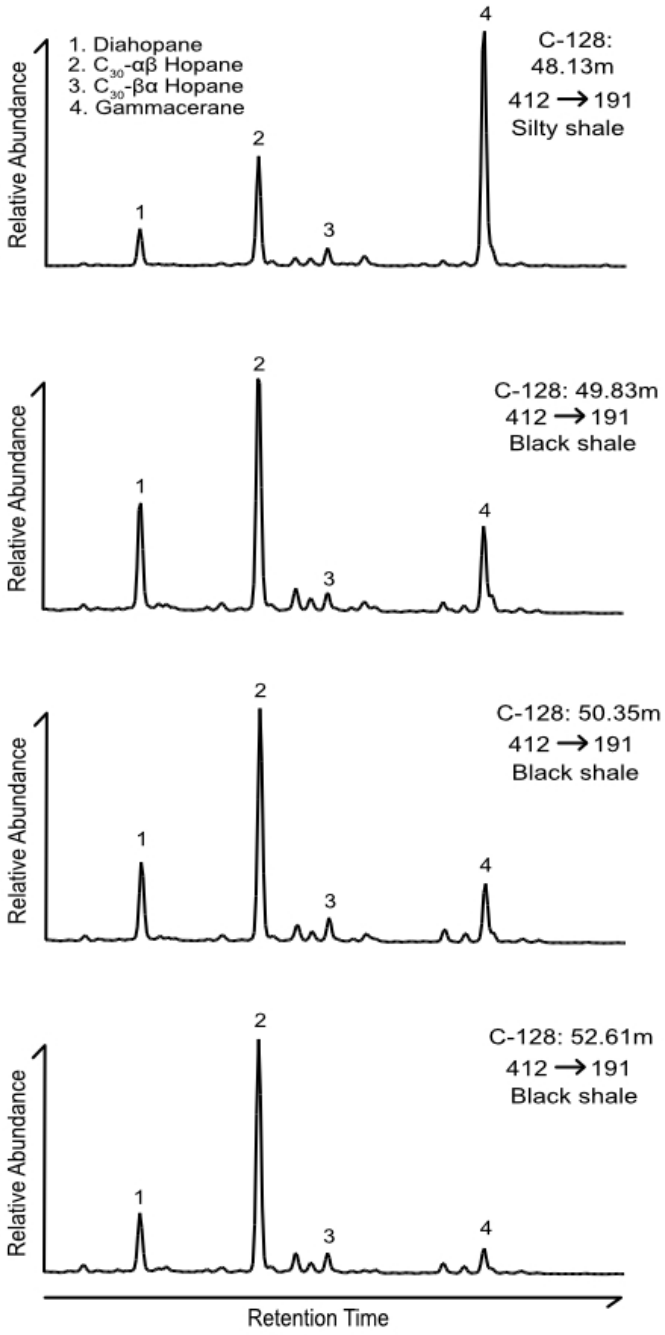

Figure 3.8: C_{30} pentacyclic triterpane patterns. MRM-GC-MS traces comparing C_{30} triterpane distributions (using the appropriate molecular-daughter ion transition of m/z 412-191 for selective detection of these polycyclic alkanes) for a series of rock bitumen extracts from the C-128 core. Compound peaks identified are: 1. C_{30} diahopane; 2. C_{30} αβ-hopane; 3. C_{30} βα-hopane (moretane); 4. gammacerane. A systematic reduction in the abundance of gammacerane (4) relative to C_{30} αβ-hopane (2) with increasing depth in the black shale interval suggests the upper portion of black shale was deposited in a more saline and likely progressively shallowing lacustrine setting. Even higher relative abundances of gammacerane are found in the silty shales of the overlaying evaporative section (see **Table 3.2**), presumably reflecting periodic hypersaline depositional conditions for this shallow water setting for the upper stratigraphic interval.

While this pattern might seem contradictory with the C-O isotope data, which suggest that the black shale interval was fresher than the intervals above and below, it is highly conceivable that these proxies capture different layers in a salinity-stratified water column. Density stratification likely began during the high-stand interval, but the carbonate C-O data could reflect the relatively fresher and better mixed surface water. In contrast, the biomarkers from this interval likely include contributions from organisms that lived in bottom waters and benthic settings that were saline and anoxic. It is unlikely that the biomarkers migrated down section into the black shale, as the overlying rocks are markedly less organic-rich. Hence the saline signature of the black shale is most likely indigenous to these rocks.

5.3. Redox evolution

Several lines of evidence suggest that bottom waters in the Newark lake became progressively more anoxic with increasing water depth and subsequent basin evolution with waning inputs and increasing evaporation. First, the decrease in bioturbation and the trend toward plane and wrinkly laminated black shale suggests that conditions may have become hostile for burrowing animals during deposition of the black shale due to low oxygen availability as well as high salinity. Anaerobic metabolisms within these ecosystems are suggested by the fairly depleted $\delta^{13}C_{org}$ values (Schidlowski, 1987; Zerkle et al., 2005). Second, the high abundance of organic carbon and the high abundances of carotanes suggests that biomass remineralization was suppressed during the deposition of

the black shale due to dynamic maintenance of very low oxygen and sulfate levels for respiration (**Fig. 3.6**). The preservation of carotanes over geologic time requires relatively reducing bottom water settings, due to the sensitivity of these molecules to rapid oxidation (Ding et al., 2019; Hebting et al., 2006). This is supported by low pristane/phytane ratios and moderate enrichments in the HHI across the lower gray and black shales, which indicates a lack of oxic degradation (Peters et al., 2005). As proposed in previous studies of other stratigraphic units in the Newark and Hartford basins, bottom-water anoxia during maximum water levels in the Van Houten cycles may have been an inevitable consequence of hydrological stagnation of the lake basin (El Tabakh and Schreiber, 1994; Kruge et al., 1990; Olsen and Kent, 1996; Suchecki et al., 1988). Saline conditions as inferred from the biomarker record starting above the microlaminite may have further suppressed the solubility of O_2 in these waters.

5.4. Evidence for elevated pH

The nitrogen isotope ratios of the Towaco Formation ($\delta^{15}N_{total}$) have probably been affected to some degree by diagenetic processes. During the degradation of biomass, in particular during the rapid degradation of peptides (Abdulla et al., 2017; Schmidt et al., 2011), nitrogen in the form of ammonium (NH_4^+) is released into pore waters. This diagenetic process is to a first order independent of redox conditions (Freudenthal et al., 2001; Schmidt et al., 2011). However, under oxic conditions, nitrification of diagenetic NH_4^+ results in a net increase in the residual $\delta^{15}N$ of biomass by a few permil magnitude (Freudenthal et al., 2001; Lehman et al., 2002). This process may largely explain the

values around +5‰ in the gray shales of the Towaco Formation. However, the spike to +15‰ in the black shale above the microlaminated fish-bearing interval is too large to be the result of diagenetic alteration alone. In fact, under anoxic conditions, as inferred from this part of the section, the diagenetic isotope effect is negligible (Freudenthal et al., 2001; Lehman et al., 2002; Robinson et al., 2012).

Such high values require processing of fixed nitrogen in the water column. In modern freshwater lakes, $\delta^{15}N_{total}$ typically falls between 0‰ and +6‰ (McLauchlan et al., 2013), and marine sediments only display higher values of up to +15‰ in upwelling zones with high degrees of denitrification, made possibly by a large supply of dissolved nitrate from the deep ocean which allows for such a signal to be preserved despite extreme nitrate loss (Tesdal et al., 2013). In lakes, however, strongly elevated $\delta^{15}N_{total}$ has only been reported from alkaline settings (Collister and Hayes, 1973; Lent et al., 1995; Menzel et al., 2013; Stüeken et al., 2015c; Talbot and Johannessen, 1992). Under high-pH conditions, diagenetically released NH_4^+ can partition into volatile NH_3 with a pKa of 9.25. This partition reaction is associated with a large isotopic fractionation of 45‰ at standard temperature, where residual NH_4^+ becomes isotopically heavier as NH_3 escapes into the atmosphere (Li et al., 2012). Preservation of the non-volatile NH_4^+, which can be re-assimilated into biomass and incorporated into clay minerals by substituting for K^+ (Müller, 1977; Schroeder and McLain, 1998), renders residual sediments isotopically heavy. The nitrogen isotope data from the Towaco Formation with $\delta^{15}N$ values up to 15‰ may thus point to strongly alkaline conditions with a pH around 9 or higher during the deposition of the black shale, such that NH_3 production was favored and $\delta^{15}N$

increased. Such high pH may have contributed to the disappearance of macrofauna and, hence, the absence of fish fossils above the microlaminite.

It is conceivable that the water column was relatively alkaline throughout the rest of the lake history, consistent with the biomarker assemblages throughout the section. However, the effect of NH_3 volatilization may only have been expressed under stratified conditions where NH_4^+ and NH_3 were able to escape nitrification and build up in the water column. This is typified in the black shale interval that is likely deeper, more stably stratified, and reducing. This scenario is exemplified by modern Mono Lake in the western U.S. (pH ~ 10), where stratification has led to accumulation of a large NH_4^+/NH_3 reservoir in bottom waters that is only released into the atmosphere during seasonal water-column overturn (Jellison et al., 1993).

This interpretation is consistent with the high ratios of total carbon over total nitrogen (hereafter C/N) in our black shale. The transformation of NH_4^+ to NH_3 during diagenesis would have led to a strong preferential loss of nitrogen from sediments relative to carbon, because uncharged NH_3 is less amenable to incorporation into clay minerals. This process can therefore explain the observed positive excursion in C/N ratios in the black shale. It is unlikely that the high C/N ratios reflect terrestrial plant biomass (which is known to have high primary C/N ratios > 30, McGroddy et al., 2004; Reich and Oleksyn, 2004), because the high C/N ratios in the Towaco Formation coincide with light $\delta^{13}C$ values, which are uncharacteristic of Jurassic flora (Whiteside et al., 2011). Most of the biomass in the black shale is thus likely to be microbial (see also Spiker et al., 1988), which typically has primary C/N ratios around 7-10 (Godfrey and Glass, 2011). The

measured excursion in C/N up to 50 therefore most likely reflects enhanced N loss from the system during alkaline NH_3 volatlilization.

The observed correlation between C/N ratios and TOC in the Towaco Formation (**Fig. 3.5B**) may be the result of greater NH_4^+ and NH_3 production under relatively more anoxic conditions. When less O_2 gets mixed into the sediments, more organic carbon can be preserved, and less NH_4^+/NH_3 gets oxidized to NO_3^-. Hence, more nitrogen could be lost as NH_3 and drive $\delta^{15}N$ of residual NH_4^+ heavy, which would then get passed on to biomass and clay minerals.

We speculate that the kinks in the slope in **Fig. 3.5A and 3.5B**, where $\delta^{15}N$ increases more strongly above C/N > 35 (**Fig. 3.5A**), and C/N ratios increase less strongly where TOC is above ~2% (**Fig. 3.5B**), reflect the establishment of thermal and/or salinity-driven stratification of the water column – similar to Mono Lake (Jellison et al., 1993). During this stratified phase, the isotopically heavy NH_4^+ may have become a more important source of fixed nitrogen for microbes in the photic zone, such that sinking biomass was already enriched in $\delta^{15}N$ prior to diagenesis, leading to higher overall $\delta^{15}N$ values in sediments.

6. Synthesis of basin evolution

The studied section of the Towaco Formation in the early Jurassic Newark basin records the deepening and shallowing of an ancient rift lake, likely driven by cyclic climatic changes (Olsen, 1986; Van Houten, 1962). As suggested by our lipid biomarker records, the lake waters likely became progressively more saline and alkaline with

increased evaporation above the microlaminated fish-bearing unit. In fact, increased salinity stratification, which would have promoted redox stratification between upper and lower water layers, was likely a major factor in enhancing organic matter preservation during deposition of the black shale interval as evidenced by high gammacerane index values and abundant carotane preservation in chromatograms. Bottom-water anoxia prevailed only during the deposition of the black shale, which probably marks an episode of stagnation and stratification as suggested for Van Houten cycles elsewhere in the basin (El Tabakh and Schreiber, 1994; Kruge et al., 1990). Together, indicators for high salinity, alkalinity and redox stratification increase above the fish-bearing horizon relative to preceding beds, suggesting that the onset of saline anoxic conditions may have made this lake uninhabitable for most animal life. These observations may be synthesized as follows:

Phase 1 – wet stage in a warm climate: During deposition of the lower gray shale, water influx exceeded loss by evaporation, such that the lake became progressively deeper. The shallow depth of the lake during this time likely allowed for wind mixing and entrainment of atmospheric oxygen into the water column, which would explain the observed ripples and the lack of authigenic iron and trace metal enrichments.

Phase 2 – climatic shift towards arid conditions: When the lake reached its maximum depth, likely marked by the microlaminite, the lake was evidently sufficiently dilute to support a rich biota that included various fish species (Olsen, 1988b; Olsen et al., 2003). During subsequent deposition of the remainder of the black shale evaporation became more important, leading to high salinity, high alkalinity and stagnation, as

indicated by the biomarkers and the preservation of undisturbed wrinkly mats on the lake floor. Saline waters sank to the bottom, beneath a fresher surface cap. Stagnation, paired with low O_2 solubility in saline waters, enhanced anoxia in deep waters. NH_3, built up in the lower anoxic alkaline water column, was released to the atmosphere during seasonal overturn – as we see in modern alkaline lakes. This process would explain the large $\delta^{15}N$ values observed in the black shale.

Phase 3 – arid climate: During deposition of the upper gray shale, aquatic salinity increased further, as suggested by the biomarker assemblages and oxygen isotope data. Evaporation exceeded inflow and the lake water level dropped. Under shallow water conditions, wind mixing extended down to the sediments, allowing for the formation of ripples and the entrainment of oxygen. Finally, deposition of the red shales marks almost complete desiccation with only seasonal or less frequent flooding.

7. Conclusions and wider implications

The hydrological evolution of the Newark Basin can be constrained by sedimentary and mineralogical features, stable isotopic ($\delta^{13}C_{org}$, $\delta^{15}N_{total}$) ratios, lipid biomarker distributions, and paleogeographic reconstructions. A diverse suite of biomarker hydrocarbons, including steranes, hopanes, other triterpanes, and carotenoids is consistent with paleontological and sedimentological constraints, which shows that biomarkers serve not only to help interpret ancient source rocks as being deposited in lacustrine versus marine settings, but also to make informative inferences about temporal shifts in water column redox and alkalinity through observations of water column

stratification and salinity. In combination with stable isotopic measurements of sedimentary organic matter, particularly $\delta^{15}N_{total}$, this represents a powerful way to recognize pH of ancient extreme systems. Within this context, diverse proxies, alone and in combination, may help us delineate and characterize ancient alkaline systems. Further, due to its geochemical recognition as an alkaline lacustrine environment, the Towako Formation can better serve as an ancient natural laboratory for assessing the effects of high pH on paleoenvironmental proxies used routinely by geochemists to track the redox evolution of Earth's surface environments across geologic time.

Acknowledgements

This work was supported at the University of California, Riverside by the NSF-EAR FESD Program and the NASA Astrobiology Institute under Cooperative Agreement No. NNA15BB03A issued through the Science Mission Directorate. We thank Roger Buick (UW) for financial support of the carbon and nitrogen isotope work. EES acknowledges support from a NASA postdoctoral fellowship, as well as valuable discussions about the Newark basin with Charlotte B. Schreiber. GDL thanks the Agouron Institute for providing funding for the Waters Autospec GC-MS instrument at UCR. We thank Dr. Wang (China University of Petroleum) for help with sampling, the Rutgers core repository for access, and Andy Robinson, Bridget Lee (UCR) and Andy Schauer (UW) for technical support.

Sample Depth	TOC	C/N	$\delta^{13}C$	$\delta^{15}N$
Core C-128				
45.48	0.4	10.68	-26.5	5.82
48.13	0.35	8.41	-26.38	5.53
48.86	0.32	7.71	-27.25	4.99
49.83	1.06	24.33	-30.1	6.57
50.08	0.92	24.27	-30.22	5.94
50.54	4.75	45.36	-29.78	12.66
50.84	6.64	45.31	-29.71	14.47
51.27	2.08	36.04	-29.65	6.2
51.54	3.46	46.66	-29.29	6.92
52.61	1.04	22.7	-30.21	5.9
53.52	0.3	7.62	-28.83	4.84
54.1	1.86	29.74	-30.44	7.29
Core PT-14				
94.82	0.29	7.31	-26.18	6.15
95.58	0.46	10.22	-26.03	7.02
95.83	0.35	11.36	-26.89	5.01
97.05	0.32	7.55	-26.89	4.92
98.04	1.35	34.08	-29.83	5.76
98.6	1.31	33.51	-29.91	6.88
99.31	4.95	47.49	-30.03	12.58
99.57	4.87	43.85	-29.84	12.31
100.08	2.73	41.79	-29.44	6.35
101.02	1.29	31.29	-30.4	6.12
102.29	0.16	3.79	-26.94	3.76

Table 3.1: Bulk geochemistry data. TOC = total organic carbon in weight percent of rock; C/N = carbon/nitrogen ratio (wt%/wt%); $\delta^{13}C_{org}$ ‰ (vs VPDB); $\delta^{15}N_{total}$ ‰ (vs AIR). Colors as in **Fig. 3.3 and 3.4**.

Sample Depth	H/S	30st%	HHI	C_{29} ααα (S/S+R)	C_{31}H (S/S+R)	C_{26}/ C_{25}	C_{33} 2αMeHI	C_{33} 3βMeHI	Gam. Index	3β /2α	C_{31}R/ C_{30}H	Pr/ Phy	Carotanes
Core C-128													
45.48	6.09	0.00	1.91	0.32	0.59	0.63	10.49	7.91	6.23	0.73	0.30		
.13	2.95	0.00	2.32	0.44	0.61	0.60	10.32	5.92	25.25	0.55	0.25	0.9	
48.86	3.64	0.00	2.16	0.46	0.58	0.84	8.79	4.24	12.18	0.46	0.20		
49.83	1.88	0.00	4.21	0.62	0.59	1.47	3.83	5.23	3.23	1.39	0.20	0.61	5.07
50.08	2.02	0.00	4.41	0.57	0.59	1.45	3.66	5.22	3.33	1.45	0.25		
50.54	2.55	0.00	3.76	0.55	0.62	1.30	2.58	5.46	2.35	2.18	0.29	0.79	3.60
50.84	2.63	0.00	3.69	0.53	0.60	1.37	2.14	4.77	2.58	2.29	0.32	0.74	29.93
51.27	7.70	0.00	4.46	0.53	0.61	1.20	5.64	3.37	1.46	0.58	0.27		
51.54	5.83	0.00	3.35	0.57	0.59	1.30	5.60	2.95	1.08	0.51	0.23	0.72	0.55
52.61	5.64	0.00	3.96	0.60	0.58	1.36	6.63	3.11	1.04	0.45	0.25	0.58	1.61
53.52	6.22	0.00	4.18	0.56	0.59	1.34	6.67	3.22	1.14	0.47	0.27		
54.1	7.08	0.00	4.06	0.49	0.59	1.29	6.02	3.12	1.13	0.50	0.25		
Core PT-14													
94.82	2.75	0.00	3.16	0.33	0.59	0.64	13.55	7.81	4.50	0.54	0.24		
95.58	6.74	0.00	0.90	0.29	0.59	0.74	8.46	8.26	5.55	0.97	0.26		
95.83	5.11	0.00	1.33	0.34	0.58	0.73	6.60	8.44	5.82	1.30	0.26		
97.05	2.85	0.00	2.81	0.56	0.59	0.70	8.34	4.07	10.66	0.47	0.21		
98.04	2.24	0.00	4.18	0.51	0.59	1.30	3.90	4.76	2.89	1.23	0.26	0.66	2.51
98.6	1.12	0.00	4.34	0.53	0.60	1.14	3.32	3.55	5.51	1.07	0.29		
99.31	4.02	0.00	3.84	0.49	0.59	1.36	3.42	5.18	1.92	1.55	0.33		
99.57	5.01	0.00	3.89	0.51	0.60	1.33	3.52	4.73	1.90	1.36	0.32		
100.08	5.76	0.00	3.36	0.54	0.59	1.25	5.00	2.82	1.13	0.55	0.27		
101.02	5.67	0.00	3.60	0.52	0.58	1.20	7.32	3.13	0.95	0.41	0.23		
102.29	0.40	0.00	5.10	0.34	0.60	0.71	15.19	0.00	0.66	0.00	0.26		

Table 3.2: Biomarker data. H/S = C_{27}-C_{35} hopanes/C_{27}-C_{29} regular steranes; 30st% = % of C_{30} steranes relative to C_{27}-C_{30} regular steranes; HHI = homohopane index (C_{35} homohopane/sum of C_{31}-C_{35} homohopanes); C_{29} ααS/(S+R) = C_{29} sterane ααS/(S+R) ratio for thermal maturity; C_{31}H S/(S+R) = C_{31} αβ hopane S/(S+R) ratio for thermal maturity; C_{26}/C_{25} = ratio of C_{26} to C_{25} tricyclic terpanes; 2α- and 3β-MeHI = percentage abundances of the particular C_{33} methylhopane relative to sum of C_{33} methylhopane and C_{32} homohopane; Gam. index = 10*(gammacerane/C_{30} αβ hopane); 3/2 MeHI = 3β-methylhopane index/2α-methylhopane index; C_{31}R/C_{30}H; pr/phy = pristane/phytane; carotanes = sum of carotane biomarkers/n-C_{21+22} alkanes. Colors as in **Fig. 3.3 and 3.4.**

References

Abdulla, H.A., Burdige, D.J. and Komada, T., 2017. Accumulation of Deaminated Peptides in Anoxic Sediments of Santa Barbara Basin. Geochimica et Cosmochimica Acta: doi: 10.1016/j.gca.2017.11.021.

Anbar, A., Duan, Y., Lyons, T.W., Arnold, G.L., Kendall, B., Creaser, R.A., Kaufman, A.J., Gordon, G.W., Scott, C.T., Garvin, J. and Buick, R., 2007. A whiff of oxygen before the Great Oxidation Event? Science, 317(5846): 1903-1906.

Banta, A.B., Wei, J.H. and Welander, P.V., 2015. A distinct pathway for tetrahymanol synthesis in bacteria. Proceedings of the National Academy of Sciences, 112(44): 13478-13483.

Ben-Amotz, A. and Avron, M., 1983. On the factors which determine massive β-carotene accumulation in the halotolerant alga Dunaliella bardawil. Plant Physiology, 72(3): 593-597.

Berner, R.A. and Raiswell, R., 1984. C/S method for distinguishing freshwater from marine sedimentary rocks. Geology, 12(6): 365-368

Blackburn, T.J., Olsen, P.E., Bowring, S.A., McLean, N.M., Kent, D.V., Puffer, J., McHone, G., Rasbury, E.T. and Et-Touhami, M., 2013. Zircon U-Pb geochronology links the end-Triassic extinction with the Central Atlantic Magmatic Province. Science, 340: 941-945.

Borowitzka, M.A., Borowitzka, L.J. and Kessly, D., 1990. Effects of salinity increase on carotenoid accumulation in the green alga Dunaliella salina. Journal of Applied Phycology, 2(2): 111-119.

Canfora, L., Vendramin, E., Vittori Antisari, L., Lo Papa, G., Dazzi, C., Benedetti, A., Iavazzo, P., Adamo, P., Jungblut, A. D., & Pinzari, F., 2016. Compartmentalization of gypsum and halite associated with cyanobacteria in saline soil crusts. FEMS Microbiology Ecology, 92.

Collister, J.W. and Hayes, J.M., 1973. A preliminary study of carbon and nitrogen isotopic biogeochemistry of lacustrine sedimentary rocks from the Green River Formation, Wyoming, Utah, and Colorado. In: M.L. Tuttle (Editor), Geochemical, biogeochemical, and sedimentological studies of the Green River formation, Wyoming, Utah, and Colorado. U.S. Geological Survey, Denver, CO.

Collister, J.W., Lichtfouse, E., Hieshima, G. and Hayes, J.M., 1990. Partial resolution of sources of n-alkanes in the saline portion of the Parachute Creek Member, Green River Formation (Piceance Creek Basin, Colorado). Organic Geochemistry, 21(6-7): 645-659.

Damsté, J.S.S., Kenig, F., Koopmans, M.P., Köster, J., Schouten, S., Hayes, J.M. and de Leeuw, J.W., 1995. Evidence for gammacerane as an indicator of water column stratification. Geochimica et Cosmochimica Acta, 59(9): 1895-1900.

De Grande, S.M.B., Aquino Neto, F.R. and Mello, M.R., 1993. Extended tricyclic terpanes in sediments and petroleums. Organic Geochemistry, 20(7): 1039-1047.

Ding, W., Hou, D., Jiang, L., Jiang, Y., & Wu, P., 2020. High abundance of carotanes in the brackish-saline lacustrine sediments: A possible cyanobacteria source? International Journal of Coal Geology, 219: 103373.

El Tabakh, M. and Schreiber, B.C., 1994. Lithologies and diagenesis of the lacustrine sediments of the Lockatong Formation (Upper Triassic) in the Newark rift basin. In: A.J. Lomando, B.C. Schreiber and P.M. Harris (Editors), Lacustrine reservoirs and depositional systems. Society for Sedimentary Geology, Denver, Colorado, pp. 239-295.

Farrimond, P., Talbot, H. M., Watson, D. F., Schulz, L. K., & Wilhelms, A., 2004. Methylhopanoids: Molecular indicators of ancient bacteria and a petroleum correlation tool. Geochimica et Cosmochimica Acta, 68: 3873–3882.

Fazeli, M.R., Tofighi, H., Samadi, N. and Jamalifar, H., 2006. Effects of salinity on β-carotene production by Dunaliella tertiolecta DCCBC26 isolated from the Urmia salt lake, north of Iran. Bioresource Technology, 97(18): 2453-2456.

French, K. L., Birdwell, J. E., and Berg, M. V., 2020. Biomarker similarities between the saline lacustrine Eocene Green River and the Paleoproterozoic Barney Creek Formations. Geochimica et Cosmochimica Acta, 274: 228–245.

Freudenthal, T., Wagner, T., Wenzhoefer, F., Zabel, M. and Wefer, G., 2001. Early diagenesis of organic matter from sediments of the eastern subtropical Atlantic: evidence from stable nitrogen and carbon isotopes. Geochimica et Cosmochimica Acta, 65(11): 1795-1808.

Gierlowski-Kordesch, E. and Rust, B.R., 1994. The Jurassic East Berlin Formation, Hartford Basin, Newark Supergroup (Connecticut and Massachusetts): A Saline Lake Playa Alluvial Plain System. Sedimentology and Geochemistry of Modern and Ancient Saline Lakes, SEPM Special Publication, 50: 249-265.

Godfrey, L.V. and Glass, J.B., 2011. The geochemical record of the ancient nitrogen cycle, nitrogen isotopes, and metal cofactors. Methods in Enzymology, 486: 483-506.

Gold, D.A., Grabenstatter, J., de Mendoza, A., Riesgo, A., Ruiz-Trillo, I. and Summons, R.E., 2016. Sterol and genomic analyses validate the sponge biomarker

hypothesis. Proceedings of the National Academy of Sciences, 113(10): 2684-2689.

Grice, K., Schouten, S., Peters, K.E. and Damsté, J.S.S., 1998. Molecular isotopic characterisation of hydrocarbon biomarkers in Palaeocene–Eocene evaporitic, lacustrine source rocks from the Jianghan Basin, China. Organic Geochemistry, 29(5): 1745-1764.

Halevy, I. and Bachan, A., 2017. The geologic history of seawater pH. Science, 355: 1069-1071.

Hardisty, D.S., Lu, Z., Bekker, A., Diamond, C.W., Gill, B.C., Jiang, G., Kah, L.C., Knoll, A.H., Loyd, S.J., Osburn, M.R. and Planavsky, N.J., 2017. Perspectives on Proterozoic surface ocean redox from iodine contents in ancient and recent carbonate. Earth and Planetary Science Letters, 463: 159-170.

Hatcher, P.G. and Romankiw, L.A., 1985. Nuclear magnetic resonance studies of organic-matter-rich sedimentary rocks of some early Mesozoic basins of the eastern United States. In: G.R. Robinson and A.J. Froelich (Editors), Proceedings of the second US Geological Survey workshop in the early Mesozoic basins of the eastern United States, pp. 65-70.

Hay, W.W., Behensky Jr, J.F., Barron, E.J. and Sloan II., J.L., 1982. Late Triassic-Liassic Paleoclimatology of the proto-central North Atlantic rift system. Paleogeography, Paleoclimatology, Palaeoecology, 40: 13-30.

Hebting, Y., Schaeffer, P., Behrens, A., Adam, P., Schmitt, G., Schneckenburger, P., Bernasconi, S.M. and Albrecht, P., 2006. Biomarker evidence for a major preservation pathway of sedimentary organic carbon. Science, 312(5780): 1627-1631.

Helz, G.R., Bura-Nakic, E., Mikac, N. and Ciglenecki, I., 2011. New model for molybdenum behavior in euxinic waters. Chemical Geology, 284: 323-332.

Horsfield, B., Curry, D.J., Bohacs, K., Littke, R., Rullkötter, J., Schenk, H.J., Radke, M., Schaefer, R.G., Carroll, A.R., Isaksen, G. and Witte, E.G., 1994. Organic geochemistry of freshwater and alkaline lacustrine sediments in the Green River Formation of the Washakie Basin, Wyoming, USA. Organic Geochemistry, 22(3-5): 415-440.

Isson, T.T. and Planavsky, N.J., 2018. Reverse weathering as a long-term stabilizer of marine pH and planetary climate. Nature, 560(7719): 471-475.

Jellison, R., Miller, L.G., Melack, J.M. and Dana, G.L., 1993. Meromixis in hypersaline Mono Lake, California. II: Nitrogen fluxes. Limnology and Oceanography, 38(5): 1020-1039.

Jiamo, F., Guoying, S., Jiayou, X., Eglinton, G., Gowar, A.P., Rongfen, J., Shanfa, F. and Pingan, P., 1990. Application of biological markers in the assessment of paleoenvironments of Chinese non-marine sediments. Organic Geochemistry, 16(4-6): 769-779.

Kent, D.V. and Tauxe, L., 2005. Corrected Late Triassic latitudes for continents adjacent to the North Atlantic. Science, 307(5707): 240-244.

Kruge, M.A., Hubert, J.F., Bensley, D.F., Crelling, J.C., Akes, R.J. and Meriney, P.E., 1990. Organic geochemistry of a Lower Jurassic synrift lacustrine sequence, Hartford basin, Connecticut, USA. Advances in Organic Geochemistry, 16(4-6): 689-701.

Lehman, M.R., Bernasconi, S.M., Barbieri, A. and McKenzie, J.A., 2002. Preservation of organic matter and alteration of its carbon and nitrogen isotope composition during simulated and in situ early sedimentary diagenesis. Geochimica et Cosmochimica Acta, 66(20): 3573-3584.

Lent, R.M., Lyons, W.B., Showers, W.J. and Johannesson, K.H., 1995. Late Holocene paleoclimatic and paleobiologic records from sediments of Devils Lake, North Dakota. Journal of Paleolimnology, 13(3): 193-207.

Li, L., Sherwood Lollar, B., Li, H., Wortmann, U.G. and Lacrampe-Couloume, G., 2012. Ammonium stability and nitrogen isotope fractionations for NH_4^+-$NH_{3(aq)}$-$NH_{3(gas)}$ systems at 20-70^{o}C and pH of 2-13: applications to habitability and nitrogen cycling in low-temperature hydrothermal systems. Geochimica et Cosmochimica Acta, 84: 280-296.

Lyons, T. W., Reinhard, C. T., and Planavsky, N.J., 2014. The rise of oxygen in Earth's early ocean and atmosphere. Nature, 506(7488): 307–315.

Malinconico, M.A., 2002. Lacustrine organic sedimentation, organic metamorphism and thermal history of selected Early Mesozoic Newark Supergroup basins, Columbia University, New York, 419 pp.

McGroddy, M.E., Daufresne, T. and Hedin, L.O., 2004. Scaling of C: N: P stoichiometry in forests worldwide: Implications of terrestrial redfield-type ratios. Ecology, 85(9): 2390-2401.

McLauchlan, K.K., Williams, J.J., Craine, J.M. and Jeffers, E.S., 2013. Changes in global nitrogen cycling during the Holocene epoch. Nature, 495(7441): 352-355.

Menzel, P., Gaye, B., Wiesner, M.G., Prasad, S., Stebich, M., Krishna Das, B., Anoop, A., Riedel, N. and Basavaiah, N., 2013. Influence of bottom water anoxia on nitroen isotopic ratios and amino acid contributions of recent sediments from small eutrophic Lonar Lake, central India. Limnology and Oceanography, 58(3): 1061-1074.

Moldowan, J.M., Fago, F.J., Lee, C.Y., Jacobson, S.R., Watt, D.S., Slougui, N.-E., Jeganathan, A. and Young, D.C., 1990. Sedimentary 24-n-propylcholestanes, molecular fossils diagnostic of marine algae. Science, 247: 309-312.

Morgan, B. and Lahav, O., 2007. The effect of pH on the kinetics of spontaneous Fe(II) oxidation by O_2 in aqueous solution–basic principles and a simple heuristic description. Chemosphere, 68(11): 2080-2084.

Müller, P.J., 1977. CN ratios in Pacific deep-sea sediments: Effect of inorganic ammonium and organic nitrogen compounds sorbed by clays. Geochimica et Cosmochimica Acta, 41(6): 765-776.

Olsen, P.E., 1986. A 40-million-year lake record of early Mesozoic climatic forcing. Science, 234(842-848).

Olsen, P.E., 1988a. Continuity of strata in the Newark and Hartford Basins of the Newark Supergroup. U.S. Geological Survey Bulletin, 1776: 6-18.

Olsen, P.E., 1988b. Paleoecology and paleoenvironments of the continental early Mesozoic Newark Supergroup of eastern North America. In: W. Manspeizer (Editor), Triassic-Jurassic rifting and the openning of the Atlantic ocean. Elsevier, Amsterdam, pp. 185-230.

Olsen, P.E., 1990. Tectonic, climatic, and biotic modulation of lacustrine ecosystems: examples from the Newark Supergroup of eastern North America. In: B. Katz (Editor), Lacustrine Basin Exploration: Case Studies and Modern Analogs. American Association Petroleum Geologists Memoir American Association Petroleum Geologists, pp. 209-224.

Olsen, P.E., 1997. Stratigraphic record of the early Mesozoic breakup of Pangea in the Laurasia-Gondwana rift system. Annual Reviews in Earth and Planetary Sciences, 25: 337-401.

Olsen, P.E., 2011. Fossil Great Lakes of the Newark Supergroup – 30 Years Later. In: A.I. Benimoff (Editor), Field Trip Guidebook. New York State Geological Association, New York, pp. 101-162.

Olsen, P.E., 2012. Air-fall ashes of the CAMP from eastern North America and Morocco, GSA Northeastern Section, annual meeting. Geological Society of America, Hartford, Connecticut, pp. 56.

Olsen, P.E. and Kent, D.V., 1996. Milankovitch climate forcing in the tropics of Pangaea during the Late Triassic. Paleogeography, Paleoclimatology, Palaeoecology, 122: 1-26.

Olsen, P.E., Kent, D.V., Cornet, B., Witte, W.K. and Schlische, R.W., 1996a. High-resolution stratigraphy of the Newark rift basin (early Mesozoic, eastern North America). Geological Society of America Bulletin, 108(1): 40-77.

Olsen, P.E., Schlische, R.W. and Fedosh, M.S., 1996b. 580 kyr duration of the Early Jurassic flood basalt event in eastern North America estimated using Milankovitch cyclostratigraphy. In: M. Morales (Editor), The continental Jurassic. Museum of Northern Arizona Bulletin, pp. 11-22.

Olsen, P.E., Whiteside, J.H. and Huber, P., 2003. Causes and consequences of the Triassic-Jurassic mass extinction as seen from the Hartford basin. In: J.B. Brady and J.T. Cheney (Editors), Guidebook for Field Trips in the Five College Region. 95th New England Intercollegiate Geological Conference, Department of Geology, Smith College, Northampton, Massachusetts, pp. 1-41.

Oren, A., 2015. Cyanobacteria in hypersaline environments: Biodiversity and physiological properties. Biodiversity and Conservation, 24: 781–798.

Partin, C.A., Bekker, A., Planavsky, N.J. and Lyons, T.W., 2015. Euxinic conditions recorded in the ca. 1.93 Ga Bravo Lake Formation, Nunavut (Canada): Implications for oceanic redox evolution. Chemical Geology, 417: 148-162.

Peters, K. E., Walters, C. C., & Moldowan, J. M. (2005). The biomarker guide (Vol. 2). Cambridge University Press.

Pratt, L.M., 1989. Deposition, diagenesis, and maturation of organic matter in rift-basin lacustrine shales of Triassic-Jurassic Newark Supergroup, AAPG annual convention. American Association of Petroleum Geology, San Antonio, Texas, pp. CONF-890404.

Pratt, L.M., Vuletich, A.K. and Daws, T.A., 1985. Geochemical and isotopic characterization of organic matter in rocks of the Newark Supergroup. In: G.R. Robinson and A.J. Froelich (Editors), Proceedings of the second US Geological Survey workshop on the early Mesozoic basins of the eastern United States. US Geological Survey, pp. 74-78.

Reich, P.B. and Oleksyn, J., 2004. Global patterns of plant leaf N and P in relation to temperature and latitude. Proceedings of the National Academy of Sciences, 101(30): 11001-11006.

Ricci, J. N., Coleman, M. L., Welander, P. V., Sessions, A. L., Summons, R. E., Spear, J. R., & Newman, D. K., 2014. Diverse capacity for 2-methylhopanoid production correlates with a specific ecological niche. The ISME Journal, 8: 675–684.

Robinson, R.S., Kienast, M., Albuquerque, A.L., Altabet, M., Contreras, S., De Pol Holz, R., Dubois, N., Francois, R., Galbraith, E., Shu, T.-C., Ivanochko, T., Jaccard, S., Kao, S.-J., Kiefer, T., Kienast, S., Lehmann, M., Martinez, P., McCarthy, M., Moebius, J., Pedersen, T., Quan, T.M., Ryabenko, E., Schmittner, A., Schneider, R., Schneider-Mor, A., Shigemitsu, M., Sinclair, D., Somes, C., Studer, A., Thunell, R. and Yang, J.-Y., 2012. A review of nitrogen isotopic alteration in marine sediments. Paleoceanography, 27(PA4203): doi: 10.1029/2012PA002321.

Rohrssen, M., Love, G.D., Fischer, W., Finnegan, S. and Fike, D.A., 2013. Lipid biomarkers record fundamental changes in the microbial community structure of tropical seas during the Late Ordovician Hirnantian glaciation. Geology, 41: 127-130.

Ruble, T.E., Bakel, A.J. and Philp, R.P., 1994. Compound specific isotopic variability in Uinta Basin native bitumens: paleoenvironmental implications. Organic Geochemistry, 21(6-7): 661-671.

Schidlowski, M., 1987. Application of stable carbon isotopes to early biochemical evolution on Earth. Annual Review of Earth and Planetary Sciences, 15: 47-72.

Schlische, R.W., 1990. Structural and stratigraphic development of the Newark extensional basin, eastern North America; evidence for the growth of the basin and its bounding structures. Geological Society of America Bulletin, 104: 1246-1263.

Schmidt, F., Koch, B.P., Elvert, M., Schmidt, G., Witt, M. and Hinrichs, K.U., 2011. Diagenetic transformation of dissolved organic nitrogen compounds under contrasting sedimentary redox conditions in the Black Sea. Environmental Science & Technology, 45(12): 5223-5229.

Schroeder, P.A. and McLain, A.A., 1998. Illite-smectites and the influence of burial diagenesis on the geochemical cycling of nitrogen. Clay Minerals, 33(4): 539-546.

Scott, C., Lyons, T.W., Bekker, A., Shen, Y., Poulton, S.W., Chu, X. and Anbar, A.D., 2008. Tracing the stepwise oxygenation of the Proterozoic ocean. Nature, 452: 456-459.

Smoot, J.P. and Olsen, P.E., 1994. Climatic cycles as sedimentary controls of rift basin lacustrine deposits in the early Mesozoic Newark basin based on continuous core. In: A.J. Lomando and M. Harris (Editors), Lacustrine Depositional Systems. SEPM Core Workshop Notes, pp. 201-237.

Sperling, E.A., Wolock, C.J., Morgan, A.S., Gill, B.C., Kunzmann, M., Halverson, G.P., Macdonald, F.A., Knoll, A.H. and Johnston, D.T., 2015. Statistical analysis of iron geochemical data suggests limited late Proterozoic oxygenation. Nature, 523: 451-454.

Spiker, E.C., Kotra, R.K., Hatcher, P.G., Goffried, R.M., Horan, M.F. and Olsen, P.E., 1988. Source of kerogen in black shales from the Hartford and Newark basins, eastern United States. In: A.J. Froelich and G.R. Robinson (Editors), Studies of the Early Mesozoic Basins of the Eastern United States: A Summary of Current Research on Early Mesozoic Sedimentary and Igneous Rocks and Related Mineral Resources. US Geological Survey Bulletin. US Geological Survey, pp. 63-68.

Stüeken, E.E., Buick, R. and Anbar, A.D., 2015a. Selenium isotopes support free O_2 in the latest Archean. Geology, 43(3): 259-262.

Stüeken, E.E., Buick, R., Guy, B.M. and Koehler, M.C., 2015b. Isotopic evidence for biological nitrogen fixation by Mo-nitrogenase at 3.2 Gyr. Nature, 520: 666-669.

Stüeken, E.E., Buick, R. and Schauer, A.J., 2015c. Nitrogen isotope evidence for alkaline lakes on late Archean continents. Earth and Planetary Science Letters, 411: 1-10.

Stüeken, E.E., Martinez, A., Love, G., Olsen, P.E., Bates, S., and Lyons, T.W., 2019, Effects of pH on redox proxies in a Jurassic rift lake: Implications for interpreting environmental records in deep time: Geochimica et Cosmochimica Acta, 252: 240–267.

Suchecki, R.K., Hubert, J.F. and Birney de Wet, C.C., 1988. Isotopic imprint of climate and hydrogeochemistry on terrestrial strata of the Triassic-Liassic Hartford and Fundy rift basins. Journal of Sedimentary Petrology, 58(5): 801-811.

Summons, R.E., Hope, J.M., Swart, R. and Walter, M.R., 2008. Origin of Nama Basin bitumen seeps: Petroleum derived from a Permian lacustrine source rock traversing southwestern Gondwana. Organic Geochemistry, 39(5): 589-607.

Tack, F.M., Callewaert, O.W.J.J. and Verloo, M.G., 1996. Metal solubility as a function of pH in a contaminated, dredged sediment affected by oxidation. Environmental Pollution, 91(2): 199-208.

Taher, A. G., 2014. Microbially induced sedimentary structures in evaporite-siliciclastic sediments of Ras Gemsa sabkha, Red Sea Coast, Egypt. Journal of Advanced Research, 5: 577–586.

Van Houten, F.B., 1962. Cyclic sedimentation and the origin of analcime-rich upper Triassic Lockatong Formation, west-central New Jersey adn adjacent Pennsylvania. American Journal of Science, 260: 561-571.

Talbot, H. M., & Farrimond, P., 2007. Bacterial populations recorded in diverse sedimentary biohopanoid distributions. Organic Geochemistry, 38: 1212–1225.

Talbot, M.R. and Johannessen, T., 1992. A high resolution palaeoclimatic record for the last 27,500 years in tropical west Africa from the carbon and nitroen isotopic composition of lacustrine organic matter. Earth and Planetary Science Letters, 110: 23-37.

Tesdal, J.E., Galbraith, E.D. and Kienast, M., 2013. Nitrogen isotopes in bulk marine sediment: linking seafloor observations with subseafloor records. Biogeosciences, 10(1): 101-118.

Tissot, B. P., and Welte, D.H., 1984. Petroleum Formation and Occurrence. Springer-Verlag, New York.

Weems, R.E. and Olsen, P.E., 1997. Synthesis and revision of groups within the Newark Supergroup. Geological Society of America Bulletin, 109: 195-209.

Whiteside, J.H., Olsen, P.E., Eglinton, T.I., Cornet, B., McDonald, N. and Huber, P., 2011. Pangean great lake paleoecology on the cusp of the end-Triassic extinction. Paleogeography, Paleoclimatology, Palaeoecology, 301: 1-17.

Whiteside, J.H., Olsen, P.E., Kent, D.V., Fowell, S.J. and Et-Touhami, M., 2007. Synchrony between the CAMP and the Triassic-Jurassic mass-extinction event? Palaeogeography, Palaeoclimatology, and Palaeoecology, 244(1-4): 345-367.

Witte, W.K., Kent, D.V. and Olsen, P.E., 1991. Magnetostratigraphy and paleomagnetic poles from Late Triassic-earliest Jurassic strata of the Newark basin. Geological Society of America Bulletin, 103: 1648-1662.

Zerkle, A., House, C.H. and Brantley, S.L., 2005. Biogeochemical signatures through time as inferred from whole microbial genomes. American Journal of Science, 305: 467-502.

Zerkle, A.L., Poulton, S.W., Newton, R.J., Mettam, C., Claire, M.W., Bekker, A. and Junium, C.K., 2017. Onset of the aerobic nitrogen cycle during the Great Oxidation Event. Nature, 542: 465-467.

Zumberge, J. E., 1987 Prediction of Source Rock Characteristics Based on Terpane Biomarkers in Crude Oils: A Multivariate Statistical Approach. Geochimica et Cosmochimica Acta, 51: 1625–1637.

.

CHAPTER FOUR

Nearshore Terrestrial Runoff and its Contribution to Marine Sedimentary Organic Matter in the Early-Middle Eocene Norwegian-Greenland Sea

Aaron M. Martinez, Sandra Kirtland Turner, Gordon D. Love

Abstract

The early-middle Eocene epoch (~50-47 Ma) is well known for both the end of the Early Eocene Climactic Optimum and regular short-lived hyperthermal climactic perturbations. At the same time, geographical restriction of the Arctic, as well as an enhanced hydrological cycle, supported the development of a surficial freshwater 'lid'. This lid facilitated intermittent blooms of the aquatic fern, *Azolla*, which has been speculated to play a significant role in the Eocene carbon cycle. In an attempt to discern the timing, magnitude, and relationship between early-middle Eocene hyperthermal and fern bloom events, we obtained high resolution core material collected by ODP Leg 151, Site 913B off the coast of Greenland. Palynology at this site also indicates *in situ Azolla* growth but at a more typical marine high latitude locality. Despite the appreciable total organic carbon (TOC) values, Rock-Eval pyrolysis indicates that most preserved sedimentary organic matter is likely terrigenous in nature, deriving from oxidized soils and inert kerogen. Individual lipid biomarker characteristics and compound distributions are complex. Lipid biomarker analysis reveals one end-member source contribution from immature terrestrial organic matter characterized by abundant hopanoids, diterpenoids,

and triterpenoids of varying magnitude emplaced on a baseline marine lipid signal. Ratios of angiosperm to gymnosperm plant inputs, as gauged from terpenoid biomarker distributions, indicate a shift from gymnosperm to angiosperm abundance up-core. Although there is a detectable signal of *Azolla* massulae, comparisons between extant *Azolla* lipids and Site 913B sediments provide no evidence that *Azolla* contributed strongly to organic matter deposition here. Early-middle Eocene sediments from Site 913B appear to record a dynamic nearshore system with periods of strong terrigenous input potentially influenced by orbitally-forced hydrological cycles, thus making correlation to the global carbon cycle difficult. Additionally, a high source contribution from a latent pool of recalcitrant kerogen to the overall sedimentary organic matter was also recognized, which may represent highly reworked or oxidized plant material. Continuous deposition of largely inert, terrigenous organic matter suggests a mechanism for carbon sequestration in the warm and wet Eocene polar regions. However, the short-term oxidation and remineralization of this terrigenous organic matter may have been a net source of ^{13}C-depleted carbon dioxide to the atmosphere and ocean rather than a sink.

1. Introduction

Anthropogenic perturbation of the carbon cycle has had a profound and unintended effect on climate. Namely, the pumping of greenhouse gases (such as CO_2) into the atmosphere has the consequence of global warming. Now, as our planet transitions into a warmer phase, it is becoming imperative to understand the links and mechanisms behind the global carbon cycle and climate throughout Earth's history.

Sediments dating from the early Cenozoic greenhouse period provide an ideal natural laboratory to observe the interactions between global warming and cooling feedbacks.

Early Cenozoic climates were significantly different from the modern icehouse regime. This ancient "ice-free" world of the Paleocene-Eocene is known as a time of increased warmth, with minimum pCO_2 estimates reaching around 1125 p.p.m.v. (though generally thought to be over 2000 p.p.m.v.; Zachos et al., 2008; van Kempen et al., 2016). Furthermore, short-lived warming events, or hyperthermals, were characteristic features of the global climate (Zachos et al., 2010). The greatest in magnitude of these is the Paleocene-Eocene Thermal Maximum (PETM, ~56 Ma), which records global warming of up to 5° C. However, many significant hyperthermals occur in series throughout the Eocene record (Kirtland Turner et al., 2014). These hyperthermals have been linked to various mechanisms for oxidative release of carbon to the atmosphere (ie.: volcanism, collapse of methane hydrates, respiration of organic matter; Lunt et al., 2011; Sexton et al., 2011), and constitute a time of naturally-forced climatic perturbation.

Co-eval with instability in the climate and global carbon cycles, the early-middle Eocene epoch (~50-47 Ma) is marked by massive blooms of the extant freshwater fern, *Azolla*, which occurred intermittently in surface waters of the polar ocean (Brinkhaus et al., 2006). Particular oceanographic conditions would have been necessary to sustain these blooms—namely, restriction between the Arctic and surrounding ocean basins and a freshwater surface 'lid' overlaying a stratified water column—and should have made the seafloor highly conducive to the preservation of large quantities of organic matter (Speelman et al., 2009b; van Kempen et al., 2012). Drawdown and sequestration of large

quantities of organic matter could produce sizable perturbations in the global carbon cycle (Speelman et al., 2009b). Despite their potential overlap, the relative timing between global climate variability (i.e. hyperthermals) and episodic *Azolla* blooms remains to be accurately characterized (Speelman, 2010).

To investigate a possible connection between high resolution hyperthermal climactic and environmental records to *Azolla* bloom events, we obtained core samples from Ocean Drilling Program Leg 151 Site 913B in the Norwegian-Greenland Sea (September 1993; Myhre et al., 1995a). Brinkhaus et al. (2006) notes that this core captures *in situ Azolla* growth during the early-middle Eocene period (though *Azolla* counts are an order of magnitude lower than the Arctic basin proper cores). These findings have been corroborated by further palynological studies (Eldrett et al., 2009; Barke et al., 2012). Site 913B boasts the most complete high-latitude record of the Eocene-Oligocene period and possesses a strong magnetostratigraphic record with abundant age-diagnostic dinocyst biostratigraphic markers that firmly tie this locality into the global geomagnetic polarity timescale (Eldrett et al., 2004; Eldrett et al., 2009; Inglis et al., 2015). Due to the relative abundance of *Azolla* spores with viable magneto- and biostratigraphic constraints, it has been speculated that Site 913B has potential to be chemostratigraphically correlated to the global carbon cycle (Speelman, 2010; Barke et al., 2012). Recent work has compiled bulk organic and lipid biomarker data over an expanded temporal range from Site 913B (~50 – 33 Ma; Inglis et al., 2020) however, no previous high resolution chemostratigraphy has attempted to explore the early-middle Eocene carbon cycle in detail. We aimed then to discover the major biogenic source

inputs of early-middle Eocene organic matter at site 913B: could this organic matter be largely attributed to *Azolla* blooms or was derived from other terrestrial or marine organic sources? Knowing more about the molecular composition and biogenic sources, and their temporal variability, of Site 913B organic matter, permits new insights into the effect of sedimentary organic matter contributions to both local and global carbon cycles during the early-middle Eocene.

2. Sample location and history

During the early-middle Eocene, the polar Norwegian-Greenland Sea consisted of several sequestered sub-basins more or less restricted from both the Atlantic Ocean to the south by the Greenland – Faroe Ridge and from the Arctic Ocean to the north, except for a shallow surficial seawater exchange (Nilsen, 1983; Eldholm and Thomas, 1993; Radionova and Khokhlova, 2000; Akhmetiev and Beniamovski, 2009; Roberts et al., 2009). Climactic conditions were generally warm, with polar sea surface temperatures in the broad range of 10-20°C (Brinkhaus et al., 2006; Stein et al., 2014). Warm climates led to a low latitudinal temperature gradient and associated increases in polar precipitation (Zachos et al., 2001; Eldrett et al., 2009; Speelman et al., 2010; Inglis et al., 2015). These geographical conditions may have favored brackish surface water development in the Norwegian – Greenland Sea, as shown with calculated fish apatite salinities in the low 20 ppt range (possibly as low as 10 ppt) for the early-middle Eocene range sediments (Andreasson et al., 1996). Salinity stratification and lack of mixing may have led to low-oxygen bottom waters, which has been used to interpret the relatively

enriched total organic carbon (TOC) contents preserved in sediments (Thiede et al., 1995; Andreasson et al., 1996). While pollen and cysts are sporadically abundant (Eldrett et al., 2009), the apparent lack of calcareous microfossils has been attributed to either depth of deposition below the carbonate compensation depth (CCD; Myhre et al., 1995) or stratification leading to more acidic bottom waters (Andreasson et al., 1996).

ODP Leg 151 site 913B was drilled in September 1993 in the Norwegian – Greenland Sea to a total depth of 770 mbsf (**Fig. 4.1;** Thiede et al., 1995). Site 913B is the most complete Arctic high-latitude record of the Eocene-Oligocene period and possesses a strong magnetostratigraphic record with age-diagnostic dinocyst biostratigraphic markers that firmly tie this locality into the global geomagnetic polarity timescale (Eldrett et al., 2004; Eldrett et al., 2009; Inglis et al., 2020). For this paper, our absolute dates for sedimentary deposition follow the age model put forth in Inglis et al. (2020). The core consists of four lithologic units, with unit IV encompassing the early-middle Eocene of interest here. Samples come from early-middle Eocene 913B sediments of unit IV from 685 – 717 mbsf at ~20 cm-scale resolution (48.29 – 50.21 Ma; ~10 kyr resolution, minus core recovery gaps). These sediments consist of laminated clays, massive silty clays, and clayey, silty muds in fining upward sequences, with scattered coal fragments (mm – cm scale) occurring in the massive units below 702 mbsf (Thiede et al., 1995). Occasional slump structures are recognized. Deposition of the lower massive, poorly sorted deposits (and coal fragments) likely occurred due to short distance mud flows or turbidity currents and suggest proximity to the coast (Myhre et al., 1995). These sediments have been noted to show notable terrestrial influence and were possibly

very nearshore, though the overall water paleodepth is hard to establish (Waddell and Moore, 2008). Sediments were probably sourced from the eastern edge of Greenland, which was free of glaciers during that time (Thiede et al., 1995; Andreasson et al., 1996; Eldrett et al., 2007). The proportions of finer sediments increase up-section and are inferred to represent a gradual shift to less energetic conditions possibly due to a change in sediment source, shift in sedimentary depocenter, or sea level rise (Myhre et al., 1995).

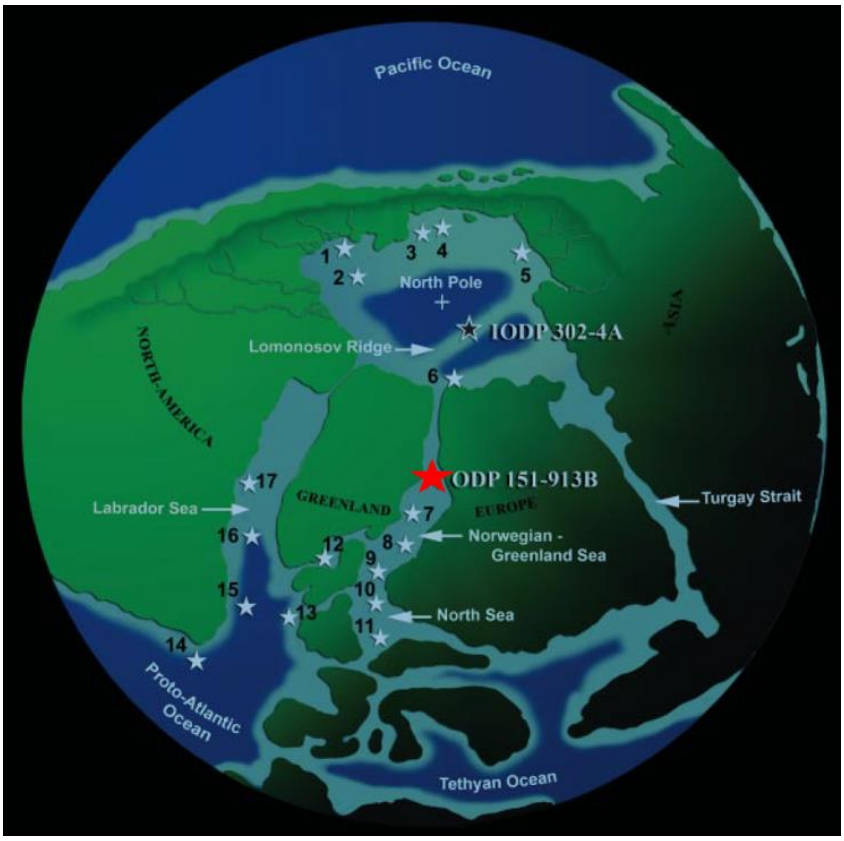

Figure 4.1: Early-middle Eocene paleogeography. Relative drill site of ODP Expedition 151 Site 913B is labeled as a red star. The proto Norwegian-Greenland Sea was an ice-free and relatively restricted basin. Figure modified from Brinkhaus et al. (2006).

3. Methods

3.1. Bulk organic geochemistry

Bulk sediment samples for organic geochemistry were crushed in a pre-fired (500°C) ceramic mortar and pestle. 0.5 g of this crushed powder was decalcified with 1 N HCl at 60°C overnight (or until no further reaction was observed). Samples were rinsed to a neutral pH with Milli-Q ultrapure water, then placed in a 100°C drying oven for an hour and further drying overnight. Weight percent carbonate mineral content was estimated based on overall weight loss from this process. The residues were weighed into tin capsules and combusted on a Costech elemental combustion system (EA) coupled to a Delta V isotope ratio mass spectrometer (IRMS). Total organic carbon (due to loss of carbonate) and total nitrogen contents, as well as bulk sedimentary $\delta^{13}C$, were determined by comparison of resulting peak areas to a suite of standards including acetanilide, glycine, and two homogenized house shales. Stable isotope results for 12/13C are reported as $\delta^{13}C$ relative to VPDB in permil (‰). The reported standard deviation for all carbon isotope measurements is ±0.1‰. To verify independent inter-lab reproducibility, a subset of samples were sent to GeoMark Research for TOC analysis by LECO C230 and bulk $\delta^{13}C$ determinations using an Elementar Isotope Select Cube elemental analyzer (EA) coupled to a VisION isotope ratio mass spectrometer (IRMS) calibrated against certified international standards (USGS24 and NBS22).

3.2. Rock-Eval pyrolysis

To determine hydrocarbon production parameters within 913B sediments, approximately 100 milligrams of washed, ground (60 mesh) bulk sediment sample were analyzed with either a Rock-Eval II or HAWK instrument at GeoMark Research. Measurements include S1: free bitumen content (mg HC/g rock); S2: remaining generation potential (mg HC/g rock); Tmax: temperature at maximum evolution of S2 hydrocarbons (°C); and S3: organic carbon dioxide yield (mg CO_2/g rock), and were generated by heating according to the following parameters S1: 300°C for 3 minutes; S2: 300°C to 550°C at 25°C/min, held at 550°C for 1 minute; S3: trapped between 300 to 390°. Instrument calibration was achieved using a rock standard with values determined from a calibration curve to pure hydrocarbons of varying concentrations. This standard was analyzed every 10 samples as an unknown to check the instrument calibration.

3.3. Site 913B lipid biomarker extraction

Selected samples were processed for lipid biomarker analysis. Due to mass limitations on sedimentary material, samples were screened first by abundance of TOC or the pre-recorded presence of *Azolla* spores. Some samples with low TOC (as in the more sandy material) were also analyzed in an attempt to lessen selection bias. Crushed sediment powders (typically 5 g) were placed in a mix of 9:1 DCM/MeOH and heated in a CEM Microwave Accelerated Reaction System (MARS) to extract the bitumen phase of organic matter as a total lipid extract (TLE). Once extracted, TLEs were filtered to remove suspended sediments. TLE was then evaporated to dryness. Elemental sulfur was

removed from the extract by overnight reaction with copper pellets activated with 1N hydrochloric acid. The samples were then separated via centrifugation and the supernatant removed to clean vials. Select samples were split into aliquots, with one part being subjected to saponification using KOH. Dry TLE's were methylated by addition of acidic methanol (HCl with anhydrous methanol) and kept at 60°C overnight to convert glycerides and free fatty acids to fatty acid methyl esters (FAMEs). Once methylated, TLE's were separated into five fractions by liquid chromatography over silica gel in a 5 ml fired glass column. Fractions were eluted in an order of increasing polarity: 1) aliphatic hydrocarbons with hexane [1.5 column dead volume (DV) determined empirically for each silica bed]; 2) aromatic hydrocarbons in 2 DV 4:1 hexane/DCM; 3) ketones and FAME in 2 DV DCM; 4) alcohols in 2 DV 4:1 DCM/ethyl acetate; and 5) diols in 2 DV 7:3 DCM/Methanol. Procedural blanks comprised of pre-combusted sand were analyzed parallel to samples to ensure that background compounds are negligible in comparison with biomarker analyte abundances.

To discern *Azolla* biomass inputs into 913B sediments, a sample of the extant *Azolla caroliniana* was extracted and used as a standard comparison for lipid constituents. Whole bunches of *A. caroliniana* including leaves, stems, and roots were carefully washed in deionized water. Washed bunches were then lyophilized and stored in a freezer. Approximately 0.5 g of freeze-dried *Azolla* was crushed to a fine powder in a pre-fired ceramic mortar and pestle. To confirm that *Azolla* specific biomarkers could survive through our sedimentary extraction procedures, this plant powder was extracted as above in a solvent-bath using the MARS. This yielded a large quantity of bright green

TLE (likely due to an abundance of extracted chlorophyll). No activated copper was added to these samples based on the assumption that *Azolla* does not host a large amount of organic sulfur. TLE was aliquoted and separated into three fractions via liquid column chromatography. These were aliphatic and aromatic hydrocarbons, as above, and then everything else eluted as polars using 4 DV 4:1 DCM/MeOH.

3.4. Continuous flow catalytic hydropyrolysis (HyPy)

To determine the preservation potential of *Azolla* lipid compounds in the sedimentary record, I used continuous flow catalytic hydropyrolysis (HyPy) to fragment *Azolla* biomass and release the core hydrocarbons from parent lipids and other cell material. This was done on both whole *Azolla* samples as well as the residue left over from exhaustive solvent extraction. This HyPy technique was also applied to select pre-extracted sediment samples to determine the bound biomarker content of site 913B kerogens, in order to check the consistency between bitumen and kerogen phases of organic matter. All samples follow the same procedure. For modern *A. caroliniana* samples, ~0.5 g of both simply freeze dried powder and pre-extracted *Azolla* residue are used, while in 913B sediment samples up to 1.5 g (depending on TOC) of exhaustively pre-extracted *Azolla* interval sediment powders are loaded with ~5-6 wt% MoS_2 catalyst (Love et al., 1995; Love et al., 2005). For each run, a HyPy procedural blank was heated from room temperature to 250°C at 100°C/min up to 520°C at 8°C/min. Following this, a sample runs on the same temperature program. Both blanks and sediment samples require a leak-tight (H_2 leak rate not exceeding 5 bar/min at pressure) set up. H_2 pressures were

maintained in the range of 130-140 bars with a flow rate of 4 L/min. Pyrolysate products were trapped in silica gel cooled by dry ice. Organic products were then eluted from the silica gel by use of a sequential solvent scheme, as above, to yield three product fractions consisting of aliphatics, aromatics, and non-hydrocarbons (polars).

3.5. Gas-chromatography mass-spectrometry

All lipid fractions were analyzed in full scan mode at UC Riverside by gas chromatography–mass spectrometry (GC–MS) on an Agilent 7890A GC system coupled to an Agilent 5975C inert MSD mass spectrometer. The GC temperature program was 60°C (held for 2 min), heated to 150°C at 20°C/min, then to 325°C at 2°C/min, and held at 315°C for 20 min. The GC was equipped with a DB1-MS capillary column (60 m × 0.32 mm, 0.25 μm film thickness) with helium used as a carrier gas. Compounds were identified based on characteristic mass spectra and retention times compared to in house standards and literature databases.

3.6. Metastable reaction monitoring gas-chromatography mass-spectrometry

Saturated hydrocarbon fractions were analyzed by metastable reaction monitoring–gas chromatography–mass spectrometry (MRM–GC–MS) conducted at UC Riverside on a Waters AutoSpec Premier mass spectrometer equipped with a HP 6890 gas chromatograph and a DB-1MS coated capillary column (60 m × 0.25 mm, 0.25 μm film) using He as a carrier gas. The GC temperature was programmed with an initial hold at 60°C for 2 min, then heating to 150°C at 10°C/min rate, followed by heating to 320°C

at 3°C/min rate and a final hold for 22 min; analyses were performed via splitless injection in an electron impact mode, with an ionization energy of 70 eV and an accelerating voltage of 8 kV. MRM transitions for C_{27}–C_{35} hopanes, C_{31}–C_{36} methylhopanes, C_{21}–C_{22} and C_{26}–C_{30} steranes, C_{30} methylsteranes, and C_{19}–C_{26} tricyclics were monitored. Analytical errors for individual hopanes and steranes concentrations are estimated at plus/minus 30%. Average uncertainties in hopane and sterane biomarker ratios are plus/minus 8% as calculated from multiple analyses of saturated hydrocarbon fractions from oil standards.

4. Results

4.1. Bulk sediment geochemistry

A total of 86 sediment samples were analyzed for bulk rock data spanning four core recoveries in hole 913B (47-50). Samples are reported as sediments ranging from 48.26 – 50.21 Ma according to the age model of Inglis et al. (2020). An 8 m core gap splits the upper two cores from the more complete lower cores. Sediments are predominantly a silty clay but contain some more clay-rich matrix with organic particles and are occasionally interspersed with layers of coarser sand. Carbonate mineral content is relatively low, ranging from 5.8 – 29.2 wt% total sediment (mean 14.2 %).

TOC ranges from 0.16 – 7.55 wt% of bulk sediments but most values are appreciable at minimum, with a whole core average of 1.0 wt% (**Fig. 4.2**). TOC content increases up-core; the upper two sections record several higher values > 2.0 wt% and an average of 1.63 wt% (n = 26; though see median = 0.87 wt%) while the lower portions of

the core average 0.72 wt% (n = 60; median = 0.72 wt%).The lower core data appear to be skewed to lower values along with the presence of sandy sediment samples possessing extremely low TOC (n = 9; median TOC = 0.18 wt%). Removing these data gives a corrected median TOC = 0.82 wt% (n = 51) for the lower cores, which is quite similar to the upper core value. Total nitrogen (TN) typically covaries with carbon abundance with a range of 0.02 – 0.28 wt% (r^2 = 0.88; mean TN = 0.08 wt%), indicating most nitrogen is organic-bound or derived from remineralized OM. C/N ratios are relatively variable throughout the recovered sediments and fall between values of 5.8 – 27 (median = 10.9; **Fig. 4.2**). There appears to be a distinctive shift to higher C/N ratios from the lower cores (> 49 Mya; median = 10.3) and upper cores (< 49 Mya; median = 14.1) sections. Within the upper core section, there is a further section of low consecutive C/N values from 688-686 mbsf (mean C/N = 10.5). Overall values generally match against original reported ship data presented by Thiede et al., 1995. Extreme TOC and TN contents are found in two samples, which also record the most elevated C/N ratios. These samples boast TOCs of 7.6 and 6.9 wt%, equal TN at 0.28 wt%, and C/N ratios of 27 and 25, respectively. Both samples are found at 693 mbsf but are interlayered by an organic-poor sample.

Rock-Eval pyrolysis data was generated for 15 samples spaced evenly through the cores with sample TOCs ranging from 0.2 – 7.6 wt%. Despite reasonable – and in some cases extremely high – TOC, both free hydrocarbon and hydrocarbon generation potential (Rock-Eval pyrolysis parameters S1 and S2, respectively) of all samples is extremely low. Few samples have high enough generation potential to assign Tmax values; though these range from 424 – 428°C and appear to indicate a contribution from very thermally

immature labile kerogen. Hydrogen index (HI) values for all samples are extremely low between 4 – 65 mg hydrocarbon/g TOC. Conspicuously low HI values may indicate samples reflect predominantly relatively mature and/or a latent kerogen pool composed mainly of refractory organic carbon derived from oxidation or microbial reworking.

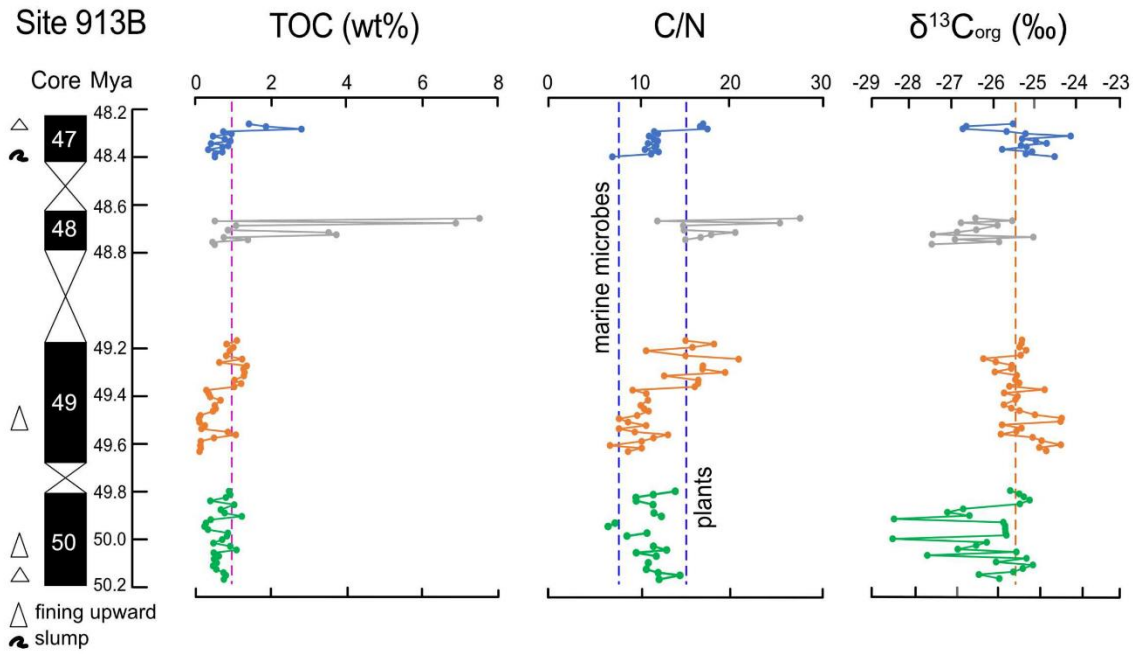

Figure 4.2: Bulk organic geochemistry. Total organic carbon (TOC) contents of sediments are generally low, often below 1.0 wt % as shown by the purple dashed line. C/N contents appear to derive from mixed sources, falling between bounds of marine plankton/microbes and that of the terrestrial plants (dashed blue lines). $\delta^{13}C_{org}$ is quite variable around the -25.5‰ mean value (orange dashed line), but generally appears to show a slight increasing trend in the upper sediments.

4.2. Organic carbon isotopes

Bulk $\delta^{13}C_{org}$ isotope ratios display significant variation throughout the core with a range from -28.4‰ – -24.1‰ (mean ~-25.5‰) but with a more ^{13}C-enriched signal in the upper sediments (**Fig. 4.2**). This range is typical for Eocene sediments, but many of the bulk values are more ^{13}C-enriched than the baseline of -27‰ for sediments from the co-eval ACEX core *Azolla* interval. If the entire section is considered as a whole interval, there appears to be no obvious correlation between $\delta^{13}C_{org}$ and TOC ($r^2 = 0.13$). Splitting into individual sections, cores 47 and 49 are generally more enriched in $\delta^{13}C_{org}$ than cores 48 and 50 (medians of -25.2 and -25.4% versus -26.4 and -25.7, respectively). Within each core, absolute values vary by about 2‰, with fluctuations between local maxima and minima occurring quite rapidly. Adjacent samples rarely yield identical $\delta^{13}C_{org}$ values. While all cores consistently fluctuate from local maxima and minima in $\delta^{13}C_{org}$ between adjacent samples, the range of variation is different between the core sections. Cores 48 and 50 record higher levels of internal variation than cores 47 and 49. With the exception of two outliers at the uppermost layers of core 47, samples from cores 47 and 49 not only fall much more stably around the -25.5 mean value but also record less variation extreme variation between samples with total $\delta^{13}C_{org}$ ranges of 1.6 and 1.9‰, respectively. In contrast, cores 48 and 50 exhibit differences of 2.4 and 3.4‰ for bulk $\delta^{13}C_{org}$, respectively, between their maxima and minima.

4.3. Sedimentary lipid biomarkers

4.3.1. *Aliphatics*

Aliphatics (F1) hydrocarbons represent a small portion of extractable organic matter in our Site 913B sediments, likely due to the very low thermal maturity of the host sediments. However, detailed examination of this fraction can provide many insights into the deposition and preservation of organic matter. Total ion current chromatograms (TICs) of the aliphatic fraction generated from GC-MS are typically dominated by late-eluting cyclic alkanes that include both saturated and unsaturated versions of terpenoid biomarkers – hopanes, steranes, and other various triterpenes (**Fig. 4.3**). Some samples also show elevated peaks for more volatile compounds towards the beginning of the chromatograms, due to rare enrichments in diterpenoids. The dominance of terpenoid biomarkers over *n*-alkanes is a bit unusual for ancient sediments, but actually common for more recent immature organic matter (Peters et al., 2005). Linear *n*-alkanes are broadly produced by many organisms but are typically found in the rock record as the result of thermal and chemical degradation of more complex organics. The general paucity of *n*-alkanes is likely due to the relative immaturity of the host sediments, which is corroborated by Rock-Eval pyrolysis data indicating both low burial temperatures and low hydrocarbon generation potential.

Variations in *n*-alkane abundance profiles are often influenced by organic matter source. Short chain *n*-alkanes (*n*-$C_{15\text{-}19}$) are prominent in marine systems while terrestrial organic matter is often characterized by longer chain terrestrial plant waxes (*n*-$C_{27\text{-}33}$) often possessing a very strong odd-over-even carbon number predominance. Alkane

average chain lengths (ACL) are used as a measure of change in higher plant communities (Pancost and Boot, 2004): ACL = (25 × C_{25}) + (27 × C_{27}) + (29 × C_{29}) + (31 × C_{31}) + (33 × C_{33}) / Σ($C_{25\text{-}33)odd}$. Similarly, the carbon preference index (CPI) is used to determine the overall odd-over-even predominance in long chain alkanes (Bray and Evans, 1961) that is used to interpret transport, degradation, and thermal maturity (Diefendorf and Freimouth, 2017) and is defined here as: CPI = 0.5 × ((C_{25} + C_{27} + C_{29} + C_{31} / C_{26} + C_{28} + C_{30} + C_{32}) + (C_{27} + C_{29} + C_{31} + C_{33} / C_{26} + C_{28} + C_{30} + C_{32})). The terrestrial to aquatic ratio (TAR) tracks the overall ratio of long-chain to short-chain *n*-alkanes as a proxy for biogenic source inputs: TAR = C_{29} + C_{31} + C_{33} / C_{17} + C_{19} + C_{21}. Finally, since many aquatic macrophyte plants make abundant mid-chain *n*-alkanes, the percent aquatic ratio (P_{aq}) provides constraint on the sources of higher-chain compounds (Inglis et al., 2020): P_{aq} = C_{23} + C_{25} / C_{23} + C_{25} + C_{29} + C_{31}.

While present in all samples, *n*-alkanes represent only a small proportion of the total aliphatics found at Site 913B (see **Fig. 4.3**; similar to previous early-middle Eocene reports by Inglis et al., 2020). The *n*-alkane parameters for most samples are relatively intermediate in overall chain length and consistent throughout the cores. ACL ranges from 25.8 – 28.8 with a mean value of 28.3. ACL exhibits a moderate correlation to sample TOC (r^2 = 0.41) – low TOC samples also tend to have a lower ACL. CPI values show that odd carbon numbered alkanes are predominant throughout the core, though this is more noticeable in the longer chain compounds, as expected (range = 1.7 – 4.8; mean = 2.4). This is suggestive of thermally immature organic matter that retains a biologically inherited odd-over-even carbon number preference. CPI values are consistent throughout

the samples with occasional high values (i.e. 4.8), however, there is no correlation to TOC content. The TAR is typically intermediate for all samples with a median of 1.6 (range = 0.4 – 2.9). The P_{aq} ratio is unsurprisingly similar to ACL, showing a general range of 0.4 – 1.0 (median 0.5), with the high values representing organic lean samples that are depleted in long-chain alkanes, rather than an abnormal abundance of mid-chains.

While *n*-alkanes are rather low abundance, Site 913B polycyclic biomarker alkanes are both abundant and diverse in their distributions. Hopanoids make up the bulk of the resolvable compounds within the aliphatic fraction of the bitumen. These are present as both hopanes and hopenes (saturated and unsaturated forms) ranging from C_{27}-C_{35} and can be used to infer host sediment thermal maturity and distinguish source inputs to organic matter. For these samples, a straightforward indication of very immature organic matter (as expected from Rock-Eval pyrolysis and *n*-alkane profiles) is the presence of the distinctive (and more thermally unstable) biological ββ stereoisomer for each hopane. Furthermore, ββ-hopane compounds are not only present, but they are very abundant. Typically, the ββ-C_{31} homohopane is the dominant resolvable peak compound evident in full scan chromatograms (**Fig. 4.3**). Other traditional hopane-based thermal maturity parameters applied include the C_{27}H Ts/Tm ratio and the C_{31}H 22S/(S+R) ratios. These are both moderately variable throughout the cores (**Fig. 4.4**) but generally low values (both medians = 0.18) indicate immature sediments significantly before oil generation. The homohopane isomerization parameter [22S/(22S+22R)] shows an apparent increase in value from the C_{31}-C_{35} homohopanes in all samples (**Fig. 4.4**). While some variation in isomerization is common between different homohopanes (Zumberge,

1987; Peters et al., 2005), the range from 0.1 to 0.5 with increasing carbon number in nearly all Site 913B samples is unusual. However, the presence of abundant ββ-hopane isomers and consistency with other traditional maturity parameters would suggest that the C_{31} S/(S+R) ratio is accurate, with the extended C_{32}-C_{35} homohopanes potentially being derived from a different source of different maturity and/or having undergone more reworking. The homohopane index (HHI; C_{35} homohopane /ΣC_{31}-C_{35} homohopanes) is low for nearly all samples (median = 0.74), with a few moderate HHI values up to 3.48 (n = 3).

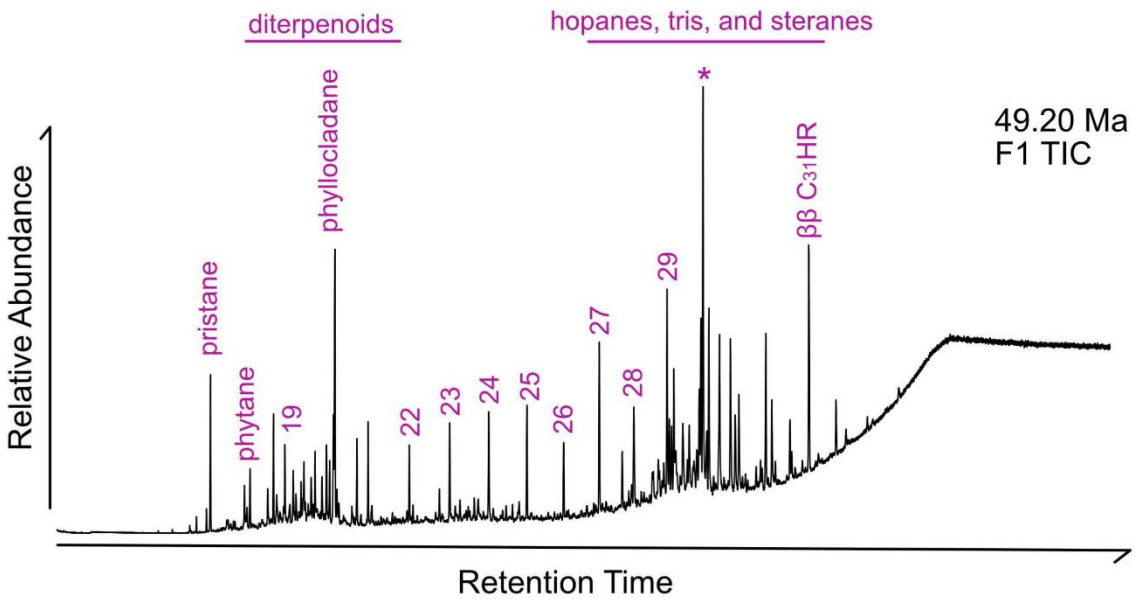

Figure 4.3: Representative GC-MS aliphatics. Aliphatic fractions tend to have enriched triterpane biomarkers relative to *n*-alkanes, as seen here. Note the increased odd-over-even predominance in the long chain *n*-alkanes as well as the overall low signal, shown by the baseline column bleed creeping up at the end of the chromatogram. This sample has some unusual features, namely an abundance of diterpenoids and the predominant * biomarker, which is the neohop-13(18)-ene. Numbers represent carbon chain lengths of corresponding *n*-alkanes.

Comparing the relative proportion of hopanes to steranes in a sample provides important information about the source of biomass, as hopanes and steranes predominantly derive from bacterial and eukaryotic products, respectively. The hopane/sterane ratio (H/S; defined as C_{27}-C_{35} hopanes/C_{27}-C_{29} regular steranes) at Site 913B is mostly elevated from 1.0 – 17.4 (median = 5.5) compared to the Phanerozoic marine average of 0.5 – 2.0 (Cao et al., 2009). In fact, only two samples fall within the Phanerozoic marine average, despite extreme enrichments in TOC up to 7.5 wt%. This suggests that there was either a high proportion of bacterial biomass incorporated into the sediments or that there was extensive bacterial reworking of the Site 913B organic matter.

Though less abundant that hopanoids, sterane biomarkers show a few distinct trends throughout these cores. First, metrics of thermal maturity such as sterane isomerization patterns [i.e. C_{29} ααα S/(S+R); **Fig, 4.4**], predominance of the biological C_{27}-C_{29} αααR sterane isomers, and the presence of βαα isomers strongly suggest immature organic matter, in accordance with the major hopane stereoisomer ratios. Sterane carbon number patterns, which can be used to distinguish between groups of eukaryotic phytoplankton (Kodner et al., 2008), are typically dominated by C_{29} (stigmastane) compounds (median 44% of total steranes; **Fig. 4.3**). This suggests a prominent carbon source from terrestrial plants, especially given the waxy n-alkane distributions and other molecular indicators of terrestrial inputs (see later), with perhaps some contribution from marine green algal clades. Overall sterane patterns appear to be controlled by the variable influx of C_{29} sterane. The other major steranes (C_{27} and C_{28}

compounds) strongly covary throughout all samples, suggesting a similar source environment for those two groups. Importantly, every sample has a small but distinct signal from 24-*n*-propylcholestanes (24-npc; median = 2% of total steranes) likely sourced from marine pelagophytes. Methylsteranes, including both the C_{30} 4(α,β),23,24-trimethylcholestanes (dinosteranes), as well as C_{30} 4-methylstigmastanes are consistently present at low abundance in all samples.

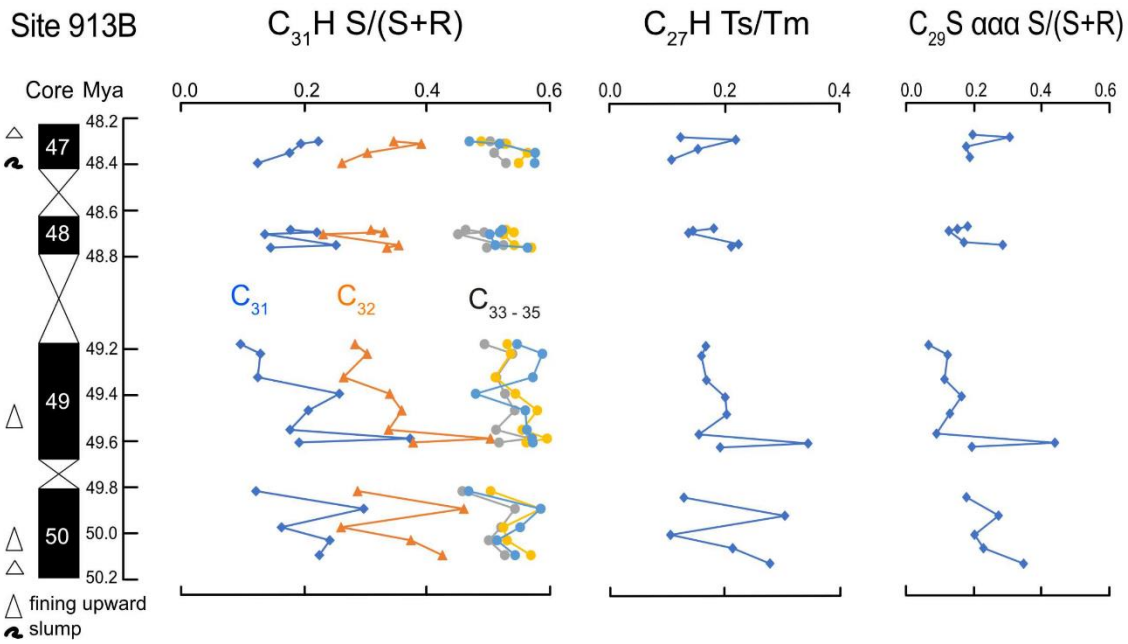

Figure 4.4: Biomarker thermal maturity parameters. The biomarker thermal maturity parameters from stereoisomer ratios generally indicate highly immature organic matter consistent with the maturity of the host sediments. There is some variation in the older sediments, likely indicative of source mixing, but all stereoisomer ratios have not reached their thermal equilibrium values.

Many samples record a large abundance of a C_{29} triterpene eluting directly before the C_{29} αβ hopane (and nearly on top of the C_{29} αααR sterane); although the exact ID is unknown, mass spectral characteristics suggest a nor-oleanene compound. A similarly

large hopene (identified as the neohop-13(18)-ene) elutes directly after the C_{30} αβ hopane. Another terpenoid biomarker parameter that bears mentioning is gammacerane – only present here in vanishingly small amounts. Some samples possess extreme outlier abundances of rare compounds, such as a major enrichment in a diterpenoid (tentatively identified as phyllocladane; **Fig. 4.3)** and an unusually enriched C_{28}-(28,29) bisnorhopane.

The HyPy aliphatic fraction of an extracted sediment (sample 48.69 Ma) provides an interesting counterpoint to the bitumen extracts. Hopanes are again the predominant signal, with the C_{27} Tm and C_{29} αβ hopane the most elevated of those. The C_{31} homohopanes are still present in relatively high amounts (especially the ββ isomer) but do not express the dominance shown in the corresponding bitumen phase. C_{27} and C_{29} steranes are equivalent in magnitude, with lesser amounts of the C_{28}. Extended homohopanes and C_{30} methylsteranes are also present in low to trace abundances. Overall, the bitumen and kerogen phases are similar, the main contrasts are the expected lack of diasteranes in pyrolysate and the loss of the larger triterpene peaks. So, the biomarker assemblages from this HyPy experiment confirm that the main biomarker compounds detected in the bitumen phase are endogenous constituents.

4.3.2. Aromatics

Site 913B sediments host an astonishing diversity of aromatic compounds including polycyclic aromatic hydrocarbons (PAHs) as well as aromatic diterpanes, triterpenes, hopanes, and steranes. Many of the compounds found in these samples remain unidentified or can only be tentatively identified; thus, a full characterization of

these complex mixtures is not attempted here. Overall, the F2 TICs can be broadly split into those enriched in low molecular weight early eluting compounds and TICs enriched in larger late eluting compounds **(Fig. 4.5)**. The early eluting compounds are usually dominated by aromatic diterpenoids while the latter half of the chromatograms primarily represents aromatic triterpenoids.

Aromatic diterpenoids have been generally ascribed as the diagenetic products of gymnosperm resin compounds (Simoneit et al., 1986). A variety of these diterpenoids are detectable in the Site 913B samples, typically including retene (m/z 219), simonellite (m/z 237), and dehydroabietane (m/z 255). Retene is especially prominent in many samples, often far and away the most characteristic peak (**Fig. 4.5**). Retene dominance decreases stratigraphically from the oldest samples (core 50) to the youngest (core 47), which may indicate a lessening of gymnosperm input to sedimentary organic matter over time. The second half of the aromatic F2 TICs hosts aromatic triterpenoids and benzohopanes. These triterpenoids include both des-A (loss of the triterpene A ring; see Jacobs et al., 2007; Eiserbeck et al., 2012) and C-ring cleaved structures, the latter of which are expected to be the precursors of certain trimethylnaphtelenes (Chaffee and Fookes, 1988; Peters et al., 2005).

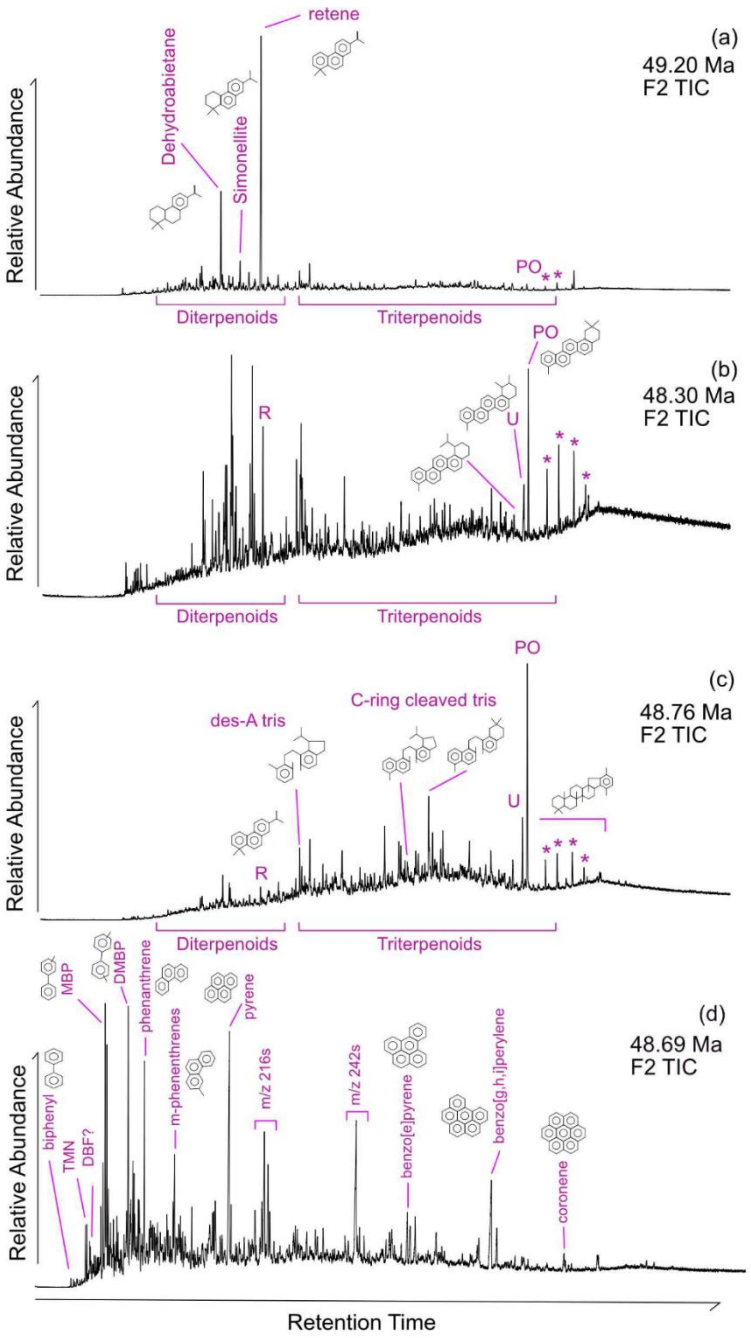

Figure 4.5: Comparative distributions of aromatic hydrocarbons in sedimentary extracts and in a kerogen HyPy product. Representative total ion current chromatograms (TICs) of (a) diterpenoid-rich sample, (b) mixed source sample, (c) triterpenoid dominated sample, and (d) kerogen composed heavily of condensed and stablepolycyclic aromatic hydrocarbons. R = retene; PO = pentanoroleanane; U = ursane derivative; * = benzohopanes; TMN = trimethylnaphtalene; DBF = dibenzofuran; (D)MBP = (di)methylbiphenyls – where the methyl group position is unknown.

The most common aromatic triterpene found in these samples is a tetra-aromatic derivative of β-amyrin identified as a 2,2,9-trimethyi-l,2,3,4-tetrahydropicene (or as a pentanoroleananonaene), which has been previously described from Eocene Arctic organic matter and oils (m/z 324, 268; henceforth, PO; Chaffee and Fookes, 1988; Schouten et al., 2007; Eiserbeck et al., 2012; Huang et al., 2013). PO increases in prominence in the younger samples – an opposite trend than observed in the diterpene retene.

Given the high abundance of hopanes and hopenes, it is not surprising that there is a wide range of aromatic hopanoids preserved in these sediments. There appear to be a number of tentatively identified tetra-aromatic hopanes (m/z 324) mixed in with other triterpenoid derivatives, though it is possible these could be derived from the lupane family, further work is needed to distinguish the two. Additionally, all samples preserve detectable benzohopanes (C_{32}-C_{35}) , which are a commonly occurring family of sedimentary hexacyclic compounds consisting of a hopane with an attached benzene ring. Benzohopanes are found in most thermally immature sedimentary samples and appear to be derived from functionalized hopanoids (bacteriohopanepolyols) during early diagenesis (Wei and Songnian, 1989; Schaeffer et al., 1993). Benzohopanes occasionally make up the bulk of the late eluting aromatic compounds.

The kerogen-bound aromatic fraction of the 48.69 Ma sediment sample is quite different from its corresponding bitumen phase. HyPy released aromatic TICs appear to be dominated by distributions of pericondensed PAHs including phenanthrene, pyrene, benzo[g,h,i]perylene, and coronene. Tri-methylated naphthalenes (m/z 170), alkylated

phenanthrenes (m/z 192), methylpyrenes (m/z 216), and methylchrysenes (m/z 242) are present in appreciable abundance. Intriguingly, the front end of the chromatograms is enriched in aromatic compounds possibly derived from carbohydrate alteration, including biphenyl (m/z 168), alkylated biphenyls (m/z 182), and some detectable dibenzofuran (m/z 168). One note is that this 48.69 Ma sediment has the highest TOC within our dataset; HyPy analysis of lower TOC samples would clarify if this contrast between bitumen and kerogen aromatics is a consistent feature of Site 913B organic matter or a sample specific result. Specifically, this result hints that a high proportion of the sedimentary organic matter found in these high TOC rocks is aromatic-rich kerogen.

4.3.3. *Carboxylic acids*

The carboxylic acid fraction (F3) of Site 913B samples is primarily composed of two different groups: late eluting hopanoic acids, consistent with the overall hopanoid trend, as well as *n*-alkanoic acids, analyzed as methyl esters (**Fig. 4.6**). Hopanoic acids are typically the most abundant constituents of the acid fraction from Site 913B in a series ranging from C_{30} – C_{34} compounds. The most abundant is univariately the C_{32} homologue possessing the biologically inherited (22R)-17β,21β(H)-stereochemistry, which is a commonly found major geohopanoid in thermally immature sediments (m/z 263; Buchholz et al., 1993; Abbott et al., 2001; Farrimond et al., 2002).

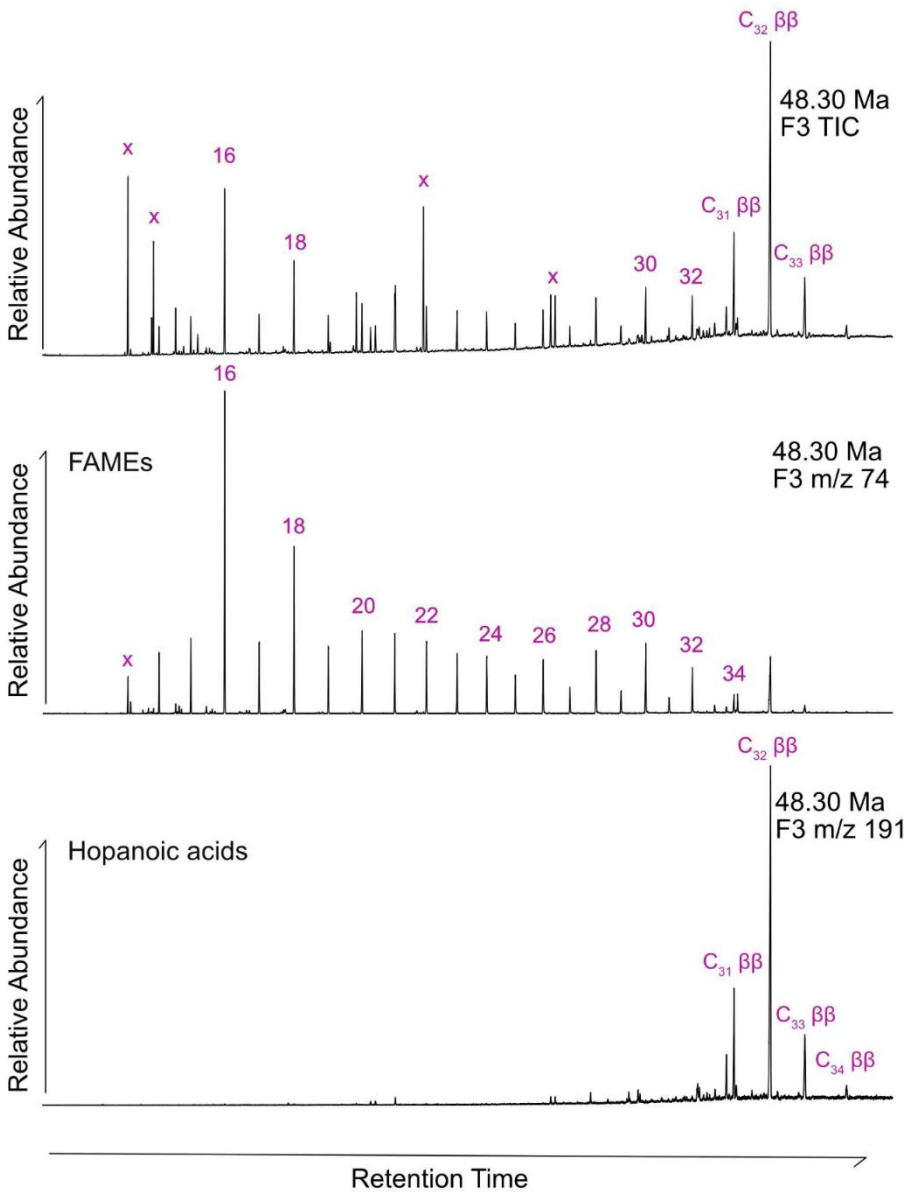

Figure 4.6: Acid fraction chromatograms. Total ion current (top) of a representative F3 split into its two major components: fatty acid methyl esters (FAMEs; middle) from m/z 74 chromatograms and hopanoic acids (bottom) from m/z 191 chromatograms. The C_{32}-ββ hopanoic acid is typically the most predominant compound, followed by the *n*-C_{16} fatty acid. Measured contaminants are marked with an x. Singular numbers represent the carbon chain length of individual FAMEs. Notice in the long chain FAMEs there is a distinct even-over-odd predominance as well as a low abundance of branched and unsaturated FAMEs.

Alkanoic acids (here converted to methyl esters; FAMEs) are functionalized molecules with an acid head group and a linear hydrocarbon tail. These molecules are common constituents of membrane lipids and typically show a strong even carbon number in most living cells. Over geologic time, these compounds can degrade into *n*-alkanes that are one carbon less than their corresponding fatty acid, due to cleavage at the acid group carbon. Thus, comparing distributions of FAMEs to *n*-alkanes can provide insight into diagenetic changes in organic matter over time (Peters et al., 2005). Long chain alkanoic acids are much more prevalent in their respective F3 fraction than the low-abundance *n*-alkanes found in the aliphatics. At Site 913B, FAMEs typically range from $C_{14} – C_{32}$ (though some samples retain chain lengths up to C_{36}) with the C_{16} saturated FAME typically the most predominant, as common for marine sedimentary samples (Budge, 1999). There are also short chain ($<C_{20}$) branched and unsaturated FAMEs with low relative abundances. FAME-based TAR [though in this case using the $(C_{28} + C_{30} + C_{32})/ (C_{14} + C_{16} + C_{18})$ FAMEs], potentially representing terrestrial plant wax inputs, is decently correlated to the *n*-alkane TAR on a simple linear scatter ($r^2 = 0.45$). The ratio of mid-to-long chain FAMEs [P_{mc}; $(C_{20} + C_{22} + C_{24} + C_{26}) / (C_{28} + C_{30} + C_{32})$] is also surprisingly well correlated to the mid-to-long chain alkane distributions of P_{aq} ($r^2 = 0.71$).

4.4. Azolla lipids

To quantify possible *Azolla* source organic matter input to sedimentary biomass, accurate identification of *Azolla* lipid biomarkers was necessary (i.e. Speelman et al.,

2009a; Nierop et al., 2018). Whole extracts and fractions of *Azolla caroliniana* were analyzed by GC-MS and MRM-GC-MS to obtain accurate retention times and mass spectra for comparison to Site 913B sedimentary samples and to ensure that our methods produced the expected results. A suite of *Azolla* biomarkers, especially the ω9,ω10-diols, were detected in both the derivatized TLE and polar fraction of the *Azolla* extract, as well as in the respective saponified versions, similar to the original characterization of an *Azolla* macrophyte by Speelman et al. (2009a). These compounds were found in none of Site 913B sediment samples analyzed, however, either in purified lipid fractions or in whole total lipid extracts (TLEs), including in sedimentary samples previously shown to host *Azolla* massulae (i.e. Brinkhuis et al., 2006). However, instrument constraints prevented all samples from being analyzed, so further work is necessary to definitively say that *Azolla* biomarker compounds are not present at this location.

Catalytic hydropyrolysis provides a way to quickly defunctionalize biomass and produce a suite of hydrocarbons that would be generated from thermal degradation of *Azolla* biomass over geologic time. This is done through preferential cleaving of the functionalized moieties present in the biomass within a strongly reducing hydrogen gas atmosphere (Love et al., 2005). Kerogen-bound aliphatics of *Azolla* show an extensive range of *n*-alkanes and *n*-alkenes (C_{14} – C_{36}), as well as apparent alkadienes at C_{25} and greater, which are more abundant for the C_{32} – C_{36} even homologues and perhaps derive from the abundant C_{32}-C_{36} ω9,ω10-diols within *Azolla*, though the HyPy technique is susceptible to hydrogenations at mid-chain unsaturations (Love et al., 2005; **Fig. 4.7**). The maximum response of *n*-alkanes is typically at C_{23} – C_{24}. Polycyclic alkane

distributions are dominated by the C_{29} steranes (ααaR and βααR stereoisomers; likely derived from sitosterol; Speelman et al., 2009a), with lesser contributions from an unidentified C_{30} triterpene (diploptene or an isomer). There is an additional detection of several intriguing early eluting and unidentified diterpene compound (m/z 123, 278).

Carefully pre-extracted *Azolla* biomass was further hydropyrolyzed to examine the less soluble compounds, possibly representing the composition of the macromolecular structure of *Azolla* biopolymers or strongly retained lipid constituents. There are notable differences from direct HyPy of *Azolla* biomass, including: 1) significantly reduced polycyclic alkane abundance; 2) loss of most alkenes and alkadienes; 3) loss of triterpenes and sterenes; and 4) further enrichment of the midchain *n*-alkanes (**Fig 4.7**). In particular, the C_{23} and C_{24} *n*-alkanes become exceedingly prominent produces from the pre-extracted residual *Azolla* biomass, though longer chain compounds are still present in abundance. Noteworthy, HyPy does yield long chain alkanes from insoluble Azolla biomass extending up to *n*-C_{36} within a prominent cluster of C_{32}, C_{34} and C_{36} *n*-alkanes as found as a carbon number pattern for the extractable diols.

5. Discussion

5.1. Composition of Site 913B organic matter

Sedimentary organic matter is inherently heterogeneous, consisting of a complex mixture of individual discrete compounds and macromolecules derived from many different biogenic sources. The organic signal could be derived from terrestrial or marine organisms, at varyings state of preservation and alteration, from pristine to heavily

reworked biomolecules or ancient recalcitrant organic matter transported to a marine depocenter, or from a mixture of these inputs. Deconvolving this history can be a significant challenge. However, it is imperative to disentangle the individual sources and quality check the overall preservation of organic matter within each local depositional site before using an organic-based record to make broader inferences (Stein et al., 2006). At this high latitude depositional site, during a time of repeated climactic perturbations, variations in organic matter source and preservation are expected with high resolution sampling and must be considered.

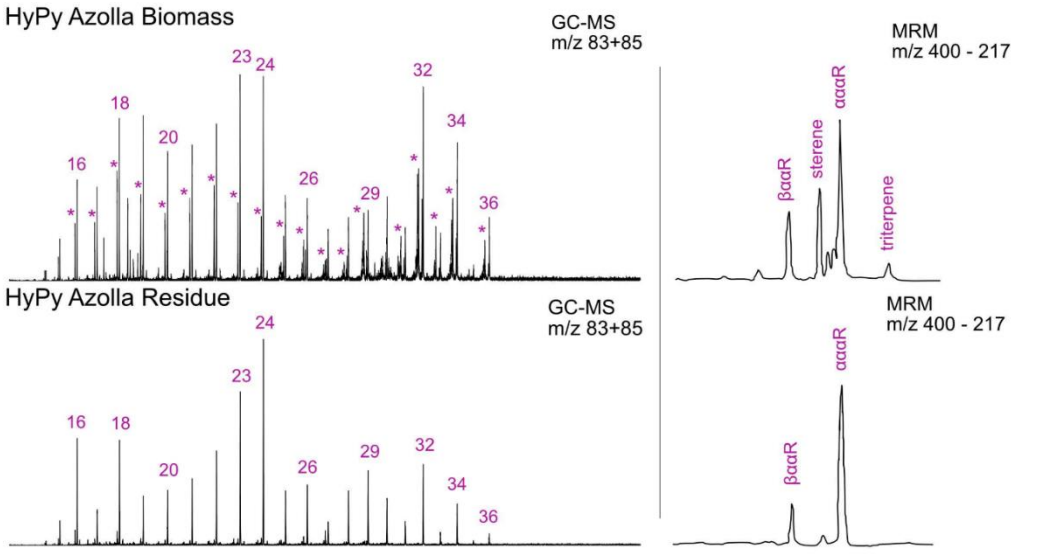

5.1.1.

Figure 4.7: *Azolla* HyPy. Aliphatic fractions of *Azolla* whole cells (upper) and insoluble biomass (lower) generated from catalytic hydropyrolysis (HyPy). On the left side, are stacked GC-MS traces for m/z 83+85, showing the distribution of *n*-alkanes (numbers) and various alkenes (indicated by the * markers). The whole cell product has abundant unsaturated compounds and prominent even numbered predominance long chain compounds, likely reflecting the abundance of long chain diols in *Azolla*. The residue, however, shows a higher signal from mid-chain *n*-alkanes with a lower degree of unsaturation. MRM traces of the C_{29} steranes (right) are characterized in both samples by biologic isomers likely derived from sitosterol or other C_{29} parent sterols, as typical for HyPy products. The whole cell product displays a strong signal of unsaturated compounds (sterenes and a co-eluting triterpene) that is missing from the residue, indicating that these compounds are more readily extractible and volatilized at low temperature during HyPy treatment.

Thermal maturity and preservation of organic matter

Lipid biomarker parameters for thermal maturity, including the C_{27} hopane Ts/Tm ratio, C_{31} homohopane 22S/(S+R) stereoisomer ratio, and C_{29} sterane ααα R (S/S+R) ratio are consistent with Rock-Eval pyrolysis and suggest that the labile, extractable organic matter at Site 913B is very immature, prior to any oil generation and free from overprinting migration (**Fig. 4.4**; see Peters et al., 2005 for a breakdown of stereoisomer ratios). The predominance of the biologic ββ isomers in hopanes and hopanoic acids (Schouten et al., 2007; Weller and Stein, 2008), CPI values > 1, and the general abundance of functional moieties lends further support for immature labile organic matter. HI values are extremely low for these samples (<65), which, at face value, could imply any of a high maturity, aromatic, or oxidized kerogen source to sedimentary organic matter. HyPy of kerogen residue reveals that the aromatic fraction (and generally the whole pyrolysate) is dominated by condensed aromatics from inert macromolecules (**Fig. 4.5**). The low HI values are likely derived primarily from this aromatic kerogen composition, since this phase will represent the bulk of the organics in the sediment. Therefore, the overall organic matter is consistently immature, but extractible bitumen is superimposed over highly aromatic, inert kerogen.

The similarities between *n*-alkane and FAME carbon number distributions may suggest that the *n*-alkanes could be largely derived from sedimentary fatty acids and alcohols. Following that logic, the relative high abundance of FAMEs compared to the low abundance of *n*-alkanes could be interpreted as a sign that a significant portion of this organic matter has yet to undergo any significant thermal maturation, which is consistent

with other biomarker parameters. Similarly, the unusual predominance of C_{31} hopanes may be derived from defunctionalization of the abundant C_{32} ββ hopanoic acids, as has been previously suggested from immature samples (Farrimond et al., 2002).

5.1.2. Terrestrial versus marine source

Rock-Eval pyrolysis is a common screening tool to characterize bulk compositions and types of organic matter in ancient sediments. Low HI values are typical of overmature ancient kerogens although less commonly may be found for immature, terrestrially derived organic matter that has undergone oxidative reworking with a larger relative proportion of humic materials and carbohydrates (Hatcher and Romanikov, 1985; Peters et al., 2005; Carrie et al., 2012). However, low HI is also sometimes correlated with low TOC contents of sedimentary rocks. This is not the case at Site 913B; HI values as low as 21 correspond to TOC enriched to 7.6 wt%. This is unusual for ancient sediments and further suggests that not only is there a terrigenous source, but that remobilized kerogen is largely inert [and see Boucsein and Stein (2009) for discussion on organic macerals]. The finding that kerogen-bound aromatics are elevated in metastable carbohydrate derivatives and condensed PAH supports a major source from relatively oxidized soils or coals (Achten and Hofmann, 2009).

While repeated identification of marine dinocysts is highly suggestive of a marine depositional environment, a terrestrial contribution to Site 913B organic matter has long been recognized from an elevated carbon to nitrogen data point and freshwater dinocysts (Myhre et al., 1995; Andreasson et al., 1996; Brinkhuis et al., 2006; Barke et al., 2012).

C/N ratios measured in this study generally fall in the range of 10-15, corroborating these findings. Typically, microbial biomass (including marine plankton and heterotrophic bacteria) has a C/N value around ~7 (Godfrey and Glass, 2011) while higher plants have higher C/N ratios (> 15) due to the greater expression of structural carbohydrates (i.e. cellulose and lignin) over proteins (McGroddy et al., 2004; Godfrey and Glass, 2011). Intermediate values, such as found here, probably indicate mixed sources of organic carbon derived from both marine planktonic biomass and higher plants. The samples with the highest C/N ratios also have enriched TOC contents. This could result from a higher proportion of terrigenous materials or from extensive heterotrophic remineralization and nutrient recycling of nitrogen into biomass (i.e. van Kempen et al., 2012). The *n*-alkane TAR corroborates the C/N results, with intermediate values indicative of a mix of sources between marine bacteria/algae and higher plants (Inglis et al., 2020), though longer-chain plant waxes appear to account for a bit more of the (albeit weak) *n*-alkane signal on average.

Diverse di- and triterpenoids suggest a terrigenous plant source to free lipids. The aromatic diterpenoid retene is particularly abundant. While retene has been detected in a wide range of organisms, including some marine algae, it is typically in low concentrations except for in conifer resins (Lin and Chang, 2000). Thus, the simple abundance of retene suggests that this compound is likely sourced from onshore terrestrial plants (i.e. conifers; Inglis et al., 2020). The aromatic triterpenoid compounds tentatively identified here are derived from members of the oleanane, lupane, and ursane families, which are typically thought to be biomarkers for angiosperms, with a diagenetic

formation process derived from precursor molecules such as oleanic acid or β-amyrin (Ten Haven and Rullkötter, 1989; Otto et al., 2005; Eiserbeck et al., 2012). The total array of higher plant lipids found in these samples provides a strong argument for a significant portion of the labile sedimentary OM to have come from land.

The prevalence of hopanoid-derived compounds in every analyzed biomarker fraction, in particular the hopanoic acids, is also highly suggestive of a major terrigenous source input to organic matter (Peters et al., 2005). Hopanoic acids are found in most sedimentary samples but are especially predominant in samples with inputs from terrestrial soils, where they have been interpreted as oxidative products in the heterotrophic reworking of bacteriohopanepolyols (Saito and Suzuki, 2007). This distribution could also arise from bitumen biodegradation (Meredith et al., 2000), but due to the immaturity of the host sediments (and lack of any significant unresolved complex mixture in chromatograms), is it more likely that any biodegradation/oxidation took place before deposition at Site 913B. The ratio of the C_{16} FAME to the C_{32} ββ hopanoic acid (F/H) may be of use to distinguish samples with significant soil/terrigenous inputs, though caution must be exercised when considering depositional redox effects. The F/H ratio is variable throughout these cores, ranging from 0.4 – 15.5 (median = 1.1), supporting a probable mixed source signal for most samples. However, the presence of several high values produces an intriguingly dichotomous distribution in this ratio when plotted against TOC. Samples with high relative FAMEs also tend to have relatively low TOC, while all samples with high TOC also have a larger proportion of hopanoic acids (**Fig. 4.8)**. Since hopanoic acids may be sourced through transport of oxidized soil matter,

this suggests that samples with enriched TOC are simply recording a stronger terrestrial signal. An influx of oxidized, refractory soil organic matter, or particulate coal fragments (as mentioned in Thiede et al., 1995), is consistent with the extremely low HI values and could explain how sediments with TOC enrichments up to 7.6 wt% retain almost no hydrocarbon generation potential.

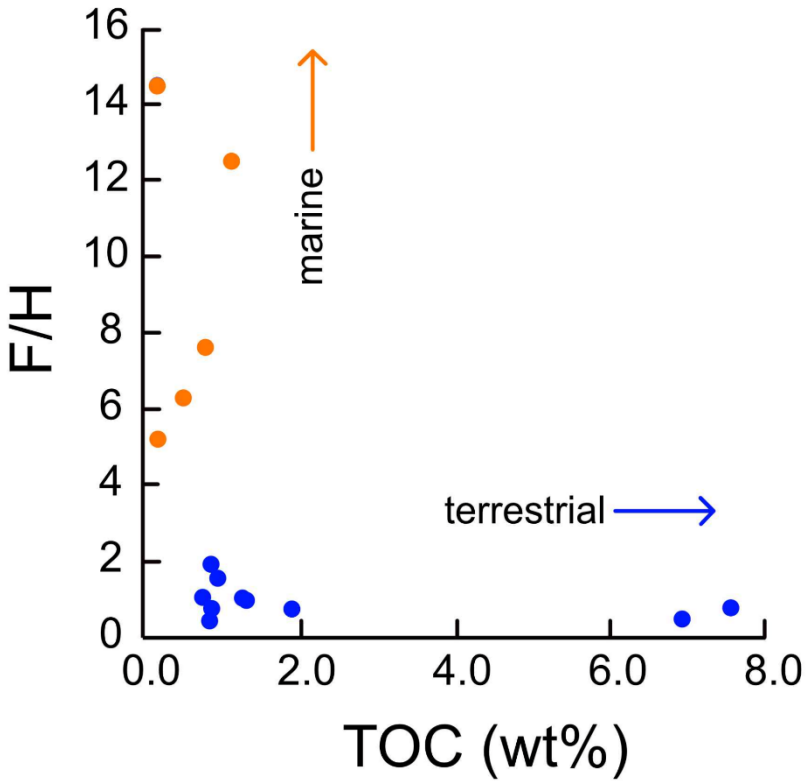

Figure 4.8: Scatter plot of TOC content of sediments vs measured F/H ratio. When plotted against total organic carbon (TOC) content, the F/H ratio (C_{16} saturated FAME/C_{32} ββ hopanoic acid) splits samples into two groups. Samples with high F/H have low TOC, while high TOC samples also have an abundance of hopanoic acids. This suggests that higher TOC samples likely record more terrestrial organic matter whereas low TOC samples are much more clearly mixed source or marine.

Sterane biomarkers can provide an additional degree of OM source specificity. The most abundant steranes in each sample are the C_{29} compounds, stigmastanes (**Fig. 4.9**). Stigmastane precursor compounds (stigmasterol, sitosterol, ect.) are main

constituents of both green algal groups and plants (including *Azolla*; Kodner et al., 2008; Speelman et al., 2009a). C_{27} and C_{28} steranes are common in the red lineage of algal groups (diatoms, coccolithophores, and dinoflagellates; Volkman, 2003; Knoll et al., 2007) or heterotrophic protists (Brocks et al., 2017). These red-derived steranes are usually predominant in Cenozoic marine sediments and covary here in the Site 913B sediments, suggesting they are derived from a singular source environment. Abundances of the C_{29} stigmastanes are decoupled from that trend, suggesting they are derived from a different source, in this case most likely terrigenous or nearshore aquatic plants. An important counterpoint to the prominence of terrigenous sources is the detection of the C_{30} sterane, 24-*n*-propylcholestane (24-npc), in each sample. This compound is known to mainly derive from pelagophyte algae, which are obligatory marine organisms (Volkman, 2003).

Overall, organic matter for samples studied at Site 913B appears to be primarily derived from a terrigenous source transported to a marine depocenter. This result is not necessarily contradictory to previous palynological studies (i.e. Barke et al., 2012), as it should be noted that free biomarkers, kerogen, cysts, and pollen have different transport and enrichment mechanisms that may result in conflicting reports (see Schouten et al., 2007). Terrigenous constituents to organic matter include inert soil-derived kerogen, diterpenoids (i.e. retene), triterpenoids (i.e. oleanane derivatives), diverse hopanoids, long chain *n*-alkanes, and likely the C_{29} steranes. Marine sources encompass the C_{27} and C_{28} steranes, short chain *n*-alkanes and *n*-alkanoic acids, 24-npc, and dinosteranes. Samples with higher relative contributions from marine organisms tend to also have lower TOC

(and qualitatively lower *n*-alkane ACL), which may suggest that these represent a background marine basinal signal in-between periods of larger-scale terrigenous deposition.

5.1.3. Depositional environment

Previous studies of the palynoflora assemblages from the early Eocene at Site 913B revealed a diverse and swampy flora, including conifers, palms, cycads, walnuts, and ferns among others (Eldrett et al., 2009; Greenwood et al., 2010). The wide range of plant-derived di- and triterpenoid compounds in the corresponding sedimentary record is thus unsurprising. Since specific compounds come from compositionally distinct plant sources (i.e. gymnosperm diterpenoids versus angiosperm triterpenoids), comparing the diterpenoid retene with the triterpenoid PO (the R/PO ratio) can provide some indication of what type of flora was predominant in the sedimentary source area (see Shouten et al., 2007; Inglis et al., 2020). Since plant lipids have different production yields and transport mechanics (especially compared to pollen), and in light of the vast amount of di- and triterpenoids not measured in this simple ratio, this should be stressed that this is a more qualitative approach. However, R/PO ratios vary from 0.1 – 52.1 (median 3.6) and appear to clearly reflect a shift in terrestrial source organisms from gymnosperms in the oldest sediments to angiosperms in the younger sediments **(Fig. 4.9**). This matches temporally with a decline in pine species pollen (Eldrett et al., 2009) and would suggest some climatological or hydrological change occurring on the Greenland mainland over time. There is no connection between the R/PO ratio and *n*-alkane plant wax parameters,

except for a weak correlation between relatively higher retene and more terrestrial TAR ($r^2 = 0.38$). This suggests that angio- versus gymnosperm sources of *n*-alkanes are mostly indistinguishable for these samples.

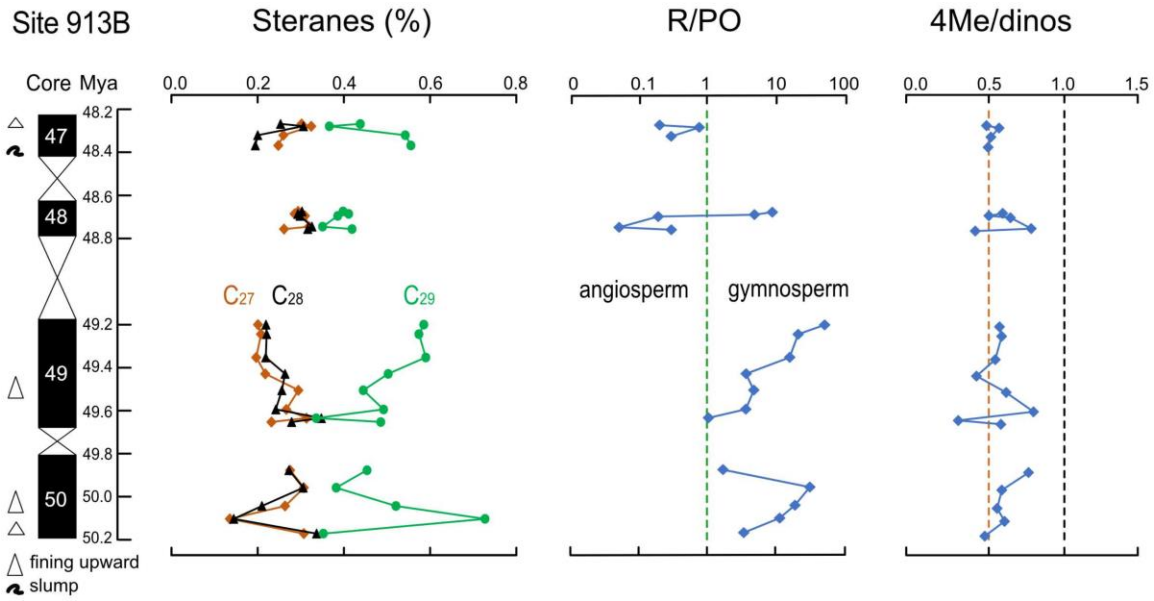

Figure 4.9: Source and depositional environment biomarker stratigraphy. The dominant sterane in almost all samples is the C_{29} stigmastane. C_{27} and C_{28} steranes co-vary and likely represent a planktonic signal, whereas the C_{29} sterane appears to derive from a separate terrestrial source. The retene/pentanoroleanane ratio (R/PO) is a qualitative metric of gymnosperm versus angiosperm biomarker input. There is a distinct increase in angiosperm input in younger sediments (~48 Ma), possibly indicating a change in major land flora. Note the log-scale, samples greater than 1 (green dashed line) have greater gymnosperm influence. The ratio of C_{30} 4-methylsteranes to dinosteranes (4Me/dinos) can be indicative of freshwater incursions. Most samples fall around a low 0.5 (orange dashed line) but have some periods of variation. However, no samples reach near the 1.0 level indicated by the black dashed line. Thus, there is no strong evidence for freshwater incursion for this parameter.

Discovery of characteristically warm, swampy flora and fauna fossils suggested the high latitude regions of the early-middle Eocene were rather warm (Estes and Hutchison, 1980). This has since been backed up by numerous geochemical and modeling studies, which show warm temperatures, a low latitudinal temperature gradient,

and a subsequently strong hydrological cycle (Moran et al., 2006; Pagani et al., 2006; Eldrett et al., 2009; Greenwood et al., 2010; Speelman et al., 2010; Inglis et al., 2020). In the Arctic basin, geographic restriction coupled to increased rainfall and runoff likely led to the generation of a freshwater surface layer, which may have induced stratification and thus influenced deposition and increased preservation of large quantities of organic matter (Brinkhuis et al., 2006). Discovery of massive *Azolla* blooms requires the freshening of surface waters, as *Azolla* cannot survive more than slightly brackish salinities (Brinkhuis et al., 2006; Greenwood et al., 2010; Barke et al., 2012; van Kempen et al., 2013). Similar freshening of the Norwegian-Greenland Sea, as well as the Arctic, has been reported from fish bone and tooth oxygen isotopes, as well as lipid hydrogen isotopes; stratification resulting from such has been suggested as one reason for the occasional, anomalously high TOC in the region and possibly the dissolution of carbonate tests (Andreasson et al., 1996; Waddell and Moore, 2008; Speelman, 2010). A mix of low salinity and marine dinocysts, as well as *Azolla* massulae, have also been found in Site 913B sediments (Barke et al., 2012). However, we see no strong lipid biomarker evidence for pronounced salinity stratification or freshwater surface layers. In particular, the proportion of 4-methylstigmastane compared to C_{30} 4,23,24-trimethylcholestanes (dinosteranes) can be effectively used to pinpoint incursions of fresher surface waters (Goodwin et al. 1988; Behrooz et al., 2018). Dinosteranes are characteristically sourced by dinoflagellates, which can be either marine or freshwater species; as above, cysts of both types have been found at this location (Eldrett et al., 2004; Brinkhuis et al., 2006; Barke et al., 2012). The relative proportion of 4-

methylstigmastane to dinosterane is typically higher during periods of increased freshwater discharge (Summons et al. 1987; Goodwin et al., 1988). However, this ratio remains relatively low and invariant throughout Site 913B (**Fig. 4.9**). A commonly utilized alkane biomarker for stratified environments is the gammacerane index. Gammacerane is derived from tetrahymanol, predominantly produced by heterotrophic ciliates and bacteria that live in stratified water columns (Sinninghe Damsté et al, 1995; Banta et al., 2015). Gammacerane is vanishingly low in all Site 913B samples if detected at all. The source organisms for both these biological parameters likely occur in the Norwegian-Greenland Sea during the early-middle Eocene as shown by detectable contributions to organic matter. Together, these parameters imply no prolonged freshwater stratification at this site in the Norweigian-Greenland Sea during the early-middle Eocene, despite palynological evidence of freshwater dinocysts in 913B sediments (Barke et al., 2012). Perhaps freshening of surface waters was tied to short-term freshwater discharge events, so that the background marine signal from lipid biomarkers shows more long-term averaged seawater conditions.

The restricted nature of the Eocene Arctic drove the Arctic basin anoxic at depth (Weller and Stein, 2008; Speelman et al., 2009b). Similar reducing conditions have been proposed for the Norwegian-Greenland Sea to explain some of the anomalously high TOC values detected in the early-middle Eocene sediments (Thiede et al., 1995; Andreasson et al., 1996). However, we see no evidence of exceptionally reducing conditions in the biomarker profiles, such as diagnostic carotenoid markers (Weller and Stein, 2008). The aliphatic hydrocarbons show only trace amounts of the C_{35}

homohopane, as indicated by the very low HHI in every sample. This would suggest deposition and early diagenesis of these compounds at an oxidative sediment-water interface (Peters et al., 2005).

5.2. Lack of biomarker evidence for **Azolla** *blooms*

Due to the multiple reports of *in situ Azolla* massulae found from Site 913B sediments, we expected to find distinctive biomarker evidence of *Azolla* blooms in the lipid biomarker record (Brinkhuis et al., 2006; Eldrett et al., 2009; Barke et al., 2012). However, we found none of the diagnostic functionalized *Azolla* biomarkers previously described (Speelman et al., 2009a; Nierop et al., 2018). To determine if *Azolla* biomolecules had simply degraded in time, we also looked for a predominance of mid-chain *n*-alkanes as suggested from *Azolla* HyPy residues using the P_{aq} ratio, which would account for the high abundance of what appeared to be structural C_{23} and C_{24} compounds in pyrolysates of *Azolla* residue, as well as general aquatic plants. However, the P_{aq} ratio is rather invariant between samples, where the only real deviations from a 0.5 median come from low TOC samples that simply lack long-chain *n*-alkanes. High C/N ratios have been found in concert with *Azolla* blooms, interpreted to represent periods of extreme productivity combined with nutrient recycling (Speelman et al., 2009b; van Kempen et al., 2012). However, high C/N ratios found at Site 913B appear to be derived from a large proportion of highly aromatized terrestrial organic matter. *Azolla* produces a relatively large lipid yield for a higher plant, as shown by research into its use as a biofuel and by the productive aliphatic yields of our HyPy experiments (Brouwer et al., 2016);

this is inconsistent with largely inert, aromatic kerogen. Pronounced thermal immaturity of host sediments as well as bitumen and kerogen extracts suggest that *Azolla* are unlikely to be thermally degraded to their core lipids. Further, the unique diterpenoids identified in *Azolla* do not match retention time or mass spectra to any of the diterpenoids in extracts from Site 913B sediment samples.

There are a few possibilities why we are unable to find evidence of diagnostic *Azolla* lipids at Site 913B. The simplest is that the compounds are present but in such low abundances that they are below detection limits. A calculated sum of *Azolla*-derived compounds in the Arctic Eocene ACEX samples resulted in concentrations less than 100ppm/TOC (Speelman et al., 2009b). At the same time, the ACEX sediments boast over an order of magnitude greater *Azolla* spore counts than Site 913B and provides excellent preservation of organic matter in the distinctively anoxic Arctic basin (Brinkhuis et al., 2006; Weller and Stein, 2008; Speelman et al., 2009b). Site 913B does not show evidence of low oxygen deposition and would thus be less favorable to preservation of functionalized *Azolla* biolipids. However, abundant functionalized lipids are preserved in Site 913B sediments, so it seems likely that the recalcitrant diols of *Azolla* would be detectable if they had originally been deposited in abundance (Speelman et al., 2009a). Possibly, *Azolla* massulae could have been swept out from a more nearshore growing habitat to a marine depocenter, which would be consistent with the major source of terrestrial, inert kerogen. Due to sampling limitations we were unable to analyze every sample for *Azolla*-derived lipids. Further sample analyses should be undertaken before we can definitively *Azolla* compounds are not present at Site 913B.

5.3. Implications for early-middle Eocene carbon cycles

Eocene climate is broadly representative of a greenhouse system, with warm temperatures and ice-free poles (Zachos et al., 2001; Zachos et al., 2008; Inglis et al., 2015). A characteristic example is the Early Eocene Climactic Optimum (EECO; ~51-53 Ma), where temperatures and pCO_2 reaches the Cenozoic long-term maximum. After the EECO, global temperatures begin a long decline towards more modern icehouse conditions (Speelman et al., 2009b; Zachos et al., 2010; Inglis et al., 2015), with a larger cooling effect possibly occurring at the poles (Pearson et al., 2007). The end of the EECO is also coincident with the abrupt appearance of obliquity cycles at low latitude sites in the middle of Chron 22r, which interrupt the dominant eccentricity trend (Westerhold and Röhl, 2009). Obliquity cycles strongly influence seasonality and thus have a large influence in the high latitudes. Thus, the end of the EECO has been interpreted both as a change in high latitude deep water formation (Westerhold and Röhl, 2009). The influence of obliquity on organic matter burial as a driver of continually cooling temperatures after the EECO is less well known, where cooling is typically attributed to declining atmospheric CO_2 (Inglis et al., 2015; Lunt et al., 2016). Diminishment of the obliquity signal in Chron 22n, combined with geochemical evidence for brackish waters, has been used as evidence that the Arctic and Nordic basins were geographically cut off from the open ocean for a time during Chron 22n, which hosts a major pulse of *Azolla* burial (Barke et al., 2012). However, *Azolla* bloom events in the Eocene Arctic ocean have been separately linked to obliquity cycles, which are detectable through the *Azolla* phase in Chron 21r (Speelman et al., 2009b; Westerhold and Röhl, 2009).

Separately to the occurrence of obliquity cycles at the end of the EECO is another sequence of climatological disturbance. A series of hyperthermal events is maintained throughout the Eocene (Zachos et al., 2010; Sexton et al., 2011; Kirtland Turner et al., 2014). These events are recognized via negative excursions in carbon and oxygen isotopes of carbonate (typically of foraminifera; Sexton et al., 2011), and are generally thought to be related to the injection of light carbon into the surficial Earth system via mechanisms such as volcanism, oxidation of organic matter, or the collapse of methane hydrates (Zachos et al., 2010; Lunt et al., 2011). Eocene hyperthermal events have been shown to be paced by long and short frequencies of orbital eccentricity (405 kyr and 100 kyr, respectively: Kirtland Turner et al., 2014). This pacing, along with short durations and quick recovery times, is similar to other periods in the Cenozoic and suggests mediation of hyperthermal events by transformations of carbon between different transient surficial reservoirs (such as ventilation of oceanic dissolved organic carbon; DOC) as opposed to the slow release of volcanism or catastrophic destabilization of methane hydrates (Lunt et al., 2011; Sexton et al., 2011; Kirtland Turner et al., 2014).

A main goal of this project was to resolve a detailed $\delta^{13}C$ record from Site 913B organics to compare with globally correlated sites. This would potentially aid in detecting or resolving first order drivers of early-middle Eocene climatological change as detailed above. Past studies in high-latitude regions have been hampered by poor core recovery and uncertain age models (i.e. the ACEX expedition; Pagani et al., 2006; Schouten et al., 2007; Backman et al., 2008; Speelman et al., 2009b). Site 913B sediments represent a more complete and highly resolved record that is nicely tied to fixed time points through

magnetochronometry and biostratigraphy, containing sediments of interest from Chron 22n through Chron 21r (Brinkhuis et al., 2006; Eldrett et al., 2009). Unfortunately, a complete, correlatable $\delta^{13}C$ record for the area is not easy to obtain due to a noted lack of calcareous microfossils and carbonate sediments with which to analyze traditional $\delta^{13}C_{carb}$ (Thiede et al., 1995; Andreasson et al., 1996). However, non-negligible levels of TOC in these sediments presented a target for organic carbon isotopes for comparison with global early-middle Eocene sites.

Results from Rock-Eval pyrolysis and lipid biomarker analyses suggest that bulk $\delta^{13}C_{org}$ at Site 913B is not ideal for early-middle Eocene global carbon cycle correlations. The organic matter present at the site appears to be derived predominantly of terrigenous materials including inert, terrestrial kerogen or coals. Due to the nearshore depositional environment, these would have been commonly deposited through freshwater discharge and mass wasting events, as indicated by the fining upward sequences (Thiede et al., 1995; Waddell and Moore, 2008). This means that the bulk organic carbon 1) is heavily influenced by local effects such as the mixing of multiple carbon sources, and 2) was likely deposited in a more non-linear fashion than would be expected for open marine sediments that boast continuous microfossil isotope records. Thus, it is perhaps unwise to use these sediments as direct correlations with other globally distributed Eocene sites. While correlations on a global scale might be fraught with speculation, bulk organic isotopes can still be informative about the local carbon cycle.

The composition of organic matter exerts several controls on $\delta^{13}C_{org}$ distribution. As such, the structure of $\delta^{13}C_{org}$ within individual cores may indicate shifts in OM source

processes. An interesting feature of the bulk $\delta^{13}C_{org}$ record generated here is that the more ^{13}C-enriched core sections are also the least internally variable (**Fig. 4.2**). They also exhibit much stronger correlations between TOC and $\delta^{13}C_{org.}$ This may speak to some consistency in the delivery of organic matter, possibly indicative of a higher proportion of marine-based OM, with less influence from allochthonous organic matter delivery from terrigenous discharge events. While a straightforward and coherent correlation between all samples is lacking, low TOC samples that are associated with a higher marine lipid signal also tend to have heavier $\delta^{13}C_{org}$ (**Fig. 4.2**). This would be consistent with physiological constraints on carbon isotope fractionation by terrestrial and marine organisms. During the Eocene, atmospheric CO_2 concentration was high, and a weak latitudinal temperature gradient would have increased high latitude water availability (Greenwood et al., 2010; Speelman et al., 2010). These parameters constitute two of the main controls on isotope fractionation in plants (Farquhar et al., 1989) and suggest that terrestrial plants would be able to discriminate for lighter carbon, similar to the light $\delta^{13}C$ of higher plant compounds during the Paleocene-Eocene Thermal Maximum (though with caveats due to differing plant physiologies, see Schouten et al., 2007). Marine isotopic fractionation in marine phytoplankton is generally dependent on aqueous CO_2 concentrations and growth rate (Freeman and Hayes, 1992; Wilkes et al., 2018). Warmer Eocene temperatures may have lowered dissolved CO_2 concentrations in the water, where larger algal cells may have been less discriminatory against utilizing heavy CO_2, or bicarbonate, resulting in heavier biomass. Alternatively, bloom events that consume large quantities of aqueous CO_2 can shift $\delta^{13}C_{org}$ records more positive by Rayleigh

fractionation and increased nutrient recycling (i.e. Hayes et al., 1999; Speelman et al., 2009b). Light carbon isotope values for terrigenous soil input also match against studies of soil erosion to marine settings during the end-Permian (Sephton et al., 2005). Compound specific isotope studies are required to further elucidate the components contributing to either enriched or depleted bulk $\delta^{13}C_{org.}$

Due to the repeated negative shifts in carbon isotope ratio, it is tempting to speculate some relationship to the similarly negative Eocene hyperthermals. One concrete observation, though, is that the variations in $\delta^{13}C_{org}$ between spatially adjacent samples are relatively rapid. Light to heavy $\delta^{13}C_{org}$ transitions typically occur on the scale of a few tens of thousands of years, assuming constant sedimentation (from Inglis et al., 2020). Though the Site 913B record here is too discontinuous to generate reasonable power spectra, the rapid fluctuations from light to heavy values and back are reminiscent of short period cyclicity. Rhythmic changes in the hydrological cycle could modulate the relative strength of precipitation, weathering, and runoff, as suggested for the episodic freshening of Arctic surface waters that allowed *Azolla* to bloom freely (Speelman et al., 2009a,b; Greenwood et al., 2010). In turn, remobilization of terrestrially derived kerogen or coal that influences the bulk organic signal would likely wax and wane with the hydrological cycle.

5.4. Possible high latitude early-middle Eocene carbon sinks and sources

Regardless if individual events are detectable at Site 913B or not, climactic changes linked to global carbon cycles throughout the Eocene are profound. Recent

modelling advances suggest that atmospheric CO_2 concentrations are the primary driver of high latitude Eocene cooling (Inglis et al., 2015). Transient shifts in the exogenic carbon system are thought to be at play to control fluctuations of atmospheric CO_2 on reasonably short and repeatable time scales (Kirtland Turner et al., 2014; Galeotti et al 2019). Long term burial of organic carbon is one proposed mechanism to control atmospheric CO_2 concentrations following the EECO (France-Lanord and Derry, 1997). Carbon drawdown through large scale deposition of organic carbon from massive *Azolla* blooms follows on this idea (Moran et al., 2006; Brinkhuis et al., 2006; Speelman et al., 2009b). It is possible, then, that continuous burial of terrigenous organic matter in high latitude sites during the early-middle Eocene contributed to the overall trend of decreasing atmospheric CO_2 following the EECO (Zachos et al., 2001; Zachos et al., 2008; Inglis et al., 2015). Alternatively, the extensive oxidation and reworking apparent in Site 913B kerogens may have been a source of ^{13}C-depleted carbon back to the atmosphere.

Highly refractory organic matter was deposited in local marine sediments over the early-middle Eocene at Site 913B. While there are episodes of extremely enriched TOC, similarities in Rock-Eval pyrolysis parameters between low and high TOC samples suggests that refractory organic matter was deposited consistently over the course of a few million years. Abundant aromatics and hopanoic acids suggest a strong source from weathered terrestrial soils and plants (Sephton et al., 2005; Saito and Suzuki, 2007). Scattered coal fragments have been identified in these early Eocene Site 913B sediments (Thiede et al., 1995). The distribution of kerogen-bound aromatics including biphenyls,

naphtelenes, phenanthrenes, and chrysenes as well as alkylated derivatives is similar to unburnt coals (Achten and Hofmann, 2009). The presence of certain alkylated naphthalenes in brown or sub-bituminous coals has been attributed to degradation of plant triterpenoids, which are common components of all lipid biomarker extracts found here (Chaffee and Fookes, 1988; Peters et al., 2005) although more generic sources of PAH are also ubiquitous. Studies of modern terrestrial soils show that soots, chars, and coals tend to have high aromaticity, as inferred here from both Rock-Eval pyrolysis and kerogen-bound aromatic parameters (Spiker et al., 1988). Sub-bituminous coals also show distinct odd-over-even predominance in C_{25}-C_{31} *n*-alkanes, such as we find here (thought they may preserve higher HI values; Romero-Sarmiento et al., 2011). Overall, these lines of evidence suggest weathering of soils and surficial coal beds may account for a major source of organic matter deposited locally at Site 913B (NMR spectroscopy or organic petrography would be required to confirm this finding; see Boucsein and Stein, 2009).

Organic-rich sediments with low hydrocarbon yields from solvent extraction is highly suggestive of type IV inert kerogen macerals, also known as inertinite. Inertinite is often connected with burn events and charcoal (Boucsein and Stein, 2009) or from intense diagenetic oxidation of kerogen following surface exposure. These events also typically enrich soils in condensed PAH due to rainout and selective degradation, with the result being termed pyrogenic organic matter, consistent with the hydrogen-lean composition of most of the bulk kerogen found here. Despite its commonly assumed inert and stable state, pyrogenic organic matter is not necessarily recalcitrant in surface

systems, being subject to degradation on the scale of thousands of years, similar to typical soil organic matter (Hilscher et al., 2009, Knicker, 2011). The extremely low HI values for Site 913B kerogens suggest that this oxic degradation was advanced. The rate of pyrogenic soil-derived organic matter oxidation appears to be related to high mean annual temperatures, rather than time spent in an oxic system (Knicker, 2011). The ultimate fate of kerogens can be altered by translocation of oxidized soil organic matter into colder, low oxygen marine sediments, which can significantly slow down degradation and help preserve soil organics in nearshore, thermally immature facies (Knicker, 2011; Sephton et al., 2015). In the warm high-latitude Eocene world, this translocation might sequester carbon from the exogenic pool that would otherwise fully return to atmospheric CO_2 on short time scales. Abundant evidence for geographically extensive warm polar regions with a strong hydrological cycle has been shown by swampy flora throughout the Arctic regions during the Eocene (Akhmetiev and Beniamovski, 2009; Eldrett et al., 2009; Greenwood et al., 2010). The hydrological and geographical characteristics of the Arctic may have provided an ideal place to form peat and coal sequences (i.e. Lavrushin and Alekseev, 2005; Akhmetiev and Beniamovski, 2009; Nelsen et al., 2016), then subsequently weather and transport them into marine sediments (as suggested by Boucsein and Stein, 2009). Diterpenoid and triterpenoid biomarkers such as retene and PO, as well as other terrestrial biomarkers are also frequently found in diverse arctic sediments and oils during the early Eocene (Schouten et al., 2007; Eiserbeck et al., 2012), suggesting that terrestrial organics are common components of high-latitude marine sedimentary organic matter (Boucsein and Stein 2000, 2009; Lavrushin and Alekseev,

2005; Stein et al., 2006). We show that the relative abundance of diterpenoid biomarkers at Site 913B is highest during the early Eocene and decreases markedly in younger sediments, a temporal trend continued in sediments less than 49 Ma (Inglis et al., 2020). After this point, distribution of higher plant lipids shifts dramatically, indicating either a change in depositional environment (i.e. increased distance from shore) or some long-term change in the hydrological cycle (i.e. precipitation and runoff) driven by a continually cooling climate. Thus, the warm and wet climate in the Arctic region during the early-middle Eocene may have been conducive to aiding a long-term drawdown of CO_2 through the enhanced erosion and burial of terrestrial organic matter, but with episodic net CO_2 release through extensive organic matter remineralization.

6. Future Work

Future compound specific carbon isotope stratigraphy may prove useful to deconvolute individual components of the carbon cycle (i.e. Pagani et al., 2006; Schouten et al., 2007; Pancost et al., 2013). We identified several plant derived biomarkers, including notably large abundances of retene and PO. As higher plant biomarkers, these compounds would have been produced in the ambient atmosphere of the early-middle Eocene Arctic. Thus, they may preserve a faithful signal of high latitude atmospheric carbon cycling dynamics. Furthermore, as they come from fundamentally different plant groups, we may learn about the effects of changing Arctic climates (temperature, hydrological cycles) on these different families (see Schouten et al., 2007).

The unusual samples with enriched TOCs and low HI are deserving of a more detailed analysis. A simple terrigenous source (oxidized soil material) is unlikely the only cause, rather these are likely due to high aromaticity from incorporated coal or inert oxidized kerogen (Spiker et al 1988; and see Boucsein and Stein, 2000). Organic maceral identification would help to quantify the differences and amounts of terrigenous organic matter, as well as more solidly identify *Azolla* episodes at high resolution for comparison to the biomarker record. Solid state NMR may prove useful for further structural characterization of the inert organic matter. Additional HyPy experiments, including work ups of low TOC samples, will be of great value to interpreting the overall contribution of polysaccharides and condensed PAH to organic matter. Further comparison between kerogen and bitumen bound sterane biomarker pools may allow the creation of a two-part mixing model comparing indigenous organic matter versus transported kerogen.

7. Conclusions

We examined sediments from the early-middle Eocene Norwegian-Greenland Sea (ODP Site 913B) to unravel organic source environments, organisms, and the interactions of local and global carbon cycles. We find that Site 913B organic matter appears to be derived primarily from a mix of oxidized soil materials and inert kerogen, overprinted on a typical baseline marine organic matter signal. Terrigenous constituents of sedimentary organic matter include diterpenoids (i.e. retene), triterpenoids (i.e. oleanane derivatives), diverse hopanoids, long chain n-alkanes, and at least a portion of the C_{29} steranes

(stigmastanes). Lipids from marine microorganisms encompass the C_{27} and C_{28} steranes, short chain n-alkanes and n-alkanoic acids, and dinosteranes. The proportions of gymnosperm to angiosperm plant input to organic matter lessens distinctively in younger sediments, suggesting a temporal variability perhaps linked to climatic change. Surprisingly, we find no direct evidence of a major Azolla biomass bloom input to Site 913B organic matter. Results from Rock-Eval pyrolysis and biomarker analyses suggest that δ^{13}Corg at Site 913B is not ideal for early-middle Eocene global carbon cycle correlations due to local remobilization of allochthonous organic matter. Due to a nearshore depositional environment, sedimentary organic matter carries a strong local signature that makes correlations to the global carbon cycle difficult. However, the $\delta^{13}C_{org}$ record does record variations reminiscent of cyclicity, potentially indicative of high-latitude orbital effects on hydrological cycles that influence organic carbon burial dynamics. The continuous deposition of terrigenous organic matter (inert kerogen and coal) over several million years at this high latitude site suggests that sequestration of terrestrial organic matter into the opening polar basins may have played a role in the drawdown of CO_2 following the EECO. During other intervals, the oxidation and remineralization of a large terrigenous organic matter pool may have been a net source of ^{13}C-depleted carbon dioxide and other volatile organics to the atmosphere and ocean.

Sample age (myr)	Depth (mbsf)	TOC (wt%)	N (wt%)	C/N	$\delta^{13}C$ (‰)	Carb%
48.29	685.34	1.5	0.09	16.3	-25.5	16.1
48.30	685.55	1.9	0.12	15.9	-26.6	16.7
48.31	685.76	2.8	0.17	16.8	-26.7	6.2
48.32	685.97	0.8	0.07	10.9	-25.7	
48.33	686.16	1.0	0.09	11.3	-25.2	14.2
48.34	686.35	0.5	0.05	10.3	-24.1	8.79
48.35	686.59	0.8	0.08	10.8	-25.3	13.2
48.36	686.76	1.0	0.09	11.3	-25.0	17.6
48.37	686.96	0.5			-24.7	17.7
48.38	687.14	0.9	0.08	11.1	-25.3	11.8
48.39	687.26	0.8	0.07	10.9	-25.2	8.9
48.40	687.46	0.4			-25.8	19.6
48.41	687.66	0.8	0.07	11.4	-25.1	15.3
48.42	687.84	0.6			-25.2	15.5
48.43	688.06	0.6	0.09	6.3	-24.5	
48.69	693.16	7.6	0.28	27.0	-26.4	18.9
48.70	693.38	0.6			-25.5	5.8
48.71	693.55	6.9	0.28	24.7	-26.8	19.0
48.72	693.76	1.1	0.08	14.1	-25.9	15.9
48.74	694.13	0.9	0.06	14.2	-26.4	14.4
48.75	694.33	3.6	0.18	19.8	-26.9	21.8
48.76	694.52	3.8	0.22	17.2	-27.4	22.3
48.77	694.74	0.8	0.05	16.0	-25.0	12.0
48.78	694.93	1.4	0.10	14.3	-26.9	17.3
48.79	695.13	0.5			-25.9	10.9
48.80	695.33	0.6			-27.5	28.0
49.20	703.45	1.1	0.08	14.3	-25.3	10.82
49.22	703.66	0.9	0.05	17.5	-25.3	13.0
49.23	703.86	1.1	0.07	15.1	-25.4	14.7
49.24	704.06	1.0	0.10	10.0	-25.2	11.78
49.27	704.36	0.9	0.06	14.3	-25.3	12.6
49.28	704.56	1.3	0.06	20.2	-26.2	13.6
49.29	704.76	0.7			-25.9	15.7
49.31	704.96	1.4	0.09	16.3	-25.5	17.4
49.32	705.16	1.3	0.08	16.2	-25.6	8.9
49.34	705.36	1.3	0.07	18.7	-26.0	
49.35	705.56	1.3	0.11	12.0	-25.4	13.81
49.37	705.82	1.1	0.07	15.7	-25.5	17.3
49.38	706.02	1.3	0.08	15.7	-25.4	13.8
49.40	706.22	1.1	0.07	15.4	-25.6	12.2
49.41	706.42	0.3	0.04	8.5	-24.8	13.0
49.42	706.62	0.4	0.04	10.0	-25.7	6.2
49.44	706.82	0.4			-25.4	20.3
49.45	707.02	0.7	0.07	10.2	-25.5	14.7
49.47	707.33	0.6	0.06	9.4	-25.7	23.2
49.49	707.53	0.6	0.06	9.8	-25.6	17.9
49.50	707.68	0.5	0.05	10.3	-25.4	12.1
49.52	707.93	0.2	0.02	9.0	-25.0	13.0
49.53	708.13	0.1	0.02	7.0	-24.4	8.8
49.54	708.33	0.2	0.02	8.0	-24.4	8.6
49.56	708.53	0.3	0.03	10.0	-25.8	7.7
49.57	708.73	0.2	0.03	7.0	-25.3	8.4

49.59	708.92	0.9	0.10	8.8	-25.4	11.78
49.60	709.09	1.1	0.09	12.4	-25.8	15.9
49.61	709.28	0.5	0.05	10.8	-25.1	11.7
49.63	709.48	0.2	0.02	9.5	-24.8	10.0
49.64	709.73	0.2	0.03	6.0	-24.4	7.5
49.65	709.89	0.2	0.02	9.5	-24.9	7.4
49.67	710.09	0.2	0.02	8.0	-24.7	11.8
49.84	712.47	0.9	0.07	13.2	-25.6	17.2
49.85	712.67	1.0	0.09	10.8	-25.4	14.0
49.86	712.84	0.9	0.10	8.9	-25.3	9.05
49.88	713.04	0.4	0.05	8.9	-25.1	13.8
49.89	713.27	1.1	0.10	10.7	-25.4	15.7
49.91	713.57	0.7			-26.7	16.8
49.93	713.77	0.8	0.08	10.8	-27.1	9.8
49.94	713.97	1.3	0.11	11.7	-26.6	12.9
49.96	714.17	0.5			-28.4	29.2
49.97	714.37	0.3	0.05	6.6	-25.8	27.0
49.98	714.57	0.3	0.05	5.8	-25.7	20.5
50.00	714.76	0.4			-25.7	13.3
50.01	714.97	0.9	0.09	10.1	-25.7	12.3
50.02	715.15	0.9	0.11	7.9	-25.7	14.44
50.04	715.36	0.8			-28.4	10.3
50.05	715.57	0.5			-26.2	13.5
50.07	715.76	1.0	0.09	10.8	-26.4	12.8
50.08	715.98	1.1	0.09	12.3	-26.8	11.4
50.09	716.15	0.5	0.06	8.9	-25.4	28.9
50.11	716.35	0.7	0.06	11.1	-27.6	16.2
50.12	716.53	0.5			-25.2	16.1
50.14	716.75	0.6	0.06	10.2	-25.9	12.3
50.15	716.93	0.5			-25.0	10.52
50.16	717.14	0.6	0.06	10.0	-25.3	13.0
50.18	717.34	0.8	0.07	11.3	-25.5	14.9
50.19	717.5	0.9	0.06	13.7	-26.3	
50.21	717.74	0.8	0.07	11.4	-25.8	15.2

Table 4.1: Bulk sediment geochemistry. Site 913B samples by age (Inglis et al., 2020) and depth. Including total organic carbon (wt% sediment), total nitrogen (wt% sediment), C/N ratio, $\delta^{13}C$ (‰), and carbonate contents (wt% sediment).

Sample age (myr)	Depth (mbsf)	P_{mc}	FA TAR	F/H	CPI	ACL	TAR	P_{aq}
48.29	685.34							
48.30	685.55	1.23	0.40	0.76	2.3	28.3	0.4	0.6
48.34	686.35							
48.39	687.26	0.54	2.03	1.06	4.8	27.9	1.9	0.5
48.69	693.16	0.85	0.95	0.79	2.5	28.3	1.8	0.5
48.70	693.38							
48.71	693.55	1.05	1.13	0.49	2.8	28.4	1.9	0.5
48.76	694.52							
48.77	694.74	1.10	0.20	7.63	2.2	27.3	0.9	0.7
49.20	703.45				2.6	28.5	2.9	0.4
49.22	703.66	0.60	0.85	1.93				
49.24	704.06	0.46	1.52	1.56	3.8	28.6	2.3	0.4
49.35	705.56	0.51	1.58	0.98	2.7	28.8	1.4	0.4
49.42	706.62							
49.50	707.68						0.5	
49.59	708.92							
49.63	709.48	2.02	0.08	5.22	1.7	25.8	0.6	1.0
49.64	709.73	2.65	0.06	14.52				
49.86	712.84	1.25	0.84	0.44	2.4	28.3	1.5	0.6
49.94	713.97	1.17	0.60	1.04	2.2	28.8	1.9	0.4
50.02	715.15	1.15	0.94	0.77	2.4	28.2	1.5	0.5
50.08	715.98	1.14	0.26	12.52	2.0	28.2	1.2	0.6
50.15	716.93	1.15	1.14	6.30	3.4	27.4	2.6	0.6

Table 4.2: Carboxylic acid and *n*-alkane data. P_{mc} = $(C_{20} + C_{22} + C_{24} + C_{26}) / (C_{28} + C_{30} + C_{32})$ FAMEs; FA TAR = $(C_{28} + C_{30} + C_{32})/ (C_{14} + C_{16} + C_{18})$ FAMEs; F/H = C_{16} saturated FAME/C_{32} ββ hopanoic acid; CPI = carbon preference index = $0.5 \times ((C_{25} + C_{27} + C_{29} + C_{31} / C_{26} + C_{28} + C_{30} + C_{32}) + (C_{27} + C_{29} + C_{31} + C_{33} / C_{26} + C_{28} + C_{30} + C_{32}))$ *n*-alkanes; ACL = average chain length = $(25 \times C_{25}) + (27 \times C_{27}) + (29 \times C_{29}) + (31 \times C_{31}) + (33 \times C_{33}) / \Sigma(C_{25\text{-}33)odd}$ *n*-alkanes; TAR = terrestrial to aquatic ratio = $C_{29} + C_{31} + C_{33} / C_{17} + C_{19} + C_{21}$ *n*-alkanes; $P_{aq} = C_{23} + C_{25} / C_{23} + C_{25} + C_{29} + C_{31}$ *n*-alkanes.

Sample age (myr)	Depth (mbsf)	Ts/Tm	C_{29} str ααα S/(S+R)	C_{31}H S/(S+R)	H/S	C_{27}%	C_{28}%	C_{29}%	C_{30}%	Gam.	HHI	4Me /Dino	R/PO
48.29	685.34	0.12	0.19	0.22	7.31	0.30	0.25	0.43	0.02	0.13	1.00	0.48	0.19
48.30	685.55	0.22	0.30	0.19	4.22	0.32	0.30	0.36	0.02	0.27	1.02	0.57	0.73
48.34	686.35	0.15	0.17	0.18	17.44	0.26	0.20	0.53	0.02	0.05	0.62	0.51	0.28
48.39	687.26	0.11	0.18	0.12	15.79	0.24	0.19	0.55	0.02	0.02	0.54	0.49	
48.69	693.16	0.18	0.17	0.18	2.87	0.29	0.30	0.39	0.02	0.28	0.63	0.59	8.73
48.70	693.38	0.15	0.14	0.22	5.18	0.28	0.29	0.40	0.03	0.17	0.70	0.50	4.77
48.71	693.55	0.14	0.12	0.13	3.47	0.30	0.29	0.38	0.02	0.24	0.34	0.64	0.18
48.76	694.52	0.22	0.16	0.25	2.58	0.31	0.32	0.34	0.02	0.13	1.00	0.79	0.05
48.77	694.74	0.21	0.28	0.14	3.39	0.26	0.31	0.41	0.02	0.26	0.85	0.41	0.28
49.20	703.45	0.17	0.05	0.09	5.73	0.20	0.22	0.57	0.01	0.07	0.37	0.57	52.02
49.24	704.06	0.16	0.11	0.13	9.39	0.20	0.22	0.56	0.02	0.04	0.78	0.59	21.15
49.35	705.56	0.17	0.10	0.12	6.95	0.19	0.22	0.58	0.01	0.05	0.71	0.54	15.79
49.42	706.62	0.20	0.16	0.26	5.90	0.21	0.26	0.49	0.03	0.11	1.21	0.41	3.58
49.50	707.68	0.20	0.12	0.21	5.63	0.29	0.25	0.44	0.02	0.12	0.74	0.62	4.66
49.59	708.92	0.16	0.08	0.18	6.04	0.26	0.24	0.48	0.02	0.09	0.47	0.80	3.55
49.63	709.48	0.35	0.44	0.37	1.39	0.31	0.34	0.33	0.02	0.52	3.48	0.29	1.00
49.64	709.73	0.19	0.19	0.19	5.31	0.23	0.27	0.48	0.02	0.21	1.30	0.58	
49.86	712.84	0.13	0.17	0.12	7.37	0.27	0.27	0.45	0.02	0.19	0.21	0.77	1.64
49.94	713.97	0.31	0.27	0.30	2.87	0.30	0.30	0.38	0.02	0.31	3.11	0.59	31.43
50.02	715.15	0.11	0.20	0.16	15.48	0.26	0.21	0.51	0.02	0.02	0.51	0.55	18.90
50.08	715.98	0.21	0.22	0.24	1.01	0.13	0.14	0.71	0.01	0.30	1.31	0.60	11.26
50.15	716.93	0.28	0.35	0.22	2.33	0.30	0.33	0.35	0.02	0.42	1.57	0.47	3.31

Table 4.3: Biomarker data. Ts/Tm = C_{27}H Ts/(Ts+Tm);); C_{29} str αααS/(S+R) = C_{29} sterane αααS/(S+R) ratio for thermal maturity; C_{31}H S/(S+R) = C_{31} αβ hopane S/(S+R) ratio for thermal maturity; H/S = C_{27}-C_{35} hopanes/C_{27}-C_{29} regular steranes; $C_{27\text{-}30}$% = % of individual $C_{27\text{-}30}$ steranes relative to all C_{27}-C_{30} regular steranes; Gam. = 10*(gammacerane/C_{30} αβ hopane); HHI = homohopane index (C_{35} homohopane/sum of C_{31}-C_{35} homohopanes); 4Me/Dinos = C_{30} 4-methylsteranes to dinosteranes; R/PO = ratio of diterpenoid retene vs a pentanoroleananonaene.

Sample age (myr)	Depth (mbsf)	HI	OI	Tmax
48.30	685.55	33	39	422
48.34	686.35	4	38	
48.39	687.26	11	35	
48.69	693.16	21	28	414
48.71	693.55	50	31	416
48.76	694.52	29	37	
49.20	703.45	36	47	
49.25	704.06	9	36	
49.35	705.56	6	39	
49.59	708.92	10	36	
49.64	709.73	65	165	426
49.86	712.84	28	20	
50.02	715.15	18	133	
50.08	715.98	50	55	425
50.15	716.93	17	31	

Table 4.4: Site 913B Rock-Eval pyrolysis and HAWK data. HI: hydrogen index; OI: oxygen index; Tmax.

References

Abbott, G. D., Bashir, F. Z., & Sugden, M. A. (2001). Kerogen-bound and free hopanoic acids in the messel oil shale kerogen. *Chirality*, *13*(8), 510–516.

Achten, C., & Hofmann, T. (2009). Native polycyclic aromatic hydrocarbons (PAH) in coals–a hardly recognized source of environmental contamination. *Science of the Total Environment*, *407*(8), 2461–2473.

Akhmetiev, M. A., & Beniamovski, V. N. (2009). Paleogene floral assemblages around epicontinental seas and straits in Northern Central Eurasia: Proxies for climatic and paleogeographic evolution. *Geologica Acta*, *7*(1), 297–309.

Andreasson, F. P., Schmitz, B., & Spiegler, D. (1996). Stable isotopic composition (δ 18 OCO 3 2-, δ 13 C) of early Eocene fish-apatite from Hole 913B: An indicator of the early Norwegian–Greenland Sea paleosalinity: in. *Proceedings of the Ocean Drilling Program, Scientific Results*, *151*, 583–591.

Banta, A. B., Wei, J. H., & Welander, P. V. (2015). A distinct pathway for tetrahymanol synthesis in bacteria. *Proceedings of the National Academy of Sciences*, *112*(44), 13478–13483.

Barke, J., van der Burgh, J., van Konijnenburg-van Cittert, J. H., Collinson, M. E., Pearce, M. A., Bujak, J., Heilmann-Clausen, C., Speelman, E. N., van Kempen, M. M., & Reichart, G.-J. (2012). Coeval Eocene blooms of the freshwater fern Azolla in and around Arctic and Nordic seas. *Palaeogeography, Palaeoclimatology, Palaeoecology*, *337*, 108–119.

Behrooz, L., Naafs, B. D. A., Dickson, A. J., Love, G. D., Batenburg, S. J., & Pancost, R. D. (2018). Astronomically driven variations in depositional environments in the South Atlantic during the Early Cretaceous. *Paleoceanography and Paleoclimatology*, *33*(8), 894–912.

Boucsein, B., & Stein, R. (2000). Particulate organic matter in surface sediments of the Laptev Sea (Arctic Ocean): Application of maceral analysis as organic-carbon-source indicator. *Marine Geology*, *162*(2–4), 573–586.

Boucsein, B., & Stein, R. (2009). Black shale formation in the late Paleocene/early Eocene Arctic Ocean and paleoenvironmental conditions: New results from a detailed organic petrological study. *Marine and Petroleum Geology*, *26*(3), 416–426.

Bray, E. E., & Evans, E. D. (1961). Distribution of n-paraffins as a clue to recognition of source beds. *Geochimica et Cosmochimica Acta*, *22*(1), 2–15.

Brinkhuis, H., Schouten, S., Collinson, M. E., Sluijs, A., Damsté, J. S. S., Dickens, G. R., Huber, M., Cronin, T. M., Onodera, J., & Takahashi, K. (2006). Episodic fresh surface waters in the Eocene Arctic Ocean. *Nature*, *441*(7093), 606–609.

Brocks, J. J., Jarrett, A. J., Sirantoine, E., Hallmann, C., Hoshino, Y., & Liyanage, T. (2017). The rise of algae in Cryogenian oceans and the emergence of animals. *Nature*, *548*(7669), 578–581.

Brouwer, P., Werf, A., Schluepmann, H., Reichart, G. J., & Nierop, K. G. J. (2016). Lipid yield and composition of Azolla filiculoides and the implications for biodiesel production. *BioEnergy Research*, *9*(1), 369–377.

Buchholz, B., Laczko, E., Pfennig, N., Rohmer, M., & Neunlist, S. (1993). Hopanoids of a recent sediment from Lake Constance as eutrophication markers. *FEMS Microbiology Ecology*, *11*(3–4), 217–223.

Budge, S. M. (1999). *Fatty acid biomarkers in a cold water marine environment* [PhD Thesis]. Memorial University of Newfoundland.

Cao, C., Love, G. D., Hays, L. E., Wang, W., Shen, S., & Summons, R. E. (2009). Biogeochemical evidence for euxinic oceans and ecological disturbance presaging the end-Permian mass extinction event. *Earth and Planetary Science Letters*, *281*(3), 188–201.

Carrie, J., Sanei, H., & Stern, G. (2012). Standardisation of Rock–Eval pyrolysis for the analysis of recent sediments and soils. *Organic Geochemistry*, *46*, 38–53.

Chaffee, A. L., & Fookes, C. J. (1988). Polycyclic aromatic hydrocarbons in Australian coals—III. Structural elucidation by proton nuclear magnetic resonance spectroscopy. *Organic Geochemistry*, *12*(3), 261–271.

Diefendorf, A. F., & Freimuth, E. J. (2017). Extracting the most from terrestrial plant-derived n-alkyl lipids and their carbon isotopes from the sedimentary record: A review. *Organic Geochemistry*, *103*, 1–21.

Eiserbeck, C., Nelson, R. K., Grice, K., Curiale, J., & Reddy, C. M. (2012). Comparison of GC–MS, GC–MRM-MS, and GC$\\times$ GC to characterise higher plant biomarkers in Tertiary oils and rock extracts. *Geochimica et Cosmochimica Acta*, *87*, 299–322.

Eldholm, O., & Thomas, E. (1993). Environmental impact of vocanic margin formation. *Earth and Planetary Science Letters*, *117*, 319–329.

Eldrett, J. S., Greenwood, D. R., Harding, I. C., & Huber, M. (2009). Increased seasonality through the Eocene to Oligocene transition in northern high latitudes. *Nature*, *459*(7249), 969–973.

Eldrett, J. S., Harding, I. C., Firth, J. V., & Roberts, A. P. (2004). Magnetostratigraphic calibration of Eocene–Oligocene dinoflagellate cyst biostratigraphy from the Norwegian–Greenland Sea. *Marine Geology*, *204*(1–2), 91–127.

Estes, R., & Hutchison, J. H. (1980). Eocene lower vertebrates from Ellesmere Island, Canadian arctic archipelago. *Palaeogeography, Palaeoclimatology, Palaeoecology*, *30*, 325–347.

Farquhar, G. D., Ehleringer, J. R., & Hubick, K. T. (1989). Carbon isotope discrimination and photosynthesis. *Annual Review of Plant Biology*, *40*(1), 503–537.

Farrimond, P., Griffiths, T., & Evdokiadis, E. (2002). Hopanoic acids in Mesozoic sedimentary rocks: Their origin and relationship with hopanes. *Organic Geochemistry*, *33*(8), 965–977.

France-Lanord, C., & Derry, L. A. (1997). Organic carbon burial forcing of the carbon cycle from Himalayan erosion. *Nature*, *390*(6655), 65–67.

Freeman, K. H., & Hayes, J. M. (1992). Fractionation of carbon isotopes by phytoplankton and estimates of ancient CO2 levels. *Global Biogeochemical Cycles*, *6*(2), 185–198.

Galeotti, S., Sprovieri, M., Rio, D., Moretti, M., Francescone, F., Sabatino, N., Fornaciari, E., Giusberti, L., & Lanci, L. (2019). Stratigraphy of early to middle Eocene hyperthermals from Possagno (Southern Alps, Italy) and comparison with global carbon isotope records. *Palaeogeography, Palaeoclimatology, Palaeoecology*, *527*, 39–52.

Godfrey, L. V., & Glass, J. B. (2011). The geochemical record of the ancient nitrogen cycle, nitrogen isotopes, and metal cofactors. In *Methods in enzymology* (Vol. 486, pp. 483–506). Elsevier.

Goodwin, N. S., Mann, A. L., & Patience, R. L. (1988). Structure and significance of C30 4-methyl steranes in lacustrine shales and oils. *Organic Geochemistry*, *12*(5), 495–506.

Greenwood, D. R., Basinger, J. F., & Smith, R. Y. (2010). How wet was the Arctic Eocene rain forest? Estimates of precipitation from Paleogene Arctic macrofloras. *Geology*, *38*(1), 15–18.

Hatcher, P. G., & Romankiw, L. A. (1985). Nuclear Magnetic Resonance Studies of Organic-Matter-Rich Sedimentary Rocks of Some Early Mesozoic Basins of the Eastern United States. *Proceedings of the Second US Geological Survey Workshop on the Early Mesozoic Basins of the Eastern United States*, *946*, 65.

Hayes, J. M., Strauss, H., & Kaufman, A. J. (1999). The abundance of 13C in marine organic matter and isotopic fractionation in the global biogeochemical cycle of carbon during the past 800 Ma. *Chemical Geology*, *161*(1–3), 103–125.

Hilscher, A., Heister, K., Siewert, C., & Knicker, H. (2009). Mineralisation and structural changes during the initial phase of microbial degradation of pyrogenic plant residues in soil. *Organic Geochemistry*, *40*(3), 332–342.

Huang, X., Xue, J., Wang, X., Meyers, P. A., Huang, J., & Xie, S. (2013). Paleoclimate influence on early diagenesis of plant triterpenes in the Dajiuhu peatland, central China. *Geochimica et Cosmochimica Acta*, *123*, 106–119.

Inglis, G. N., Carmichael, M. J., Farnsworth, A., Lunt, D. J., & Pancost, R. D. (2020). A long-term, high-latitude record of Eocene hydrological change in the Greenland region. *Palaeogeography, Palaeoclimatology, Palaeoecology*, *537*, 109378.

Inglis, G. N., Farnsworth, A., Lunt, D., Foster, G. L., Hollis, C. J., Pagani, M., Jardine, P. E., Pearson, P. N., Markwick, P., & Galsworthy, A. M. (2015). Descent toward the Icehouse: Eocene sea surface cooling inferred from GDGT distributions. *Paleoceanography*, *30*(7), 1000–1020.

Jacob, J., Disnar, J.-R., Boussafir, M., Albuquerque, A. L. S., Sifeddine, A., & Turcq, B. (2007). Contrasted distributions of triterpene derivatives in the sediments of Lake Caçó reflect paleoenvironmental changes during the last 20,000 yrs in NE Brazil. *Organic Geochemistry*, *38*(2), 180–197.

Kirtland Turner, S., Sexton, P. F., Charles, C. D., & Norris, R. D. (2014). Persistence of carbon release events through the peak of early Eocene global warmth. *Nature Geoscience*, *7*(10), 748–751.

Knicker, H. (2011). Pyrogenic organic matter in soil: Its origin and occurrence, its chemistry and survival in soil environments. *Quaternary International*, *243*(2), 251–263.

Knoll, A. H., Summons, R. E., Waldbauer, J. R., & Zumberge, J. E. (2007). The geological succession of primary producers in the oceans. In *Evolution of primary producers in the sea* (pp. 133–163). Elsevier.

Kodner, R. B., Pearson, A., Summons, R. E., & Knoll, A. H. (2008). Sterols in red and green algae: Quantification, phylogeny, and relevance for the interpretation of geologic steranes. *Geobiology*, *6*(4), 411–420.

Lavrushin, Y. A., & Alekseev, M. N. (2005). The arctic regions. *Geological Society of America Special Papers*, *382*, 13–29.

Lin, H.-C., & Chang, W.-L. (2000). Diterpenoids from Salvia miltiorrhiza. *Phytochemistry*, *53*(8), 951–953.

Love, G. D., Bowden, S. A., Jahnke, L. L., Snape, C. E., Campbell, C. N., Day, J. G., & Summons, R. E. (2005). A catalytic hydropyrolysis method for the rapid screening of microbial cultures for lipid biomarkers. *Organic Geochemistry*, *36*(1), 63–82.

Love, G. D., Snape, C. E., Carr, A. D., & Houghton, R. C. (1995). Release of covalently-bound alkane biomarkers in high yields from kerogen via catalytic hydropyrolysis. *Organic Geochemistry*, *23*(10), 981–986.

Lunt, D. J., Farnsworth, A., Loptson, C., L Foster, G., Markwick, P., O'Brien, C. L., Pancost, R. D., Robinson, S. A., & Wrobel, N. (2016). Palaeogeographic controls on climate and proxy interpretation. *Climate of the Past*, *12*(5).

Lunt, D. J., Ridgwell, A., Sluijs, A., Zachos, J., Hunter, S., & Haywood, A. (2011). A model for orbital pacing of methane hydrate destabilization during the Palaeogene. *Nature Geoscience*, *4*(11), 775–778.

McGroddy, M. E., Daufresne, T., & Hedin, L. O. (2004). Scaling of C: N: P stoichiometry in forests worldwide: Implications of terrestrial redfield-type ratios. *Ecology*, *85*(9), 2390–2401.

Meredith, W., Kelland, S.-J., & Jones, D. M. (2000). Influence of biodegradation on crude oil acidity and carboxylic acid composition. *Organic Geochemistry*, *31*(11), 1059–1073.

Moran, K., Backman, J., Brinkhuis, H., Clemens, S. C., Cronin, T., Dickens, G. R., Eynaud, F., Gattacceca, J., Jakobsson, M., & Jordan, R. W. (2006). The Cenozoic Palaeoenvironment of the Arctic Ocean. *Nature*, *441*(7093), 601–605.

Myhre, A.M., Thiede, J., Firth, J.V., Party, S.S., (1995). Initial reports: sites 907–913, North Atlantic–Arctic gateways I. In: Proceedings, Initial Reports, Ocean Drilling Program, ODP. Vol. 151. Ocean Drilling Program, College Station, TX, pp. 926.

Nierop, K. G., Brouwer, P., Dekker, R., Schluepmann, H., & Reichart, G.-J. (2018). ω20-Hydroxy and ω9, ω10-dihydroxy biomarker lipids in ferns from the Salviniaceae family. *Organic Geochemistry*, *125*, 229–242.

Nilsen, T. H. (1983). Influence of the Greenland-Scotland Ridge on the geological history of the North Atlantic and Norwegian-Greenland Sea areas. In *Structure and development of the Greenland-Scotland Ridge* (pp. 457–478). Springer.

Otto, A., Simoneit, B. R., & Rember, W. C. (2005). Conifer and angiosperm biomarkers in clay sediments and fossil plants from the Miocene Clarkia Formation, Idaho, USA. *Organic Geochemistry*, *36*(6), 907–922.

Pagani, M., Pedentchouk, N., Huber, M., Sluijs, A., Schouten, S., Brinkhuis, H., Damsté, J. S. S., Dickens, G. R., Backman, J., & Clemens, S. (2006). Arctic hydrology during global warming at the Palaeocene/Eocene thermal maximum. *Nature*, *442*(7103), 671.

Pancost, R. D., & Boot, C. S. (2004). The palaeoclimatic utility of terrestrial biomarkers in marine sediments. *Marine Chemistry*, *92*(1–4), 239–261.

Pancost, R. D., Freeman, K. H., Herrmann, A. D., Patzkowsky, M. E., Ainsaar, L., & Martma, T. (2013). Reconstructing Late Ordovician carbon cycle variations. *Geochimica et Cosmochimica Acta*, *105*, 433–454.

Pearson, P. N., van Dongen, B. E., Nicholas, C. J., Pancost, R. D., Schouten, S., Singano, J. M., & Wade, B. S. (2007). Stable warm tropical climate through the Eocene Epoch. *Geology*, *35*(3), 211–214.

Peters, K. E., Walters, C. C., & Moldowan, J. M. (2005). *The biomarker guide* (Vol. 1). Cambridge University Press.

Radionova, E. P., & Khokhlova, I. E. (2000). Was the North Atlantic connected with the Tethys via the Arctic in the early Eocene? Evidence from siliceous plankton. *GFF*, *122*(1), 133–134.

Roberts, C. D., LeGrande, A. N., & Tripati, A. K. (2009). Climate sensitivity to Arctic seaway restriction during the early Paleogene. *Earth and Planetary Science Letters*, *286*(3–4), 576–585.

Romero-Sarmiento, M.-F., Riboulleau, A., Vecoli, M., Laggoun-Défarge, F., & Versteegh, G. J. (2011). Aliphatic and aromatic biomarkers from Carboniferous coal deposits at Dunbar (East Lothian, Scotland): Palaeobotanical and palaeoenvironmental significance. *Palaeogeography, Palaeoclimatology, Palaeoecology*, *309*(3–4), 309–326.

Saito, H., & Suzuki, N. (2007). Distributions and sources of hopanes, hopanoic acids and hopanols in Miocene to recent sediments from ODP Leg 190, Nankai Trough. *Organic Geochemistry*, *38*(10), 1715–1728.

Schaeffer, P., Adam, P., Trendel, J.-M., Albrecht, P., & Connan, J. (1995). A novel series of benzohopanes widespread in sediments. *Organic Geochemistry*, *23*(1), 87–89.

Schouten, S., Woltering, M., Rijpstra, W. I. C., Sluijs, A., Brinkhuis, H., & Damsté, J. S. S. (2007). The Paleocene–Eocene carbon isotope excursion in higher plant organic matter: Differential fractionation of angiosperms and conifers in the Arctic. *Earth and Planetary Science Letters*, *258*(3–4), 581–592.

Sephton, M. A., Jiao, D., Engel, M. H., Looy, C. V., & Visscher, H. (2015). Terrestrial acidification during the end-Permian biosphere crisis? *Geology*, *43*(2), 159–162.

Sephton, M. A., Looy, C. V., Brinkhuis, H., Wignall, P. B., De Leeuw, J. W., & Visscher, H. (2005). Catastrophic soil erosion during the end-Permian biotic crisis. *Geology*, *33*(12), 941–944.

Sexton, P. F., Norris, R. D., Wilson, P. A., Pälike, H., Westerhold, T., Röhl, U., Bolton, C. T., & Gibbs, S. (2011). Eocene global warming events driven by ventilation of oceanic dissolved organic carbon. *Nature*, *471*(7338), 349–352.

Simoneit, B. R., Grimalt, J. O., Wang, T. G., Cox, R. E., Hatcher, P. G., & Nissenbaum, A. (1986). Cyclic terpenoids of contemporary resinous plant detritus and of fossil woods, ambers and coals. *Organic Geochemistry*, *10*(4–6), 877–889.

Sinninghe Damsté, J. S., Kenig, F., Koopmans, M. P., Koster, J., Schouten, S., Hayes, J. M., & de Leeuw, J. W. (1995). Evidence for gammacerane as an indicator of water column stratification. *Geochimica et Cosmochimica Acta*, *59*(9), 1895–1900.

Speelman, Eveline N., Reichart, G.-J., de Leeuw, J. W., Rijpstra, W. I. C., & Damsté, J. S. S. (2009a). Biomarker lipids of the freshwater fern Azolla and its fossil counterpart from the Eocene Arctic Ocean. *Organic Geochemistry*, *40*(5), 628–637.

Speelman, Eveline N., Sewall, J. O., Noone, D., Huber, M., von der Heydt, A., Damsté, J. S., & Reichart, G.-J. (2010). Modeling the influence of a reduced equator-to-pole sea surface temperature gradient on the distribution of water isotopes in the Early/Middle Eocene. *Earth and Planetary Science Letters*, *298*(1–2), 57–65.

Speelman, Eveline N., van Kempen, M. M., Barke, J., Brinkhuis, H., Reichart, G.-J., Smolders, A. J., Roelofs, J. G., Sangiorgi, F., de Leeuw, J. W., & Lotter, A. F. (2009b). The Eocene Arctic Azolla bloom: Environmental conditions, productivity and carbon drawdown. *Geobiology*, *7*(2), 155–170.

Speelman, Eveline Neletta. (2010). *Reconstruction of the Arctic Ocean environment during the Eocene Azolla interval using geochemical proxies and climate modeling. Geologica Ultraiectina (331)*. Departement Aardwetenschappen.

Spiker, E. C., Kotra, R. K., Hatcher, P. G., Gottfried, R. M., Horan, M. F., & Olsen, P. E. (1988). Source of kerogen in black shales from the Hartford and Newark basins, eastern United States. In *Studies of the Early Mesozoic Basins of the Eastern United States* (Vol. 1776, pp. 63–68). US Geol. Surv. Bull. 1776.

Stein, R., Boucsein, B., & Meyer, H. (2006). Anoxia and high primary production in the Paleogene central Arctic Ocean: First detailed records from Lomonosov Ridge. *Geophysical Research Letters*, *33*(18).

Stein, R., Weller, P., Backman, J., Brinkhuis, H., Moran, K., & Pälike, H. (2014). Cenozoic Arctic ocean climate history: Some highlights from the integrated ocean drilling program Arctic coring expedition. In *Developments in Marine Geology* (Vol. 7, pp. 259–293). Elsevier.

Summons, R. E., Volkman, J. K., & Boreham, C. J. (1987). Dinosterane and other steroidal hydrocarbons of dinoflagellate origin in sediments and petroleum. *Geochimica et Cosmochimica Acta*, *51*(11), 3075–3082.

Ten Haven, H. L., & Rullkötter, J. (1989). Oleanene, ursene and other terrigenous triterpenoid biological marker hydrocarbons in Baffin Bay sediments. *Proceedings of the Ocean Drilling Program, Scientific Results*, *105*, 233–242.

Thiede, J., Myhre, A. M., & Firth, J. V. (1995). Cenozoic Northern Hemisphere polar and subpolar ocean paleoenvironments (summary of ODP Leg 151 drilling results). *Proceedings of the Ocean Drilling Program. Initial Reports*, *151*, 397–420.

van Kempen, M. M., Smolders, A. J., Bögemann, G. M., Lamers, L. L., Visser, E. J., & Roelofs, J. G. (2013). Responses of the Azolla filiculoides Stras.–Anabaena azollae Lam. association to elevated sodium chloride concentrations: Amino acids as indicators for salt stress and tipping point. *Aquatic Botany*, *106*, 20–28.

van Kempen, M. M., Smolders, A. J., Bögemann, G. M., Lamers, L. P., & Roelofs, J. G. (2016). Interacting effects of atmospheric CO 2 enrichment and solar radiation on growth of the aquatic fern Azolla filiculoides. *Freshwater Biology*, *61*(5), 596–606.

van Kempen, M. M., Smolders, A. J., Lamers, L. P., & Roelofs, J. G. (2012). Micro-halocline enabled nutrient recycling may explain extreme Azolla event in the Eocene Arctic Ocean. *PloS One*, *7*(11).

Volkman, J. (2003). Sterols in microorganisms. *Applied Microbiology and Biotechnology*, *60*(5), 495–506.

Waddell, L. M., & Moore, T. C. (2008a). Salinity of the Eocene Arctic Ocean from oxygen isotope analysis of fish bone carbonate. *Paleoceanography*, *23*(1).

Waddell, L. M., & Moore, T. C. (2008b). Salinity of the Eocene Arctic Ocean from oxygen isotope analysis of fish bone carbonate. *Paleoceanography*, *23*(1).

Wei, H., & Songnian, L. (1990). A new maturity parameter based on monoaromatic hopanoids. *Organic Geochemistry*, *16*(4–6), 1007–1013.

Weller, P., & Stein, R. (2008). Paleogene biomarker records from the central Arctic Ocean (Integrated Ocean Drilling Program Expedition 302): Organic carbon sources, anoxia, and sea surface temperature. *Paleoceanography*, *23*(1).

Westerhold, T., & Röhl, U. (2009). High resolution cyclostratigraphy of the early Eocene-new insights into the origin of the Cenozoic cooling trend. *Climate of the Past*, *5*(3).

Zachos, J. C., Dickens, G. R., & Zeebe, R. E. (2008). An early Cenozoic perspective on greenhouse warming and carbon-cycle dynamics. *Nature*, *451*(7176), 279–283.

Zachos, J. C., McCarren, H., Murphy, B., Röhl, U., & Westerhold, T. (2010). Tempo and scale of late Paleocene and early Eocene carbon isotope cycles: Implications for the origin of hyperthermals. *Earth and Planetary Science Letters*, *299*(1–2), 242–249.

Zachos, J., Pagani, M., Sloan, L., Thomas, E., & Billups, K. (2001). Trends, rhythms, and aberrations in global climate 65 Ma to present. *Science*, *292*(5517), 686–693.

Zumberge, J. E. (1987). Terpenoid biomarker distributions in low maturity crude oils. *Organic Geochemistry*, *11*(6), 479–496.

CHAPTER FIVE

Summary of the Dissertation

1. Summary

This dissertation presents organic geochemical data spanning Phanerozoic environmental transitions to understand the effects of paleoenvironmental change on past microbes, and vice versa. First, we explored one of the major mass extinction events in Earth's history, the end-Devonian Hangenberg Crisis. Using a combination of stable organic isotopes and trace metal geochemistry we identified the onset of this extinction event for the first time in the Cleveland Shale Member of the Ohio Shale in the Appalachian Basin. Lipid biomarker analysis and constraints from bioturbation indicate that while the Cleveland Shale depositional environment was predominantly euxinic (extending into the photic zone as shown through the ubiquitous presence of green sulfur bacteria), there were frequent periods of oxygenation down to the seafloor. Throughout the black shale succession in the upper Cleveland Shale, there was apparently no major shift in the microbial community structure as inferred from the major characteristics of the lipid biomarker assemblages. Our evidence confirms that microbial communities survive, even thrive in some shelf settings, and sustain primary productivity during extinction events. Indeed, locally redox-stratified marine conditions with anoxic/euxinic zones extending into the lower photic zone could not be sustained without this microbial biomass. Further, our data show that the Paleozoic transition to C_{28} sterane producing algae, previously purported to be due to the Hangenberg crisis, is delayed in tropical

paleolatitudes until after the Hangenberg Crisis. Shallow burrows found throughout the Cleveland Shale highlight the limitations of some geochemical redox approaches for recognizing short-lived and sporadic redox changes that deviate from anoxic/euxinic baseline conditions. Brief oxygenation pulses support short lived bioturbation events occurring even within a strongly and predominantly redox-stratified euxinic basin and underscore the necessity of integrating multiple independent redox proxies for a more complete paleoenvironmental reconstruction.

The second part of this dissertation explores how changing microbial communities, shown by successions of characteristic lipid biomarkers, reflect first order changes in paleoenvironmental conditions. Based off a well-studied stratigraphic framework with distinctive cyclicity, we analyzed samples from the Towako Formation of the Newark rift basin. We find that previous sedimentological interpretations of the lake's deepening, highstand, and evaporitic phases match extremely well to variations in a suite of biomarkers including gammacerane, carotenoids, tricyclic terpanes, and methylhopanes. The addition of biomarker parameters, especially in combination with stable isotopic measurements of sedimentary organic matter, particularly $\delta^{15}N_{total}$, represents a powerful way to recognize pH of ancient extreme systems. Within this context, diverse proxies, alone and in combination, may help us delineate and characterize ancient alkaline systems. Further, due to its geochemical recognition as an alkaline lacustrine environment, the Towako Formation can better serve as an ancient natural laboratory for assessing the effects of high pH on paleoenvironmental proxies

used routinely by geochemists to track the redox evolution of Earth's surface environments across geologic time.

Lastly, we travelled to the early-middle Eocene Norwegian-Greenland Sea (ODP Site 913B) in order to the explore the history of global climactic variability occurring during the early Cenozoic. We characterized organic source environments, organismal input to organic matter, and the interactions of local and global carbon cycles. We find that Site 913B organic matter appears to be derived from a mix of oxidized soil materials and inert kerogen, overprinted on a background marine signal. While a strong terrestrial source appears continuously throughout the section, we find evidence of changing source organisms. The proportion of gymnosperm to angiosperm input to organic matter lessens distinctively in younger sediments, but surprisingly, we find no direct evidence of blooms from the freshwater fern *Azolla* as an important source of Site 913B organic matter. Results from organic geochemical analyses suggest that $\delta^{13}C_{org}$ at Site 913B is not ideal for early-middle Eocene global carbon cycle correlations, however, the site does record variations reminiscent of cyclicity, potentially indicative of high-latitude orbital effects on hydrological cycles. The continuous deposition of terrigenous organic matter (inert kerogen and coal) over several million years at this high latitude site suggests that sequestration of terrestrial organic matter into the opening polar basins may have played a role in the drawdown of CO_2 leading into the modern Cenozoic icehouse.

2. Future work

Studies are ongoing in the Devonian Appalachian Basin. It remains to be discovered if the other biotic crises hosted in Devonian black shales record the same biogeochemical trends as the Hangenberg Crisis and the Upper Kellwasser Event. Current work is focusing on adding the Lower Kellwasser Event and potentially the Dasberg event to the compendium of Late Devonian biomarker analyses in the Appalachian Basin. In concert with trace metal, bioturbation, and palynological analyses this will allow us to constrain extinction magnitude versus redox sensitivity in the Appalachian Basin. We aim to discover if the Appalachian Basin truly represents the greater world, or if it rather represents a large, insulated paleoenvironment. This in turn has implications for the global extent and diversification of planktonic communities throughout the Paleozoic. These sites in the Appalachian Basin also provide an excellent laboratory to test some of the recent ideas regarding trigger mechanisms for the Hangenberg Crisis – in particular, mass terrestrial forest die offs and increased continental runoff leading to enhanced productivity worldwide. Since the Cleveland-Bedford contact is gradational and the Hangenberg Crisis is now defined, we can look in detail at preserved kerogen to see if there is any shift in the bound organic matter pool (changes in the distributions of condensed PAH) that is linked to lithology or climatological change.

The most interesting biomarker results from the Newark Basin are found in the low total organic carbon evaporitic shales and siltstones. These rocks preserve a few strange signals including sky-high 2-methylhopane indices and mysteriously low values

of the C_{26} tricyclic terpanes. Given that these parameters are heavily used to define a wide range of environments and ecologies (see: hypersaline/alkaline lakes and the prevalence of cyanobacteria) this provides a new direction for research. Comparison of these evaporitic silts to modern analogues, like the evaporitic crusts or sabkha of the Salton Sea, California, may provide new insights into better interpreting these signals in the ancient rock record.

There is a significant amount of work still to be done at Site 913B in the Norwegian-Greenland Sea. Further analyses of kerogen-bound biomarkers are needed to confirm the hypothesis that the bulk of the organic matter appears to be terrestrial in origin, hosting a wide variety of phenolic compounds and condensed PAH. Structural characterization of the organic matter via NMR – especially the high organic, low hydrocarbon samples – will help decipher the aromaticity and apparent inertness of the Site 913B organic matter. Compound specific isotope analyses will allow a more detailed exploration of organic matter sources. By analyzing terrestrial plant biomarker isotopes, we could also get an idea about variations in ambient atmospheric CO_2 during the early-middle Eocene. Together, these analyses can confirm the continuous input of soil and fire derived organic matter into the Eocene polar basins, and, with comparison to in-depth paleogeographic and literature review may inform the sequestration of CO_2 during the early-middle Eocene.